Title

Label-Free Optical Mapping for Large-Area Biomechanical Dynamics of Multicellular Systems

Author

Lin, Yen-Ju

Publication Date

2023

Peer reviewed|Thesis/dissertation

UNIVERSITY OF CALIFORNIA

Los Angeles

Label-Free Optical Mapping for Large-Area Biomechanical Dynamics of Multicellular Systems

A dissertation submitted in partial satisfaction of the

requirements for the degree Doctor of Philosophy

in Electrical and Computer Engineering

by

Yen-Ju Lin

2023

ABSTRACT OF THE DISSERTATION

Label-Free Optical Mapping for Large-Area Biomechanical Dynamics of Multicellular Systems

by

Yen-Ju Lin

Doctor of Philosophy in Electrical and Computer Engineering

University of California, Los Angeles, 2023

Professor Rob Candler, Co-Chair

Professor Pei-Yu Chiou, Co-Chair

Biomechanical properties, such as cellular stiffness and cell-generating force, play pivotal roles in mechanotransduction, the process cells sense, adapt and respond to external stimuli in their surrounding microenvironments. They are critical biomarkers that can indicate the physiological states and molecular configurations of cells. Despite its promising scope, existing technologies for mapping large-area biomechanical properties are still limited, mostly restricted by the small field of view and scanning nature of traditional traction force microscopy (TFM). On the other hand, for a multicellular system to function properly, dynamic equilibrium and coordinated interplays

between biomechanical, biochemical, and bioelectrical properties are crucial. Chaotic activities of either of these properties can break the equilibrium, subsequently interrupting the associated downstream events, and can even lead to fatal failure of the whole system. Therefore, the capability to perform real-time monitoring of dynamic changes can provide groundbreaking insights into the bidirectional interactions in biological systems.

In this dissertation, a novel platform for mapping large-area biomechanical dynamics is proposed, designed, and established. The platform utilizes a massive number of optical diffractive elements embedded periodically in an elastic membrane to track the traction force generated by the cells seeded on top. Observation field of view up to 10.6 mm by 10.6 mm is achieved, which is 3 orders of magnitude improvement compared to traditional TFM. Meanwhile, high spatiotemporal resolution is maintained, allowing us to measure transient activities at cellular level.

To demonstrate the capabilities of our platform for visualizing the large-area biomechanical dynamics in real-time, monolayer tissue composed of millions of neonatal rat ventricular myocytes (NRVMs) are seeded on our devices. For the first time, global trend and local heterogeneities of mechanical waves created by cardiac beatings of NRVMs are recorded concurrently with unprecedented details. Conduction patterns, activation time, activation durations, conduction velocities and dominant frequencies are analyzed temporally and spatially. In addition, several conditions, including spontaneous beating, electrical stimulation, and chemical stimulation are conducted. The results further highlight our platform's potential for biological applications such as drug screening and pathological studies. Moreover, the label-free feature of our platform introduces minimized interruption to the physiological activities of cells, thereby extending the observation time of experiments. Recordings of biomechanical dynamics from the same NRVM

cultures up to 7 days are reported. This is a dramatic enhancement compared to conventional optical mapping using fluorescent dyes, which often has hours-long observation window.

Lastly, we integrated the platform with a fluorescent imaging system to conduct simultaneous mappings of the calcium ion concentration and biomechanical dynamics resulting from the cardiac beating of NRVMs. It is the first demonstration of detailed mechanical wave propagation and the corresponding calcium ion transient. Our innovative approach holds promise for studying the complex interplay between biomechanical, biochemical, and bioelectrical properties in biological systems.

The dissertation of Yen-Ju Lin is approved.

Arjun Deb

Wentai Liu

Rob Candler, Committee Co-Chair

Pei-Yu Chiou, Committee Co-Chair

University of California, Los Angeles

2023

TABLE OF CONTENTS

LIST OF FIGURES

LIST OF TABLES

ACKNOWLEDGEMENTS

It has been an extremely challenging yet fruitful experience in the past few years while working toward my Ph.D. degree. Sincerely, I want to express my gratitude to all who help me throughout this journey.

First of all, I want to give my deepest appreciation to my advisor, Professor Eric Pei-Yu Chiou for his guidance and support. Especially during the time when I was at the most difficult time, his trust and passion for research inspired me to persist and re-ignite my motivations. Without his assistance, I wouldn't be able to complete this degree. I also would like to thank my co-advisor, Professor Rob Candler, and my committee members, Professor Arjun Deb and Professor Wentai Liu, for their professional suggestions and precious time on my work.

The experiments cannot be completed without the tremendous assistance from our collaborators: Dr. Tung-Yu Wu, Dr. Yijie Wang, Linlin Zhang, Dr. Arash Pezhouman and Dr. Reza Ardehali. I would like to thank them for their invaluable input and help on optical setup and cell experiments.

I also would like to thank all my colleagues from the Optofluidics Systems Lab for their tremendous help. Specifically, I would like to thank Dr. Xing Haw Marvin Tan, for his guidance in this field and the time and effort for training and transferring many hands-on skills and techniques. I am also grateful to Dr. Kylie Pei-Shan Chung for her countless help in many aspects. I also want to thank Dr. Ting-Hsiang Wu for a lot of invaluable suggestions, especially for the cell experiments. And I want to show appreciation to Dr. Tianxing Man, Xiang Zhang, Jake Smith, Rosa Son, Alexi Gill, Jacqueline Duong, Hsin Lan, and Amanda Zhou for their time and assistance in the lab.

I wish to thank the UCLA Nanolab and all staff members for the guidance in cleanroom facilities: Dr. You-Sheng (Wilson) Lin, Lorna Tokunaga, Krissy Do, Joe Zendejas, Hoc Ngo, Brian Matthews, Yuwei Fan, Angelica Saenz-Trevizo. I also want to thank Deeona Columbia and all UCLA ECE and MAE department staffs for their assistance in administration process and paperwork.

I would like to thank all the people who provide different aspects of suggestions and technical discussion and help throughout my Ph.D. experience: Dr. Yu-Tao Yang, Hao-Yu Chien, Dr. Huei-Bin Wang, Yi-Chun Hung, Shlin Chen, Joseph Tsai, Dr. Hung-Yu Yang, Dr. Mona Jarrahi, Dr Shang-Hua Yang, Dr. Nezih Tolga Yardimci, Dr. Semih Cakmakyapan, Dr. Deniz Turan, Dr. Ping-Keng Lu, Dr. Leihao Wei, Dr. Yen-Wen Tseng, Dr. Maggie Xiao, Dr. Yu-Ching Hsiao. I learned and gained a lot from them.

Finally, I would like to thank my families and friends for their love and support throughout the years.

VITA

Education

2014 – 2016 M.S., Communication Engineering

National Taiwan University, Taipei, Taiwan

2010 – 2014 B.S., Electrical Engineering

National Taiwan University, Taipei, Taiwan

Master's Thesis

Y.-J. Lin, "Resonator-Based Noise Suppressors with Detachable Capability for the Mitigation of Electromagnetic Interference," M.S. thesis, Dept. Elect. Eng., National Taiwan Univ., Taipei, Taiwan, 2016.

Selected Publications and Presentations

[1] X. Zhang, R. Son, **Y.-J. Lin**, A. Gill, S. Chen, T. Qi, D. Choi, J. Wen, Y. Lu, N. Y. C. Lin, and P.-Y. Chiou, "Rapid prototyping of functional acoustic devices using laser manufacturing, " Lab Chip, vol. 13, Oct. 2022, doi: 10.1039/d2lc00725h.

[2] S. Li, T. Yokota, P. Wang, J. T. Hoeve, F. Ma, T. M. Le, E. R. Abt, Y. Zhou, R. Wu, M. Nathavongdouangsy, A. Rodriguez, Y. Wang, **Y.-J. Lin**, H. Muranaka, M. Sharpley, D. T.

Braddock , V. E. MacRae, U. Banerjee, P.-Y. Chiou, M. Seldin, D. Huang, M. Teitell, I. Gertsman, M. Jung, S. J Bensinger, R. Damoiseaux, K. Faull, M. Pellegrini, A. J Lusis, T. Graeber , C. G Radu and A. Deb, "Cardiomyocytes disrupt pyrimidine biosynthesis in nonmyocytes to regulate heart repair, " Journal of Clinical Investigation, vol. 132, no. 2, Jan. 2022, doi: 10.1172/JCI149711.

[3] **Y.-J. Lin**, M. Jarrahi, "Heterodyne Terahertz Detection through Electronic and Optoelectronic Mixers", Reports on Progress in Physics, 83, 2020

[4] **Y.-J. Lin**, S. Cakmakyapan, N. Wang, D. Lee, M. Spearrin, and M. Jarrahi, "Plasmonic heterodyne spectrometry for resolving the spectral signatures of ammonia over a 1-4.5 THz frequency range," Optics. Express 27, 36838-36845, 2019.

[5] N. Wang, S. Cakmakyapan, **Y.-J. Lin**, H. Javadi and M. Jarrahi, "Room-temperature heterodyne terahertz detection with quantum-level sensitivity", Nature Astronomy, DOI: 10.1038/s41550-019-0828-6, 2019.

[6] N. Wang, S. Cakmakyapan, **Y.-J. Lin**, M. Jarrahi, "Near-Quantum-Limited Double-Sideband Noise Temperature Through Room-Temperature Plasmonic Heterodyne Terahertz Spectrometers," Proc. International Conference on Infrared, Millimeter, and Terahertz Waves, Nagoya, Japan, Sep. 9-14, 2018.

[7] **Y.-J. Lin**, Y. C. Tseng, T. L. Wu, "A Resonator-Based Suppressor for Mitigating the Noise Transfer on Metal Plates for Control of Electromagnetic Interference," in IEEE Microwave and Wireless Components Letters, vol. 26, no. 11, pp. 906-908, Nov. 2016.

[8] **Y.-J. Lin**, Y. C. Tseng, C.Y. Hsiao and T. L. Wu, "A SMD-Type Filter Solution for EMI/RFI Mitigation on High-Speed Digital Interfaces and Its Application," 2015 Asia-Pacific Symposium on Electromagnetic Compatibility, Taipei, 2015, pp. 696-699

Chapter 1 Introduction

1.1 Biomechanical Properties of Cells

Biomechanical properties of cells, such as cellular stiffness and cell-generated force, are direct indications of their physiological states and molecular configurations [1] . For example, the stiffness of infected human red blood cells can increase up to 10-fold compared to their healthy counterparts [2]. In addition, cell-generated forces play essential roles in mechanotransduction, the process that cells sense, adapt and respond to external stimuli in their surrounding microenvironments [3], [4]. Abnormal traction forces in cells are often related to disease states or cellular dysfunctions [5]. For instance, insufficient contractility in cardiac muscle cells (cardiomyocytes) can lead to serious heart diseases [6]. Furthermore, the effectiveness and possible side effects of a drug can be evaluated by observing the induced changes of these biomechanical properties in cell clusters such as abnormal contraction and arrhythmic pattern. Therefore, profiling the biomechanical properties of cell clusters in a biological system can provide valuable information in cell evolution, disease detection, and therapeutic targets.

Moreover, biomechanical properties play crucial roles on the collective behaviors in multicellular structures. In a typical multicellular structure, millions of cells need to behave coordinately and coherently to ensure proper biological functions such as migration [7] , proliferation [8] and differentiation [9]. Chaotic mechanical activities in certain cell clusters can lead to fatal failure of the whole multicellular structures. For example, ventricular fibrillation or atrial fibrillation, caused by the uncoordinated rhythms of lower and upper heart chambers, can lead to deadly cardiac failure [10], [11]. Specifically, cell-generated forces are critical messenger

for cells to probe their surrounding microenvironments, communicate in between cells, and respond to external stimuli accordingly (**Figure 1.1**) [12]. Hence, studies of cell-generated forces and their roles on various cellular functions can provide informative understanding of diverse physiological events and the keys for multicellular structures to behave in an orchestrated manner. There are different existing techniques to measure and quantify cell-generated forces, spanning from different time and length scales and under different scenarios. These techniques will be discussed in detail in **Section 1.3**.

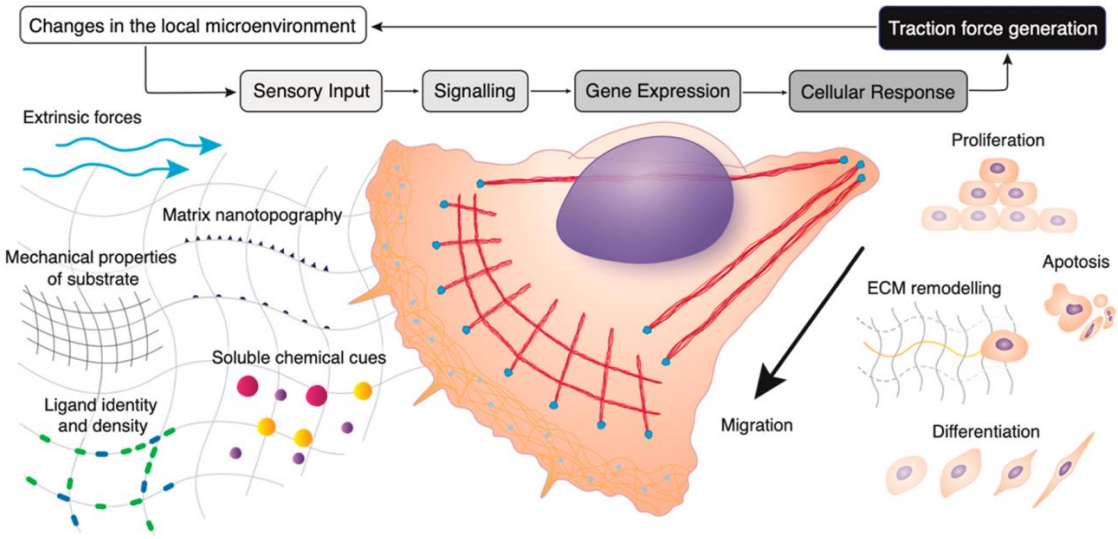

Figure 1.1 Cell-generated forces: important messenger for cells to probe their surrounding microenvironments, communicate in between cells, and respond to external stimuli accordingly [12]**.**

1.2 Dynamic Equilibrium and Couplings in Biological Systems

For a biological system to function properly, dynamic equilibrium needs to be reached. It is established by the coordinated interplays between biomechanical, biochemical, and bioelectrical properties (**Figure 1.2**). Take the excitation-contraction coupling of skeletal muscles as an example, the action potential (AP), which is the membrane potential generated by the movement of ions, will transmit the electrical signal to the neuromuscular junctions. The neuromuscular junctions are connected to sarcoplasmic reticulum (SR). Upon receiving the electrical signal from neural system, the calcium ions stored in the SR will be released and subsequently trigger the flow of calcium ions to myofibrils. Then, calcium ions will bind to the regulatory proteins on the actin filaments and therefore allow the myosin to attach to the binding sites of actin. The sliding movement between actin and myosin causes the muscle fibers to contract and become shorter [13]. Hence, unbalance of either biomechanical, biochemical, and bioelectrical properties can break the chain, subsequently interrupting the associated downstream events. For example, disorganized electrical signal in heart chambers will lead to irregular contraction and relaxation of cardiac muscles [10], [11]. Therefore, the abilities to monitor the dynamic changes of a biological system can provide transformative insights of physiological cellular functions, disease development/evolution, and signaling pathways between cells.

In a multicellular structure, bio-signals are transmitted between cells, and the signals can propagate across a large area within a short time. To be more specific, some typical conduction velocities are: 50 to 70 meter per second [14], [15] for nerve fibers, and 0.1 to 0.3 meter per second for cardiomyocytes [16], [17]. As a result, measurement approaches that can cover a large area will be invaluable to capture the dynamics of the propagating signals. Meanwhile, it is also pivotal

to have sufficient spatial and temporal resolution to locate the abnormal and heterogeneous sub-areas.

Furthermore, simultaneous measurements of several parameters are of great interest to study the complex interrelations and coupling between biomechanical, biochemical, bioelectrical, and other physiological properties. For example, optical mappings of transmembrane potential and calcium ions concentration concurrently can help us obtain comprehensive insights into the excitation-contraction coupling mechanism and investigate the pathological evolution of certain diseases [18]. Therefore, multi-parametric measurement is a vital tool to better understand the sophisticated coupling nature of numerous physiological events and activities.

Large-area dynamic changes of bioelectrical and biochemical properties are often measured by conventional optical mapping using fluorescent dyes or the microelectrode array techniques. These techniques will be discussed in detail in **Section 1.4**. On the other hand, while the tools to measure dynamic changing of bioelectrical and biochemical properties are well-established, the tools to measure large-area dynamics of biomechanical properties, specifically refer to cellular traction forces, are still lagging a lot behind. Most of them are limited to single or a small number of cells (see **section 1.3** for further discussions).

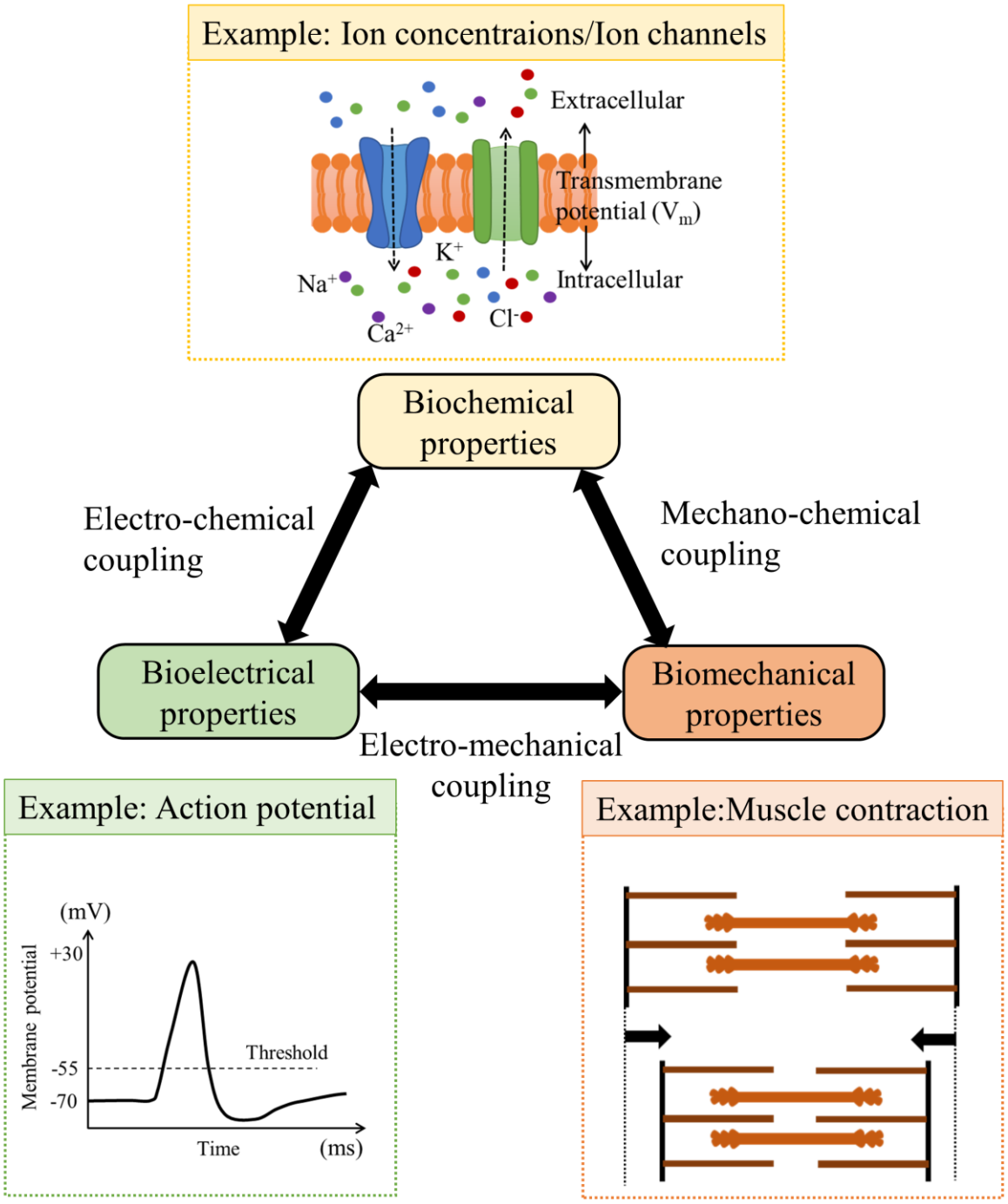

Figure 1.2 Dynamic equilibrium and coupling in a biological system: biochemical, bioelectrical, biomechanical properties and their couplings.

1.3 Existing Techniques for Measuring Cell-Generating Force

1.3.1 Traction Force Microscopy

Traction force microscopy (TFM) is the most historic and common technique to quantify cellular traction forces. Two-dimensional (2D) TFM involves tracking the movements of fluorescent beads embedded in an elastomeric substrate where cells are adhered on, as illustrated in **Figure 1.3 (a)** [19]. When cells apply forces on the elastomeric substrate, the embedded beads, serving as fiducial markers, will move accordingly. By comparing the beads' positions with and without cells, the displacements of beads induced by cellular traction can be calculated. Then, using the known young's modulus of the substrate, the traction force can be obtained. The same principle based on tracking the movements of beads can be extended to a three-dimensional (3D) situation, where cells are embedded in 3D extracellular matrix (ECM) or ECM-like materials and the displacements of the beads are recorded in all three axes (**Figure 1.3 (b)**) [19].

The advantages of TFM include its intuitive principles and its ability to provide sub-cellular resolution. TFM has been used in many studies to investigate cellular traction forces for different cell types [20], [21]. However, since the beads are typically dispersed randomly in the elastomeric substrate, the requirement of a reference image (image without cell) severely restricts their uses in many applications where continuous monitoring of the cellular traction force is necessary. Evaluations of long-term effect of drug and observations of stem cells differentiation are two examples. Additionally, the computations of TFM are very sensitive to experimental noise. In other words, a small error in the displacements from experiments can render dramatic error in the calculated traction force. Therefore, algorithms such as filtering and regularization are often needed to precisely reconstruct traction force. This significantly increases the computation effort and makes it difficult to be used as a generalized tool in every laboratory. Furthermore, to

accurately pinpoint the fluorescent beads and monitor their movements to acquire the desired beads displacements, high magnification objective lens is demanded in TFM, thereby limiting its field-of-view and throughput. A TFM can typically handle less than 50 cells per experiment and have field-of-view < $1mm^2$ in order not to sacrifice sub-cellular resolution [21], [22].

Recent developments of TFM include novel tracking algorithms to improve spatial resolutions [23], [24], reference-free TFM [25], [26], and new elastomeric materials [27]. However, due to the inherent tradeoff between spatial resolution and field-of-view of TFM, it is not a promising candidate to capture large-area biomechanical dynamics. For example, in [28], the authors propose a novel elastomeric sensor surface called "Fluorescently Labelled Elastomeric Contractible Surfaces (FLECS)". It consists of adhesive micropatterns uniformly embedded into an elastomeric film (**Figure 1.3 (c)**). Although the throughput is dramatically increased (reported to be 100-fold improvement), this sensor is limited to the study of single cell.

1.3.2 Elastic Micropillars

Elastic micropillars, with the schematic shown in **Figure 1.3 (d)**, use the deflections of micropillars array to quantify the traction force induced by the cells adhered on top. The bottom end of each pillar is fixed while the top end is free to move. The top end is often functionalized with ECM proteins to promote cell adhesions. The pillars are usually fabricated using regular patterns with pre-defined spacings, namely, using periodic structures. Hence, unlike traditional TFM, undeflected locations of pillars are known and a reference image is not needed. Because pillars are discrete and physically separated, each pillar deflects independently of others. This decouples the forces at each location and simplifies the calculation of traction force. To be more specific, with a known spring constant according to the geometry and material of pillars, classical beam theory can be directly applied to obtain the traction force exerting on each pillar [29].

Consequently, the computation is much more simplified compared to the traditional TFM. Although elastic micropillars approach features the strengths that references images are not required and the calculation of traction force is straightforward, it doesn't get the benefits without cost. In particular, the unnaturally discontinuous surface created by discrete pillars greatly impacts the morphology, size, and distribution of focal adhesion, thereby changing the physiological traction force of cells [30].

Recent advancements of the elastic micropillar approaches include further enhancement of spatial resolution using nanopillar arrays (pillar diameters are approximately 0.5um) [31] , double-sided pillar arrays to study the traction force in a 3D environment [32] and a plasmonic micropillars platform to increase the field-of-view [33], to name just a few. Specifically, the plasmonic micropillars platform proposed by [33] highlights a self-organized gold nanospheres implanted into the pillar tip. The gold nanospheres function as a strong scattering point. Therefore, it allows the tracking of pillar deflection via a low-magnification objective lens while maintaining the spatial precision. The authors present a FOV of 448 μm by 333 um with 30 nm spatial resolution using a 20x objective lens. Although with an extended field-of-view compared to other pillar-based platforms, to fully capture the transient biomechanical dynamics, this field-of-view is still not large enough with respect to the speed of bio-signal propagation. Furthermore, the gaps between the pillars make it an uneven surface, which is unphysiological for cell adhesion.

1.3.3 Optical Moiré Technique

A Moiré pattern generally refers to the interference pattern when periodic structures are overlapped with a slight offset in space (either translationally or rotationally). Benefiting from its high sensitivity in small spatial displacement fields, it has been adopted and utilized in a lot of applications to measure the surface deformation and thermal strains [34]. Using optical Moiré

effect to measure the cell-generated traction force has been proposed. A schematic of the platform is displayed in **Figure 1.3 (f)** [35]. The Moiré pattern is generated by the coherent light beam passing through two elastic substrates with periodic patterns. The cells are seeded on one of the substrates. By observing the Moiré pattern changes, the displacements created by the cells on the elastic substrates can be revealed.

The advantages of this method include that the Moiré pattern can be visualized in real-time, and it is a reference-free approach compatible with long-term traction force monitoring. In addition, the calculation of traction force is based on taking the Fourier transform of the Moiré pattern to estimate the offset from periodic structures. Therefore, it can bypass the tedious step to pinpoint the location of each sensing unit. However, this technique is only applicable to study a small number of cells. As the cell numbers increase, the effects of the deformations on Moiré pattern will couple to each other. The complicated interference will make the Moiré patterns not resolvable. Consequently, it becomes impossible to identify the location of the deformation induced by the cellular traction force.

1.3.4 Molecular Sensors

Based on a completely different mechanism, molecular sensors sense force through fluorescent resonance energy transfer (FRET). It is used in adhesion proteins and has been demonstrated to quantify forces transmission for proteins include vinculin [36] , talin [37], and E-cadherin [38]. As shown in **Figure 1.3 (g)**, the protein of interest is encoded with a mechanically calibrated linker between two fluorophores. The two fluorophores form a donor/acceptor fluorescent resonance energy transfer pair. When forces are applied to the molecule, it stretches the linker and alters the distance between the donor and acceptor. The increasing distance will lower the FRET efficiency, thereby resulting in a fluorescent signal due to the applied force.

Molecular sensors allow force quantification at pN regime and single molecular level. Although it can provide force magnitude experienced by molecules, no information about force direction is available. Furthermore, small field-of-view, low signal-to-noise ratio and the lengthy synthesis processes for specific molecular pairs are some drawbacks associated with this approach.

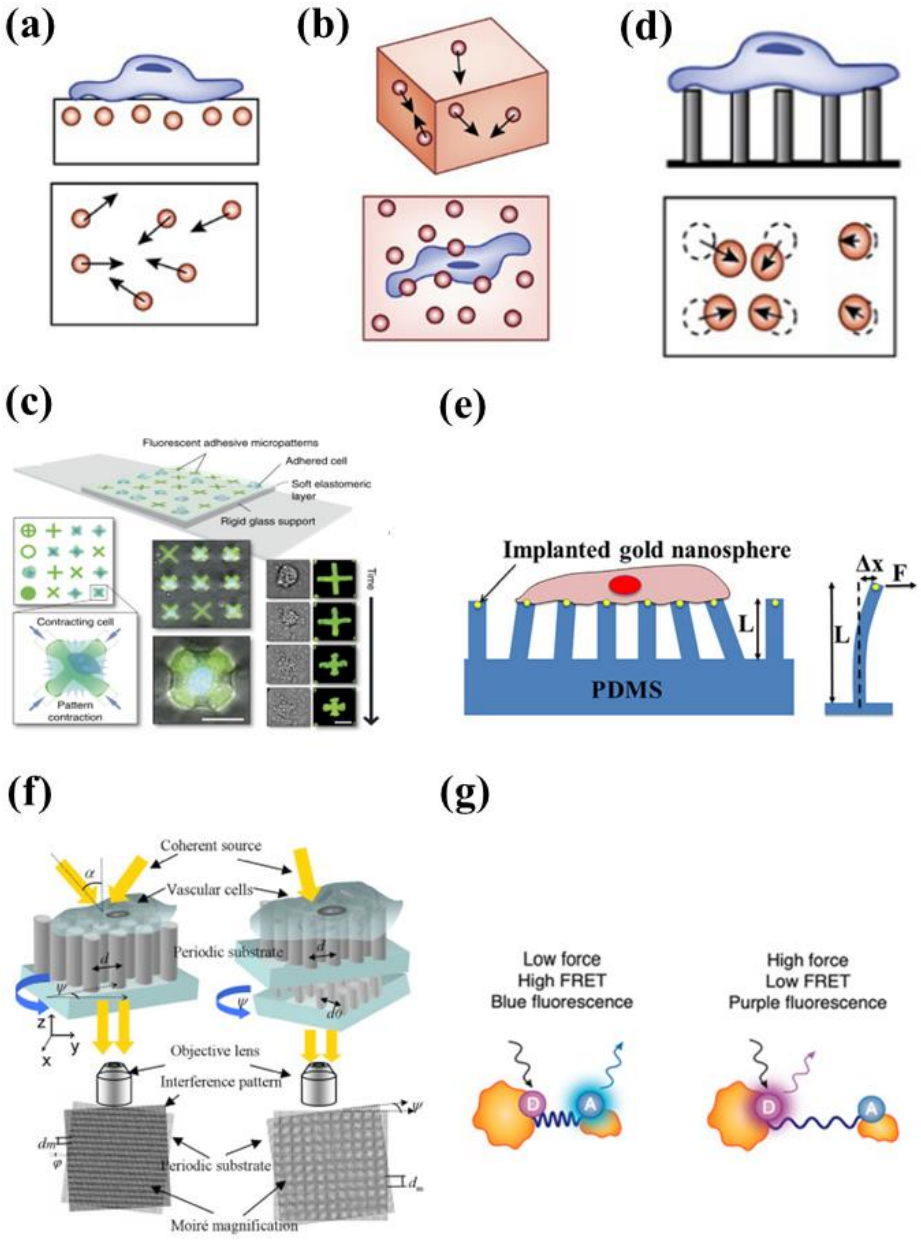

Figure 1.3 Existing techniques for measuring cell-generating traction force (a) 2D-TFM (b) 3D-TFM [19] **(c) FLECS** [28] **(d) elastic pillars** [19] **(e) gold-coated disk micropillars** [33] **(f) Moiré pattern** [35] **(g) molecular sensor** [12]**.**

1.4 Existing Techniques for Measuring Large-Area Cellular Dynamics

1.4.1 Planar Microelectrode Array

Planar microelectrode array (MEA) is a versatile tool that can be utilized in a variety of biosensing applications such as electrophysiology and electroanalytical chemistry [39]. As shown in **Figure 1.4(a)**, a MEA often consists of multiple electrodes patterned on an insulating and biocompatible substrate. Each electrode can measure the extracellular membrane potential generated by the concentration gradient of ions across the membrane of cell. Therefore, it has been used in a lot of research to record the electrical activities of electrically active cells such as neurons or cardiomyocytes. A MEA can also be adapted to measure chemical compositions via potentiometric, conductometric or voltametric approaches.

Benefited from the rapid developments of nanofabrication and CMOS technology [40], high-density microelectrode arrays with sub-cellular resolutions are available. For example, a MEA with 128 x 128 pixels and 7.8 μm x 7.8 μm pitch has been reported to record neural activity [41]. In addition, a MEA features the unique characteristic that it can be integrated with different electronic circuits on chip. Some common circuits used for MEA include multiplexers, amplifiers, filters, and FPGA (Field Programmable Gate Array) interface. Furthermore, there exist bidirectional electrodes that can deliver voltage or current stimulus to the sample, equipping a MEA the capability to record and stimulate at the same site [42]. Lastly, another great advantage of a MEA is that it doesn't perturb the physiological condition of the sample as the fluorescent dye technique does. Hence, it allows continuous observation of the same specimen for an extended period.

Despite the aforementioned strengths, MEAs still carry some drawbacks. First, the complexity of the device scales significantly with the number of electrodes. Most commercial

MEAs have 16x16 pixel numbers (256 electrodes) or less. Although the layout of electrodes can be readily adjusted so that a few electrodes cover a large field-of-view, the spatial resolution will be greatly compromised. On the other hand, the inherited tradeoff between noise level and spatial resolution of a MEA is unavoidable. Therefore, as the spacing between electrodes reduces, the signal quality is hugely deteriorated. Moreover, what MEAs measure is the extracellular membrane potential, which may be slightly different from the parameter we are really interested in, the intracellular membrane potential. Additionally, external stimulus delivered by the electrodes may create noise and cause artifacts in the measured signal. The pacing signal required for some cardiac preparation is an example that can potentially corrupt the measurement.

To sum up, although being an excellent choice for studying long-term and large-area bioelectrical and biochemical dynamics, the spatial resolution is sometimes not adequate enough to reveal the localized heterogeneities such as the abnormal contraction region of cardiomyocytes and the conduction block of neural signal transmission.

1.4.2 Optical Mapping Using Fluorescent Dyes or Genetically Encoded Sensors

As an alternative to the planar microelectrode array, optical mapping uses parameter-sensitive fluorescent dyes to obtain direct images of the electrical activity or ion concentrations in the cellular network [43], [44]. It is often used in the study of cardiac or neural system for action potential propagation or time course calcium transient. A typical optical mapping setup is shown in **Figure 1.4 (b).** The operation principle is articulated as follows. The excitation light, with the wavelength matched to the excitation spectrum of the fluorescent dye, will illuminate the dye-loaded sample. The emission light from the dye, with its wavelength red-shifted with respect to the excitation light, will be detected on the image detector after appropriate filtering. The parameter-sensitive fluorescent dyes used for optical mapping can be mainly classified into two

categories: voltage-sensitive dyes and ion-sensitive dyes [45]. Voltage sensitive dyes are a kind of potentiometric sensor. Their fluorescent output changes with the transmembrane potential. Some frequently-use voltage sensitive dyes include di-4-ANEPPS, di-4-ANBDQBS and RH237. On the other hand, ion-sensitive dyes are responsive to the intracellular ion concentrations. The most common one used in optical mapping is calcium dyes. This is because calcium ions are essential precursors of muscle contraction and play a pivotal role in the excitation-contraction coupling mechanism of muscle cells. Rhod2, Rhod4 and Fluo4 are some examples of the calcium dyes used in optical mapping. Simultaneous measurements of electrical activity and calcium ion concentration using optical mapping have also been reported [18], [46]. Other fluorescent dyes that have been utilized in optical mapping include sodium dyes (SBFI), potassium dyes (PBFI), and PH dye (SNARF-1).

Compared to the microelectrode array approach introduced in **Section 1.4.1**, optical mapping can provide a better spatiotemporal resolution. This is mainly benefited from the massive pixel number and fine pixel size of modern image detectors, especially refer to the rapid complementary metal oxide semiconductor (CMOS) sensors. Therefore, it is a great tool to visualize the fast dynamics of bioelectrical or biochemical activities over a large area. However, optical mapping has its own challenges to address. First, the fractional change of fluorescent dyes is small (usually less than 30%). Consequently, to achieve sufficient signal quality and the desired high speed, specialized cameras with extended pixel size are often needed. This will deteriorate the spatial resolution and increase the cost of the system, making it impractical to be generalized used. Secondly, photobleach and phototoxicity remain a serious issue. It not only limits the allowable observation time (usually within a few hours), but also changes the physiology of the cells. Thirdly, to reduce motion artifact, contraction inhibitors such as blebbistatin are often

applied during experiments to decouple the electrical activity and mechanical movement. Although there are some studies suggesting that the contraction inhibitors do not have direct impacts on the electrical activity of cells, side effects of those contraction inhibitors on cells are still under debate [47]. Hence, the measurements are often criticized to be unphysiological. To be more specific, mechanically uncoupled myocardium will have lower energy and oxygen consumption. Plus, no bidirectional interactions between electrical and mechanical activities are present.

Alternatively, genetically encoded sensors that are responsive to voltage or calcium can replace the function of fluorescent dyes in optical mapping. Genetically encoded voltage indicator (GEVI) such as QuasAr1 and ArcLight and genetically encoded calcium indicator (GECI) such as GCaMP series have been successfully adopted in the optical mapping [48], [49]. Despite the facts that they don't have phototoxicity issue and can extend the experiment time, the response speed of those indicators is relatively low. As a result, signals may be distorted and not represent the truth when measuring fast biological events.

1.4.3 Optical Grating Surface

To visualize the beating behavior of cardiac cells over a large area, recently, a grating surface using elastomer PDMS is proposed (**Figure 1.4 (c)**) [50]. PDMS grating with different young's modulus was fabricated using CD disks as mold. A thin layer of platinum is coated on the PDMS surface to enhance the reflectivity and contrast. Confluent layer of cardiomyocytes is seeded on the PDMS grating surface. External lamp illuminates the grating surface at an oblique angle. As the cardiomyocytes beat and apply force on the PDMS, the grating surface will be deformed, thereby deflecting the angles of diffracted light at different wavelengths. Hence, color change can be utilized to observe the change of beating patterns.

Although this device allows visualization of beating pattern in real time over a large area (2cm x 2cm), the poor spatial resolution and signal-to-noise ratio severely limit its applications. In addition, since the reflections from the grating surface are all coupled together, it is impossible to discern the location where cells apply traction force. What we can observe is a global trend superimposed by all the diffraction and scatter light. Hence, although the beating pattern over a large area can be visualized and it is a direction indication of biomechanical dynamics, it is not possible to find the heterogenous locations and wave propagation.

1.4.4 Diffractive Optical Tracer (DOT)

Recently, driven by the motivations to profile cell-generated force over a large area, a platform called "Diffractive Optical Tracer (DOT)" is proposed [51]. The schematic is shown in **Figure 1.4 (d)**. An array of micromirrors with reflective grating structure is used to measure the cell-generated traction force through the color spectra. When cells apply force on the surface, the grating disk will tilt, therefore changing the color spectra. Consequently, cell-generated force can be retrieved by the change of color spectrum. Unlike the optical grating surface approach mentioned in **Section 1.4.3**, each grating disk is optically decoupled. Thus, the spatial location of force can be readily resolvable as they are not coupled together. Cellular force measurement with field-of-view up to 4.8mm x 2.7mm and sub-cellular resolution have been reported. The capability of recording mechanical wave propagation is also demonstrated successfully using neonatal rat ventricular myocytes (NRVMs) syncytium.

However, there are some drawbacks associated with this platform. First, to obtain the direction of force, two LEDs need to be switched back and forth between x and y axes. This results in a reduction of the maximum achievable frame rate and a time offset between the x and y components of force. Secondly, to distinguish from the color spectrum generated by the

micromirror tilting induced by cell-generated force, the use of color camera will deteriorate the spatial resolution. Thirdly, the sensitivity is limited to the detectable angle range. Beyond the 1st order or 2nd order diffraction, the spectra overlap. Therefore, if the grating disks tilt beyond the range, the tilting angles are not solvable. Lastly, the oblique incident angle makes the platform susceptible to alignment. Accurate positioning of LED, sample and camera are required, making it difficult to further scale up the field of view.

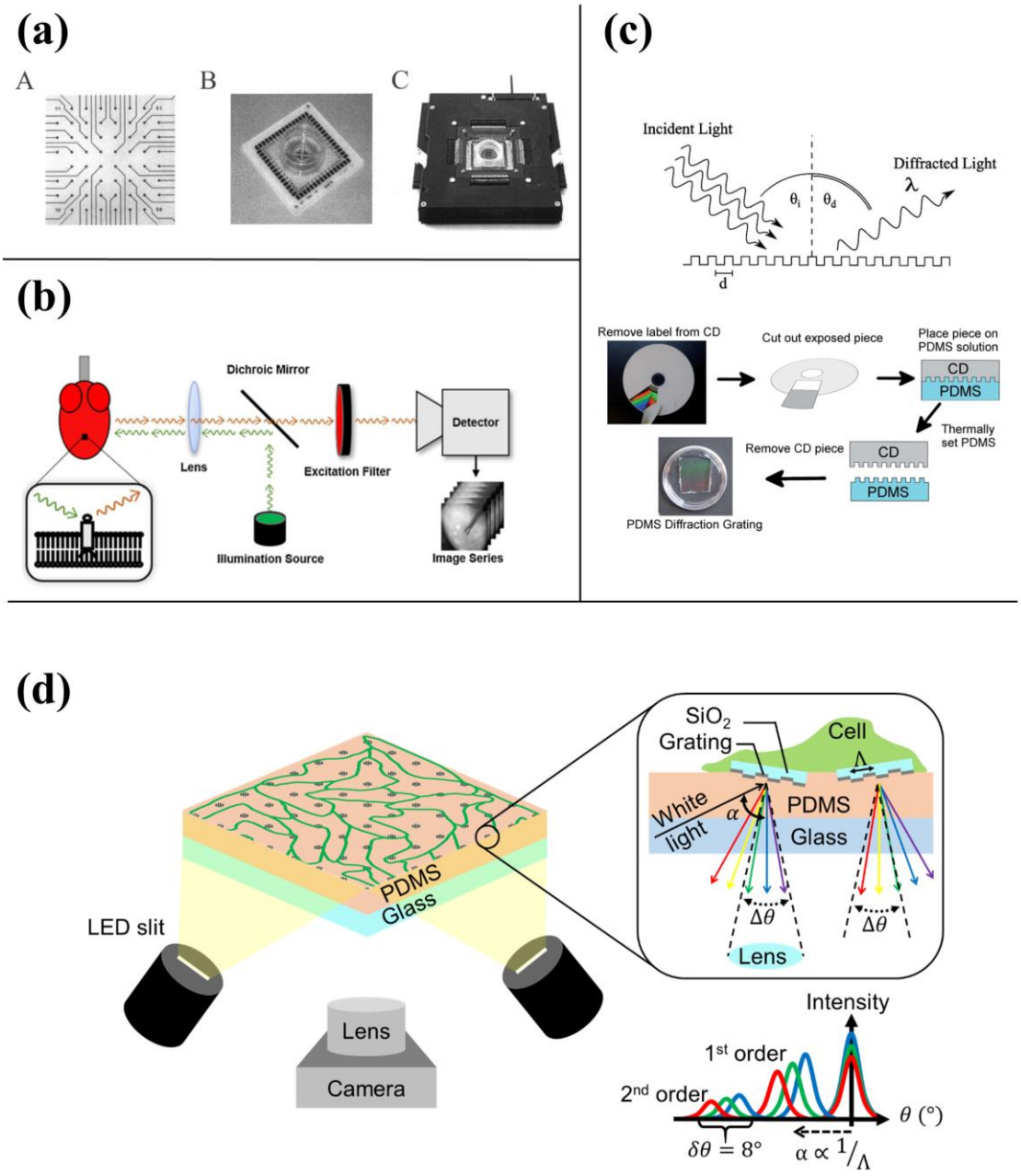

Figure 1.4 Existing techniques for measuring large-area cellular dynamics (a) planar microelectrode array (MEA), A: 8x8 layout electrode grid, B: substrate-integrated MEA culture dish, C: MEA amplifier [52] **(b) optical mapping using fluorescent dyes** [53] **(c) optical grating surface** [50] **(d) Diffractive Optical Tracer (DOT) based on diffraction grating** [51].

1.5 Conclusion

As described in **Section 1.3**, current existing technologies for measuring biomechanical properties, specifically refer to cell-generated force, have constraints on the observable area and the number of cells. Hence, it is not capable of capturing fast and transient biological events like neural signal transmission and cardiac muscle contractions. On the other hand, as introduced in **Section 1.4**, large-area profiling of bioelectrical and biochemical properties is accessible through either planar microelectrode array or fluorescent dye approaches. Nonetheless, they either do not have sufficient spatial resolution or they create additional unphysiological factors during experiments. Putting together, to fill the technology gap, we would like to develop a platform for large-area mapping of biomechanical properties in native and physiological condition. The success of this platform will offer transformative impacts on biological studies to investigate cell and tissue behaviors and the couplings between bioelectrical, biochemical and biomechanical properties.

Chapter 2 Large-Area Mapping of Biomechanical Dynamics via Array of Diffractive Elements (LAMBDA)

This chapter introduces our proposed platform for measuring large-area biomechanical dynamics of multicellular systems: "**LAMBDA**" (Large-Area Mapping of Biomechanical Dynamics via Array of diffractive elements). The schematic, design, simulation, fabrication, and characterization of the LAMBDA platform will be covered.

2.1 Platform Schematics

The schematic of the proposed LAMBDA platform is shown in **Figure 2.1**. The platform utilizes a massive number of optical diffractive elements embedded periodically in an elastic membrane (polydimethylsiloxane (PDMS)) to track the traction forces generated by the cells seeded on top. The working principle is elaborated as follows. A collimated light beam, emitted by a single-wavelength light-emitting diode (LED), illuminates the diffractive elements and the transmitted diffraction patterns of each element are detected on the image sensor below. When cells apply traction forces on the PDMS membrane, the induced lateral displacements can be monitored by the changes of the transmitted intensities and diffraction patterns from each diffractive element projected on the image sensor.

The diffractive element is a key component in the LAMBDA platform. It needs to translate the lateral displacement induced by the cell-generated force to discernible changes that can be measured by the image sensor. As shown in **Figure 2.1**, the single unit of a diffractive element

consists of a circular metal disk on the top layer of PDMS and a metal sheet with central circular aperture at the bottom. In other words, the top and bottom metal layers form a complementary shape in terms of its opacity but are offset vertically by the PDMS membrane. Since the bottom metal layer is on the glass substrate, its movement is restrained. Without any applied force, most of the illuminated light is blocked. Only a small portion of light diffracted from the edge can penetrate. When cells exert traction force on the PDMS membrane, the top metal will move accordingly while the bottom metal remains fixed. The relative movements of the top and bottom metal layers will create eclipse-like apertures with different sizes for each diffractive element while looking from top (**Figure 2.1 (c)**). The transmitted light intensity and the diffraction pattern are direct indication of the cellular traction force applied on the PDMS membrane. To calculate the resultant diffraction patterns from different aperture shapes, the diffraction theory and the simulation approaches will be illustrated in **Section 2.2**.

There are several unique advantages of the proposed LAMBDA platform compared to the existing technologies for measuring biomechanical properties, especially referring to traction force measurement. First, for conventional traction force microscopy (TFM), force-induced displacements of beads or pillars are directly tracked. This often requires a high-magnification objective lens or large numerical aperture (N.A.) optics to accurately resolve the minute displacements of beads or pillars, thereby greatly limiting the observable region. By contrast, via the optical diffractive elements, the LAMBDA platform measures the changes of displacement-induced optical properties (transmitted intensity and diffraction patterns) as opposed to measuring the force-induced displacements directly (**Figure 2.2**). Therefore, the system does not carry the field-of-view (FOV) limitation imposed by the high N.A. optics. Consequently, the LAMBDA platform can capture fast and transient biomechanical dynamics propagating over a larger FOV

with superior spatial resolution that is not achievable using traditional TFM. Secondly, no labeling chemicals such as fluorescent dyes are needed during measurements. Hence, the label-free nature of the LAMBDA platform can preserve native and physiological conditions of cells, enabling continuous and prolonged observation of biomechanical dynamics. Thirdly, the surface of the device is relatively flat. Unlike elastic micropillars approaches, no protruded structures or gaps are present on the devices used by the LAMBDA platform to alter the focal adhesions of cells. Finally, the integration of the LAMBDA platform and other microscopes is of great potential to allow simultaneous monitoring of biomechanical dynamics along with other cellular properties such as molecular configuration, transmembrane voltage, or ion concentration.

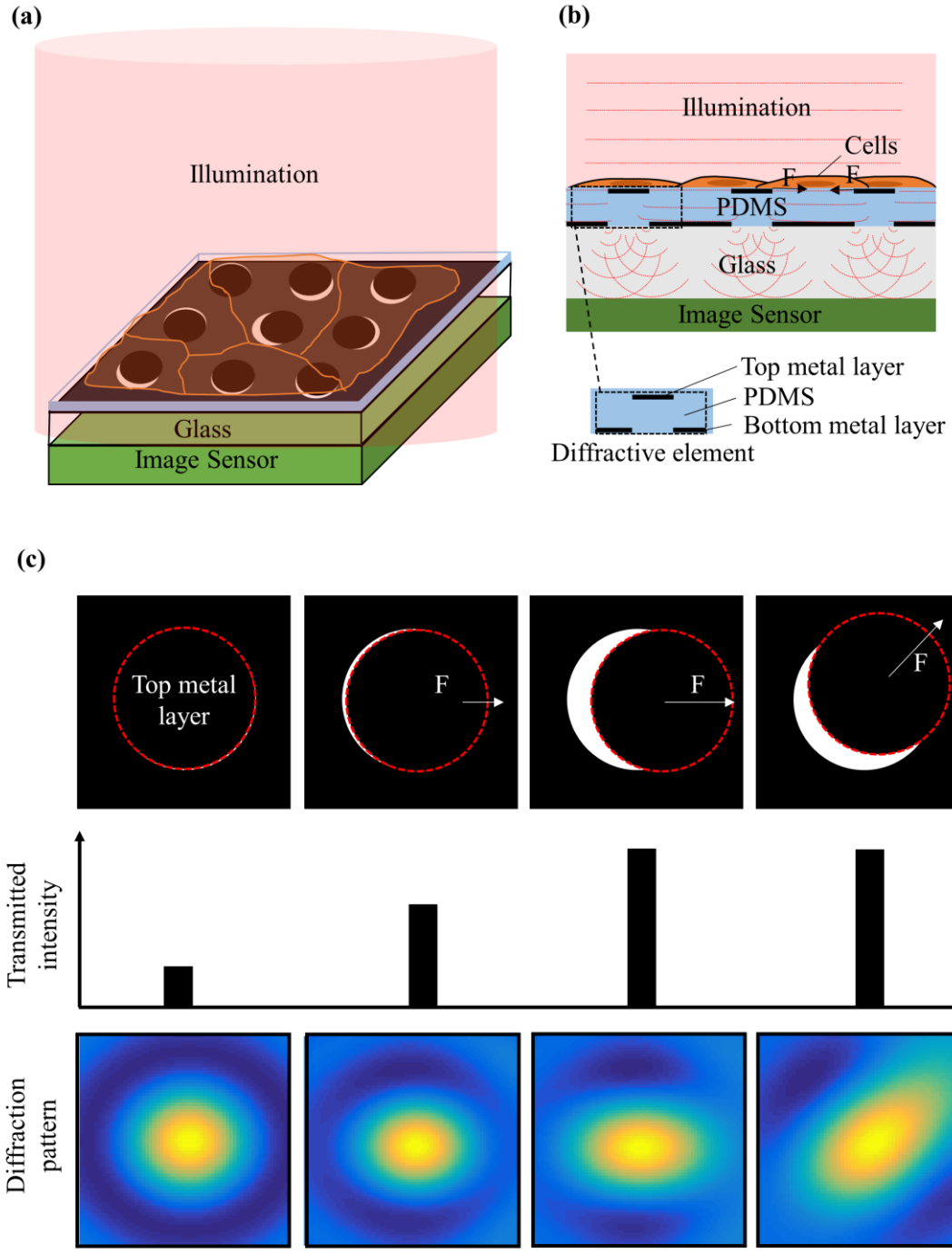

Figure 2.1 Schematic of the proposed LAMBDA platform (a) oblique view of the schematic (b) side view of the schematic (c) working principle.

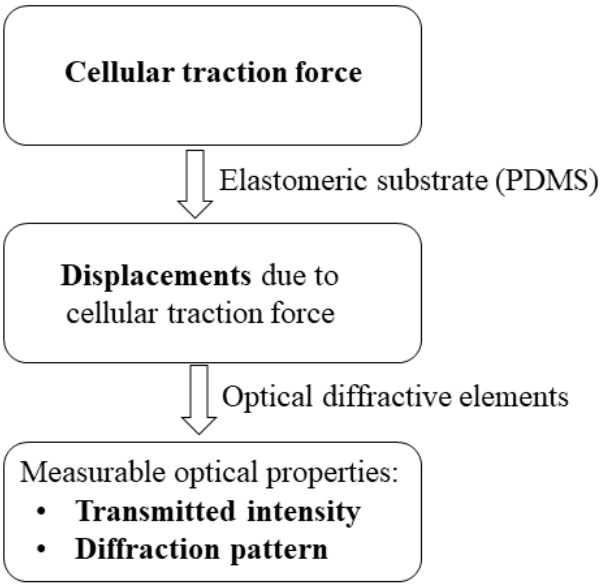

Figure 2.2 Idea of the optical diffractive elements used in the LAMBDA platform: convert the force-induced displacement to measurable optical properties.

2.2 Designs and Simulations of the Diffractive Elements

2.2.1 Diffraction Theory

Diffraction is a phenomenon when a wave passes through an aperture or an obstacle and result in the deviation of its rectilinear propagation that cannot be explained by reflection or refraction (i.e., geometrical optics) [54]. A classic example is the "single-slit diffraction" problem. The schematic is displayed in **Figure 2.3 (a)**. Single-slit diffraction describes the fact that when a wave passes through a narrow slit, alternative bright and dark fringes will be observed from a plane some distance away from the slit. This cannot be explained by geometrical optics. Hence, to account for the wave nature of light, Huygens–Fresnel principle is adopted. The principle states that each point on the wavefronts can be considered as a secondary wavelet, emitting spherical wave outward. The diffraction pattern is formed by the constructive and destructive interference of these wavelets at different locations on the observation plane.

A generalized schematic of a diffraction problem is present is **Figure 2.3 (b)**. An aperture is on the (ξ, η) plane (aperture plane). Light illuminates from the left-hand side of the aperture, and after passing the aperture, propagates to the right-hand side of the aperture. Our interest is the diffraction pattern on the observation plane (x, y) plane, located some distance away from the aperture plane. The notation, U, is adopted to represent any of the scalar components of electric or magnetic fields (i.e., E_x, E_y, E_z, H_x, H_y, H_z). To calculate the resulting patterns after a wave passing through an aperture or an obstacle, Fresnel diffraction formula can be used to link the field on the aperture plane U (ξ, η), to the desired field pattern on the observation plane U (x, y), through a surface integral. It can be written mathematically as

$$U(x,y) = \frac{\exp(jkz)}{j\lambda z} \iint_{-\infty}^{\infty} U(\xi,\eta)\ \exp\left\{j\frac{k}{2z}[(x-\xi)^2 + (y-\eta)^2]\right\} d\xi d\eta$$

(**Equation 2.1**)

where λ is the wavelength of the illuminating light, k is the wave number, and z is the distance between the aperture plane and the observation plane. Fresnel diffraction formula is specifically appliable in the near field, where the spherical wavefront is approximated by a parabolic shape. On the other hand, if the observation plane is far enough, Fresnel diffraction formula can be further simplified as Fraunhofer diffraction formula, where the planar wavefront is utilized. The mathematical form of the Fraunhofer diffraction formula can be written as

$$U(x,y) = \frac{\exp(jkz)\exp\left(j\frac{k}{2z}(x^2+y^2)\right)}{j\lambda z} \iint_{-\infty}^{\infty} U(\xi,\eta)\ \exp\left\{-j\frac{2\pi}{\lambda z}(x\xi + y\eta)\right\} d\xi d\eta$$

(Equation 2.2)

It should be noted that there are some assumptions associated with **(Equation 2.1)** and **(Equation 2.2)**. First, the wave should be in a linear, isotropic, homogeneous, non-dispersive and non-magnetic environment. Secondly, observation should be made at least several wavelengths away from the aperture. Thirdly, the diffracting structures should be larger than the wavelength. To sum up, if the above three conditions are satisfied, the diffraction patterns can be calculated using either **(Equation 2.1)** (near field) or **(Equation 2.2**) (far field).

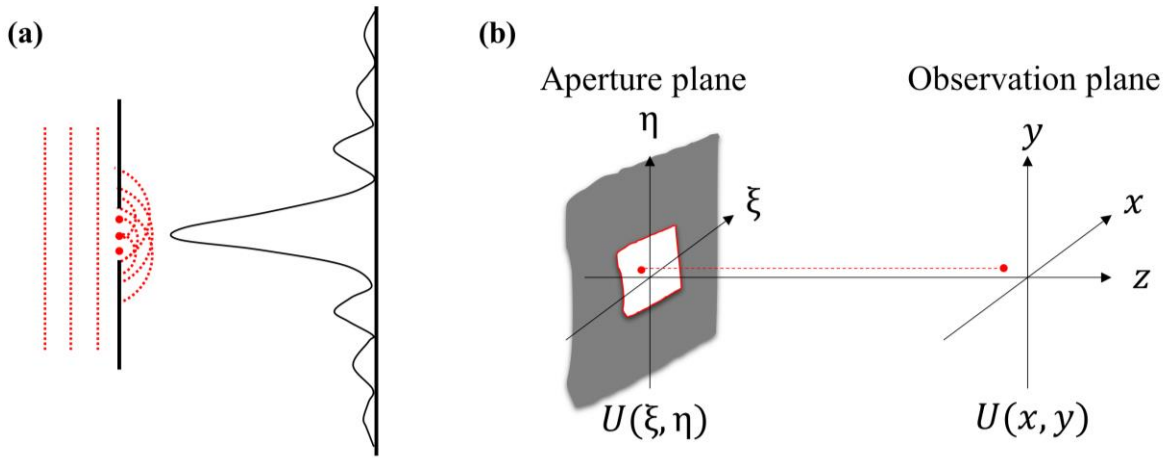

Figure 2.3 Schematics of a diffraction problem (a) single slit diffraction (b) diffraction formula.

2.2.2 Finite-Element Numerical Simulation

Since our diffractive element consists of a two-layers metal structure with discontinuities, it fails to meet all the assupmtions stated in **Section 2.2.1** that leads to the Fresnel diffraction formula. Therefore, we utilize a two-step process to calculate the diffraction pattern, as illustrated in **Figure 2.4**. The first step is to analyze the two-layer metal structure using a three-dimensional (3D) full-wave simulation software (Ansys Lumerical FDTD). By doing so, the effects of edges and discontinuities of the diffractive element on the diffraction pattern can be accounted for accurately. Afterward, the electric fields on the plane 2 um away from the bottom metal layer is exported from the full-wave simulation. This plane is regarded as the equivalent aperture plane for the second step. From there, Fresnel diffraction formula (**Equation 2.1**) is applied to obtain the diffraction pattern 100 um away from the bottom metal layer. Instead of the Fraunhofer diffraction formulam, we use the Fresnel diffraction formula here for better accuracy. The sufrace integral accosicated with the Fresnel diffraction formula is implemented numerically by a customized

MATLAB code. This process is validated by comparing diffraction patterns of a single-layer slit obtained directly from the Fresnel diffraction formula and the two-step simulation.

Using this two-step simulation, we can approximately predict the transmitted intensities and the diffraction patterns generated by different aperture shapes and dimensions. For example, total transmitted power (sum of transmitted intensities) with respect to various lateral displacements is shown in **Figure 2.5**. U and V denote the lateral displacements of the diffractive element in the x and y direction, respectively. Additionally, **Figure 2.6 (a) to (f)** presents the diffraction patterns with respect to different lateral displacements. The aperture shapes looking from top are displayed on the top right corner of each figure. The disk diameter is 8 um and the PDMS layer is 2um thick. The wavelength of the illumination light is 800 nm. It is clear that the center bright spot of the diffraction pattern can be a direct indication of the displacements. To be more specific, the elliptical ratio and the long axis direction of the center bright spot change with different lateral displacements U and V. Hereafter, if not explicity stated, the introduced two-step process is used to numerically analyze the diffraction pattern.

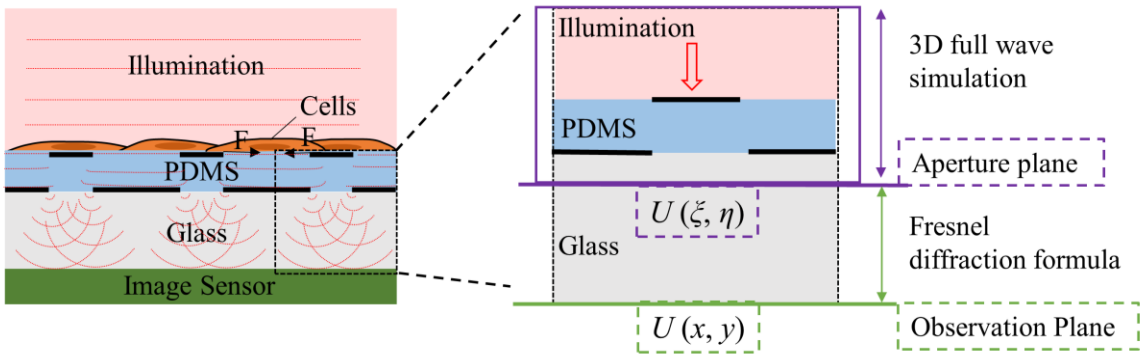

Figure 2.4 The two-step simulation process to calculate the diffraction pattern from the proposed diffractive elements.

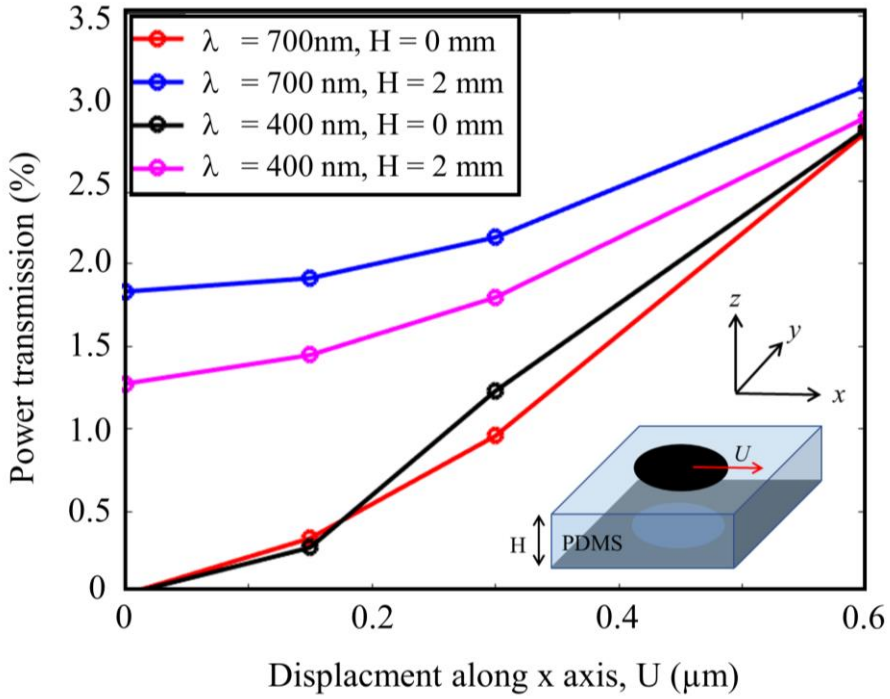

Figure 2.5 Total transmitted power (sum of transmitted intensities) of the diffractive element with respect to various lateral displacements.

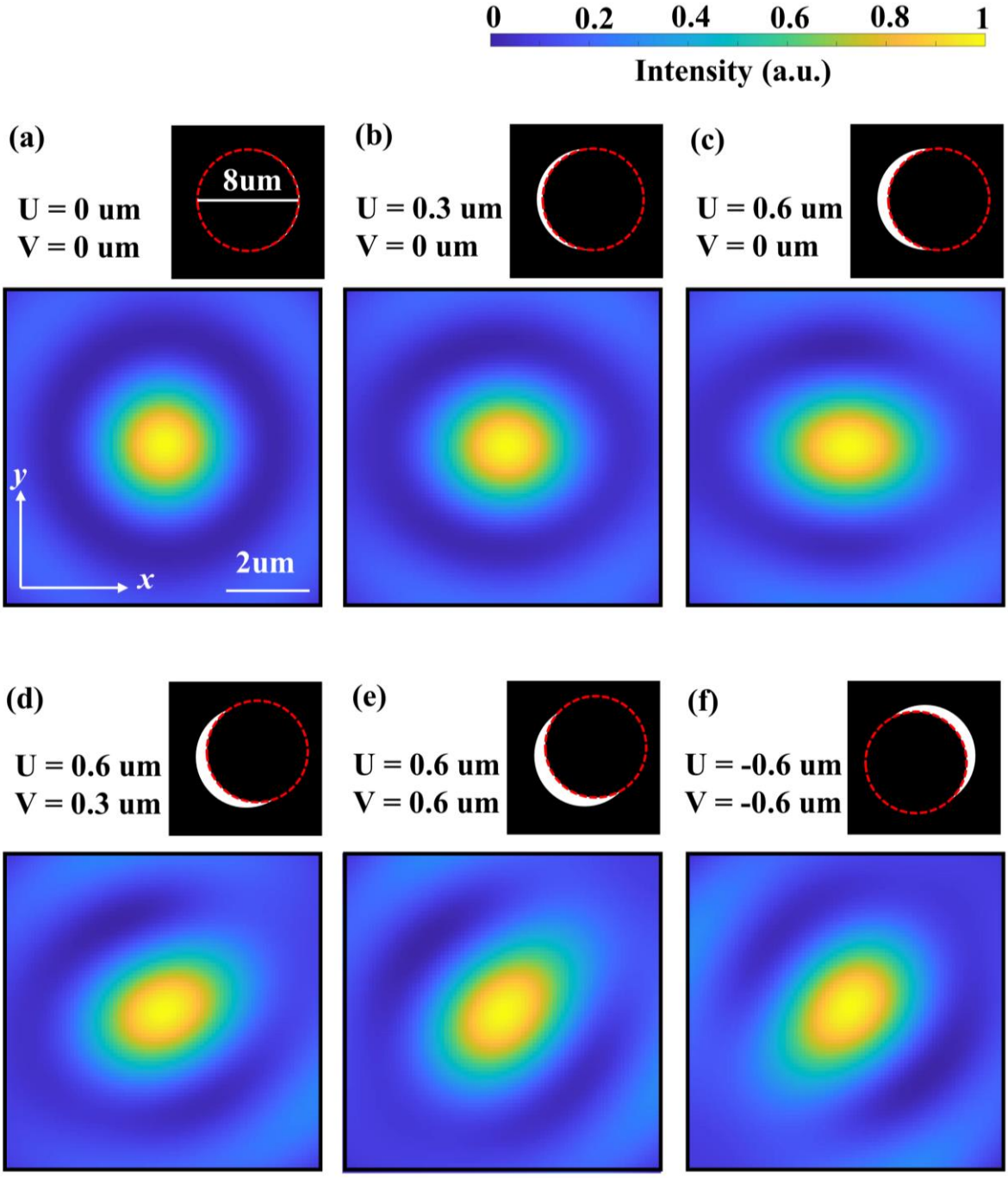

Figure 2.6 (a)-(e) Simulated diffraction patterns with respect to different lateral displacements.

2.2.3 Design Considerations of the Diffractive elements

This section discusses the design considerations of the diffractive elements. Specifically, shape, PDMS thickness, PDMS stiffness, disk size/periodicity and illumination wavelength will be addressed.

Shape In addition to the circular shape presented in **Figure 2.5** and **Figure 2.6**, other shapes such as circular ring, square and square ring are potential candidates for the diffractive elements (**Figure 2.7 (a)**). Meanwhile, the top metal layer and the bottom metal layer can be swapped, creating the so-called "center-top" and "center-bottom" configuration, as demonstrated in **Figure 2.7 (b)**. The center-top configuration has the benefit that the top metal layer of each element is physically disconnected. Therefore, upon the exertion of the cellular traction force, it is easier for each individual element to move. For simplicity, circular shape with center-top configuration is selected as the first-generation prototype in this disseration. Howoever, it should be kept in mind that there are various designs of diffractive elements available.

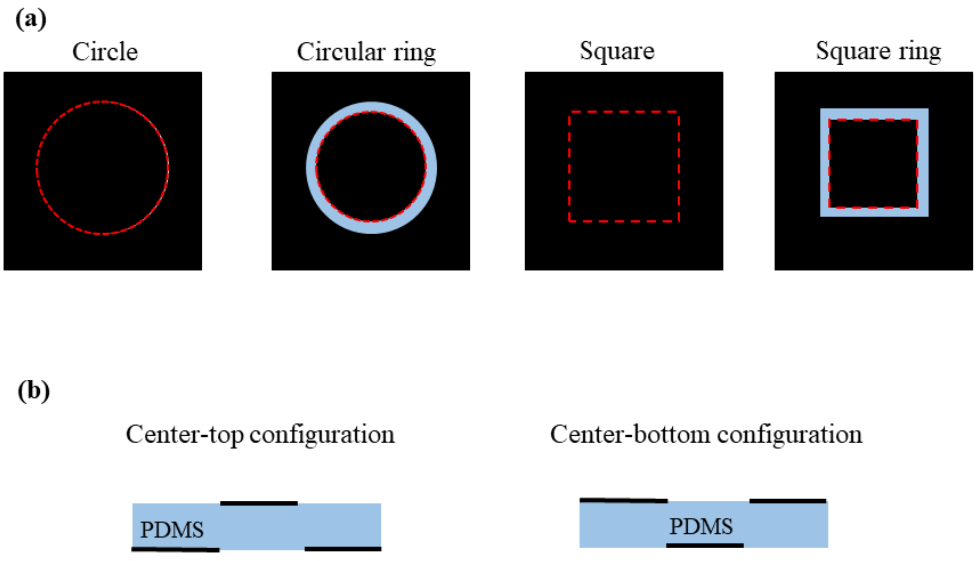

Figure 2.7 Potential shapes and configurations for the diffraction elements.

PDMS thickness For the design of our proposed diffractive element, PDMS thickness controls the offset distance between the top and bottom metal layers. This offset distance has significant impacts not only on the amout of light transmission but also on the optical sensitivity (change of the diffraction patterns with respect to the lateral displacements). Considering the extreme case that the offset distance drops to zero, the metal layer will completely block the light transmssion if there is no lateral displacements. Once lateral displacements appear to allow the passage of light, there will be a steep increase of the transmitted intnesity. This give the nature of the high optical sensitivity assoicated with thin PDMS layer. Next, let's consider the other extreme case that there is a huge offset distance between the two metal layers. This large distance in between the two metal layers will permit high transmission of light, creating a bright background even without any lateral displacements. Hence, changes of diffraction patterns with lateral displacments only contribute a minute amount to the exisitng bright background.

On the other hand, mechanical sensitivity (change of the lateral displacement with respect to the exerted cellular force) features an opposite trend against the optical sensitivity. More quantitative mechanical analysis will be detailed in **Section 2.2.4**. Intuitivly, the thicker the PDMS layer, the larger the indcued displacements under the same loading force, thereby giving its higher mechanical sensitivity.

To sum up, a device with a thin PDMS layer will have higher optical sensitivity but lower mechanical sensitivity, compared to a device with thick PDMS layer. In practice, the PDMS thickness is chosen to be 2 to 5 um as a decent tradeoff between optical sensitivity and mechanical sensitivity.

Disk size and Periodicity As in the case of traditional traction force microscopy, there exists a ultimate tradeoff between the disk size/disk periodicty and the spatial resolution. Namely,

smaller disk size and periodicity will render a better spatial resolution. In reality, however, the image sensor has a finite pixel dimension, therefore, the disk size/periodicty cannot be infinitesimal in order for the diffraction pattern being resolvable. Given the typical pixel dimension of a modern image senesor (1 to 4 um) and the averaged size of cells (e.x. A cardiomyocyte is about 100 um by 20 um), the devices used in the experiments have disk sizes and periodicity fall between 5 to 15 um and 20 to 40 um, respectively. These numbers are selected to ensure that the diffraction pattens are able to be resolved by the image senors while still maintaining the spatail resolution at cellular level.

Illumination Wavelength Theoretically, the size of the diffraction patterns at a given observation plane is proportional to the illumination wavelength (**Equation 2.1**). In other words, the shorter the wavelength, the smaller the diffraction pattern. Nevertheless, in practice, the diffraction pattern will be digitalized by the finite pixel size of image sensor. Therefore, the impact of wavelength on the diffraction is smoothed out. On the other hand, to avoid scattering and absorption of light from the biological sample, illumination wavelength with large penetration depth is favored. This spectrum window is usaully defined to be from 650 nm to 1350 nm, within which the penetraion depth reaches the maximum . Combining the above two points with the fact that the quantum efficiency of image sensor usually drops a lot for wavelength above 1um, red to near-infrared illumination (660 nm to 800 nm) is picked for our experiments.

PDMS stiffness In addition to the thickness of PDMS layer, the stiffness of PDMS layer also determine the amount of lateral displacements. Under the same loading force, the softer the substrate, the larger the displacements. However, for a biological system, cell-generate forces vary a lot with their micro-environment. It has been reported that cells tends to exert larger forces on harder substrate [55]–[57]. The relationship of the force and the substrate stiffness is complex and

nonlinear. Therefore, substrate stiffness is often chosen to mimic the physiological tissue environment whenever possible.

The stiffness of a substrate is characterized by the Young's modulus in the linear region of its stress-strain curve. Different stiffness of PDMS can be obtained by mixing Sylgard PDMS 184 and PDMS 527 with different ratios [58]. In the experiments for neonatal rat ventricular myocytes (NRVM), 50 kpa PDMS is used (mixture of PDMS 527 and 184 with ratio 10 to 1).

2.2.4 Solid Mechanics Simulation

To obtain an estimated range of displacements that may be induced by cells, finite-element solver (COMSOL Multiphysics, solid mechanics module) is utilized. First, we study the simplified case where a given stress (boundary load) is applied along a single axis (x-axis in the simulation) on the proposed diffractive element. **Figure 2.8 (a)** and **(b)** presents the resultant displacements under different boundary loads for PDMS thickness that equal to 2 μm and 5 μm**,** respectively. Moreover, for each PDMS thickness, several Young's modulus are swept. Unsurprisingly, thicker, and softer PDMS will have larger displacements compared to their thinner and stiffer counterparts under the same boundary load. Considering the typical magnitude of cell-generated force (1 nN to 300 nN) and stress (0.05 to 10 kpa) [12], [19], [59], displacements with sub-micron to micron order are to be expected for our platform. Additionally, it is worth mentioning that within this range, the PDMS still behaves as an elastic material (within the linear region of the stress-stain curve).

Next, we move to a more practical situation where a monolayer of cells exerts a two-dimensional (2D) stress on the substrate. To implement, a 2D random stress distribution is synthesized using Fourier series. The synthesized stress distribution is applied on the surface with an array of diffractive elements (**Figure 2.9 (a)**). An example of the stress distribution and the

resultant displacements of diffractive elements from a 5x5 disk array are given in **Figure 2.9 (b) and (c)**, respectively. The 2D simulation can help us study the mechanical coupling between diffractive elements. Moreover, it can serve as the data to build model for retrieving cellular traction force if the displacements of each diffractive elements can be extracted from the measured diffraction patterns.

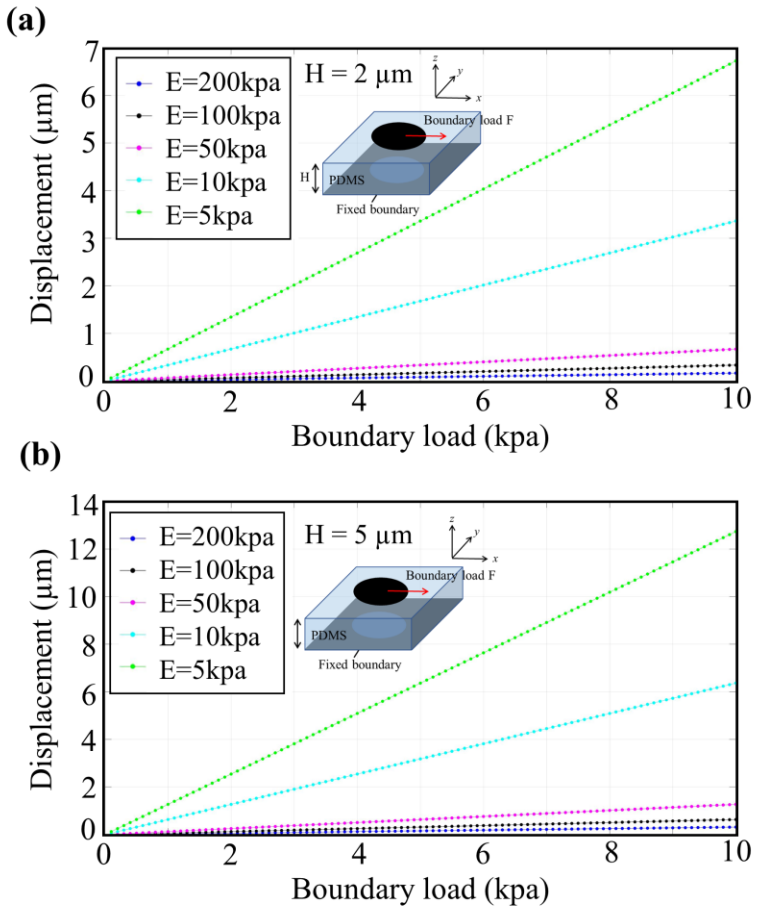

Figure 2.8 One-dimensional solid mechanics simulation to study the displacements of diffractive elements under different boundary load (a) PDMS thickness equals to 2 μm (b) PDMS thickness equals to 5 μm. Inset show the simulation schematics. (Disk diameter = 8 μm; E represents Young's modulus of the PDMS).

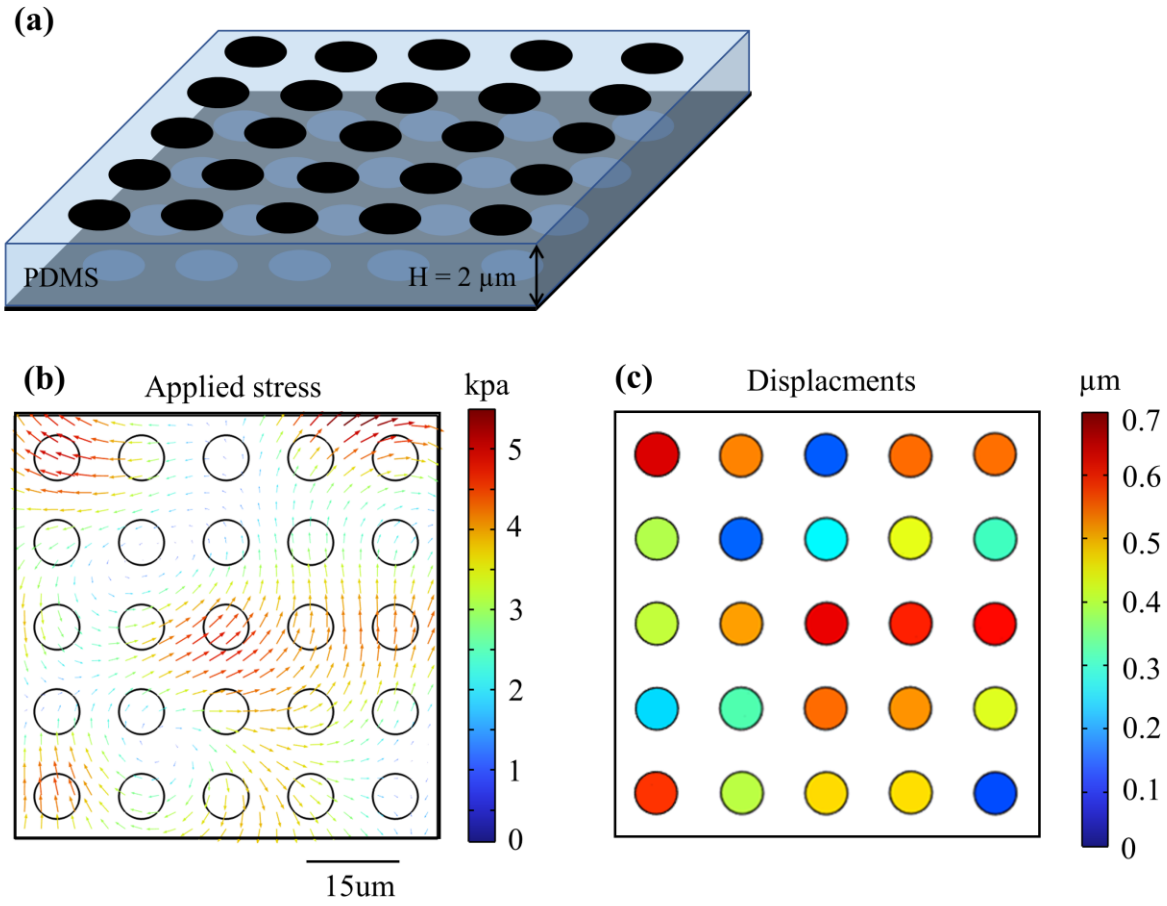

Figure 2.9 Two-dimensional solid mechanics simulation (a) Schematic of simulation (b) an example of the synthesized stress distribution (c) the resultant displacements of each diffractive element.

2.2.5 More Discussions

Digitalization of diffraction pattern by image sensor In practice, the diffraction patterns created by the diffractve element will be digitalized and converted to electrical signal by the image sensor. The principle of how a CMOS sensor works is briefly described as follow: A number of photons incident on each pixel of CMOS sensor will be converted to electrons and stored in the

well. The final reading of CMOS sensor will be proportional to the collected electrons in the well. The efficiency of this photon-electron conversion is called quantum efficiency and is dependent on the wavelength of incident photons. Intuitively, given the same photon flux density, the larger the pixel size, the more the photons a pixel can collect, thereby giving larger signal. However, as the pixel size increases, the features of diffraction pattern may be blurred and deteriorate the spatial resolution subsequently. The tradeoffs lie between pixel size and signal level. Besides pixel size, exposure time, the period during which the sensor collects photons will determine the signal level and limit the maximum sampling speed.

Cellular stiffness measurements In addition to cellular traction force, cellular stiffness is another critical biomarker to understand the physioloiglcal and pathological states of cells. The porposed LAMBDA platfrom is of great potential to be magneticially-actuated by incorporating magnetic metals to conduct large-area mapping of cellular stiffness.

2.3 Fabrication Process of the Devices (Array of Diffractive Elements)

The proposed device is fabricated using photolithography, isotropic metal deposition and PDMS stamping. The substrates are standard 1mm-thick glass slides. The fabrication process flow is given in **Figure 2.10** and summarized below. Detailed parameters for each step can be found in **Appendix A**.

(a): Patterning SU8 posts on the glass substrate.

SU8 posts serve as spacers and mechanical support for the subsequent PDMS stamping. They are patterned using standard photolithography.

(b): Patterning photoresist AZ5214

Photoresist AZ5214 is used to mold the PDMS. It is patterned using standard photolithography and aligned with the SU8 posts patterned in **Step (a)**.

(c): Stamping PDMS

Uncured PDMS is poured on the patterned substrate and covered by a polyvinyl acetate (PVA)-coated glass. PVA is a water-soluble polymer and is used as a sacrificial layer during the stamping process. A constant pressure (23 kpa) is applied on PVA-coated glass through a PDMS buffer. The device is left in the room temperature for at least 48 hours until PDMS is fully cured. Then, the PVA-coated glass is removed by soaking the whole sample in deionized water.

(d): Removal of PDMS residue

After the first PDMS stamping, reactive ion etching (Oxford RIE) is utilized to clean and etch the PDMS residue until photoresist AZ5214 is completely exposed. The etching speed is about 400 nm per min and the etching time is about 2.5 minutes.

(e): Removal of photoresist AZ5214

Next, the device is soaked into acetone solution and put in the ultrasound bath for 5 seconds to strip the photoresist AZ5214. The PDMS disks, which are the main component to create displacements, are formed after this step.

(f): Isotropic metal deposition

Electron beam evaporation is utilized to implement isotropic metal deposition (SLOAN, SL 1800). Aluminum is chosen due to its high reflectivity in visible and near infrared spectra. According to the working principle of the proposed diffractive element, however, any light-blocking material can be used.

(g): Stamping PDMS

Lastly, to ensure a flat surface, which is favored by most cells to develop focal adhesions physiologically, PDMS stamping process, the same as (c), is conducted again to fill PDMS to the air gaps in between PDMS disks. After removing the PVA-coated glass, the final device is shown in **Figure 2.10 (h)**.

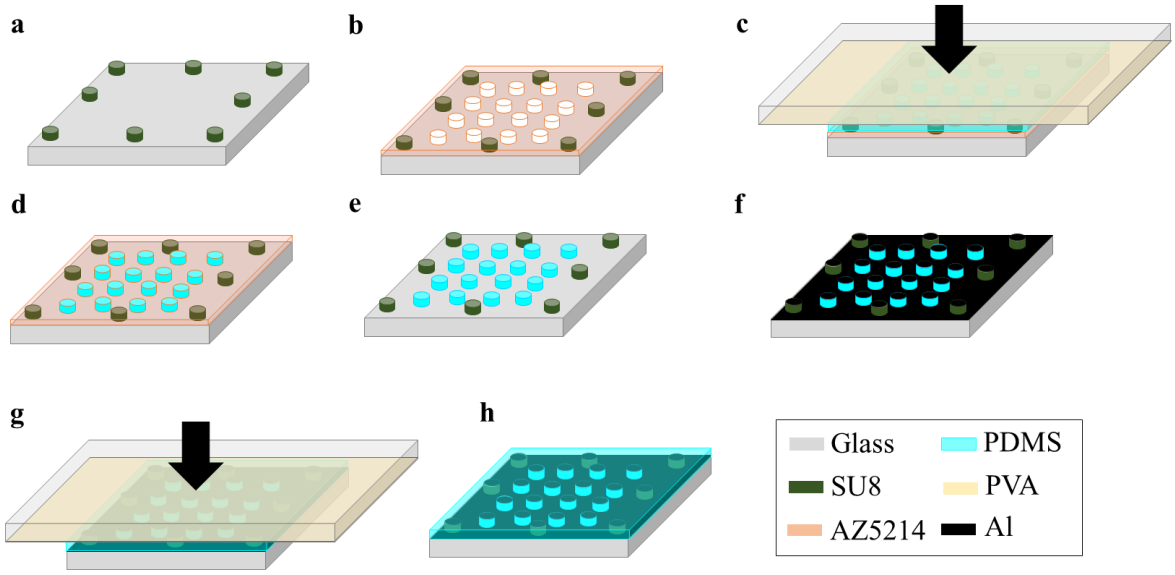

Figure 2.10 Fabrication process flow (a) patterning SU8 posts (b) patterning photoresist AZ5214 (c) stamping PDMS (d) removal of PDMS residue (e) removal of photoresist AZ5214 (f) isotropic metal deposition (g) stamping PDMS (h) final device.

2.4 Characterization

2.4.1 Measured Diffraction Patterns using the LAMBDA platform

Figure 2.11 displays the microscope photos of a fabricated device and **Figure 2.12** presents the device images measured in the LAMBDA platform. The SU8 posts form a grid surrounding the circular diffractive elements to provide uniform mechanical support during PDMS stamping. They are highlighted in orange color in one inset of **Figure 2.11**. Since they are usually larger and taller than the diffractive elements, their diffraction patterns are brighter than those from diffractive elements and can be easily identified and removed during post-processing. The camera sensor is with an 8-bit depth; therefore, the intensity reading measured in the LAMBDA platform will span from 0 to 255.

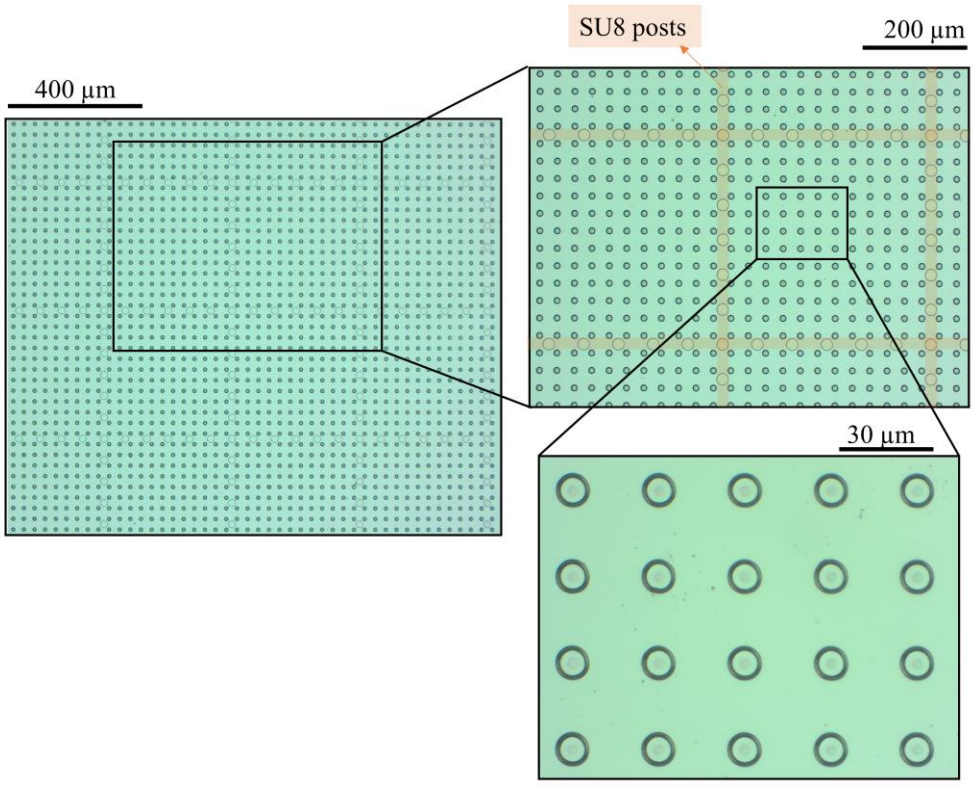

Figure 2.11 Microscope photos of the fabricated device. SU8 posts are highlighted in orange color in one inset.

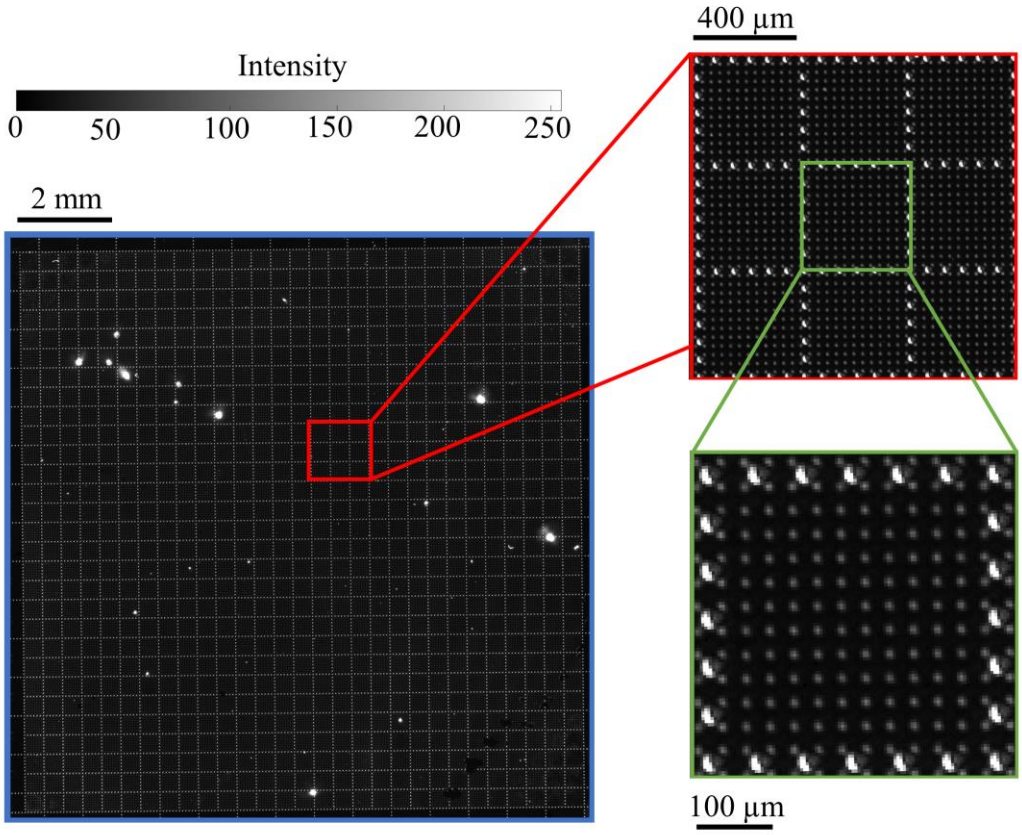

Figure 2.12 Measured diffraction patterns of the fabricated device in the LAMBDA platform.

2.4.2 Calibration Devices

To further study the relationship between the measured intensities/diffraction patterns and the displacements of diffractive elements, we fabricated a calibration device. The calibration device is composed of structures mimicking the diffractive elements but with pre-patterned displacements. In other words, for the device used in the LAMBDA platform ("real device"), the displacements of diffractive elements are created by the cellular traction force while for the "calibration device", the displacements are produced in advanced and fixed. The design, fabrication and characterization of the calibration devices will be explained as follows.

First, to generate various displacements on one device, the concept of Vernier pattern is utilized. As demonstrated in **Figure 2.13**, Vernier patterns are composed of two periodic configurations with minor difference in their periodicities. Hence, when the two patterns overlap, the perfectly aligned location is always accompanied with its neighbours offset slightly. Moreover, the offsets of the two patterns will increase gradually as the location is farther away from the perfectly aligned spot.

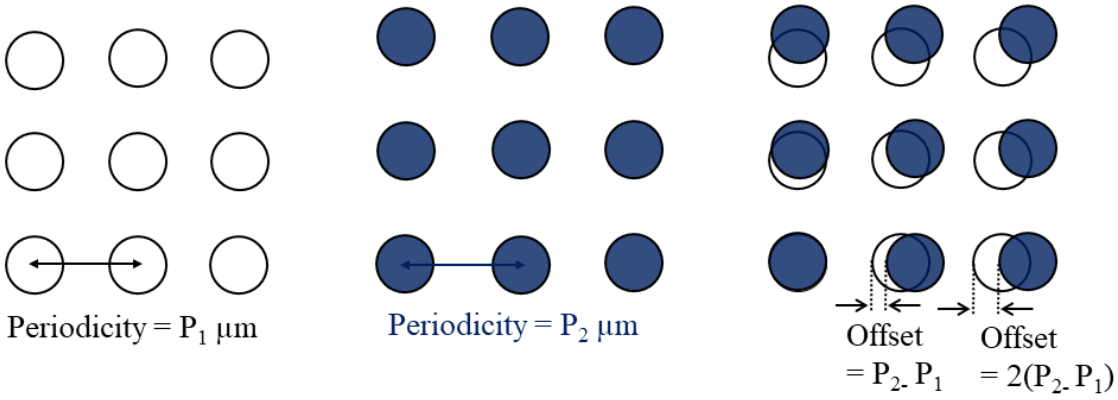

Figure 2.13 Concept of Vernier pattern.

Based on the similar concept, the calibration device is constructed by two complementary metal patterns with their periodicities offset by a small amount. To be more specific, the top metal pattern is circular disks array while the bottom metal pattern is circular holes array. The fabrication process of the calibration device is summarized in **Figure 2.14**. To begin with, we pattern the SU8 spacer on a glass substrate (**Figure 2.14 (a)**). They serve as spacers and control the PDMS thickness in the PDSM pressing step later. The pattern of SU8 spacers is the same as those used in the real device. Then, the circular holes array (bottom metal layer) is made by standard photolithography and metal lift-off (**Figure 2.14 (b-1)**). Meanwhile, the circular disks array (top

metal layer) is patterned on another glass substrate using the same method (**Figure 2.14 (b-2)**). Finally, the uncured PDMS is pour onto the bottom metal substrate with the top metal substrate flipped to cover the bottom substrate. A constant pressure (23 kpa) is applied on it through a PDMS buffer during curing (Same parameter as the PDMS stamping used for real device). The final calibration device is obtained after the PDMS layer is cured (**Figure 2.14 (c)**). The microscope photos of the top disks array and bottom holes array before assembling are shown in **Figure 2.14 (d-1)** and **(d-2)**, respectively. The difference of periodicity is 0.2 µm.

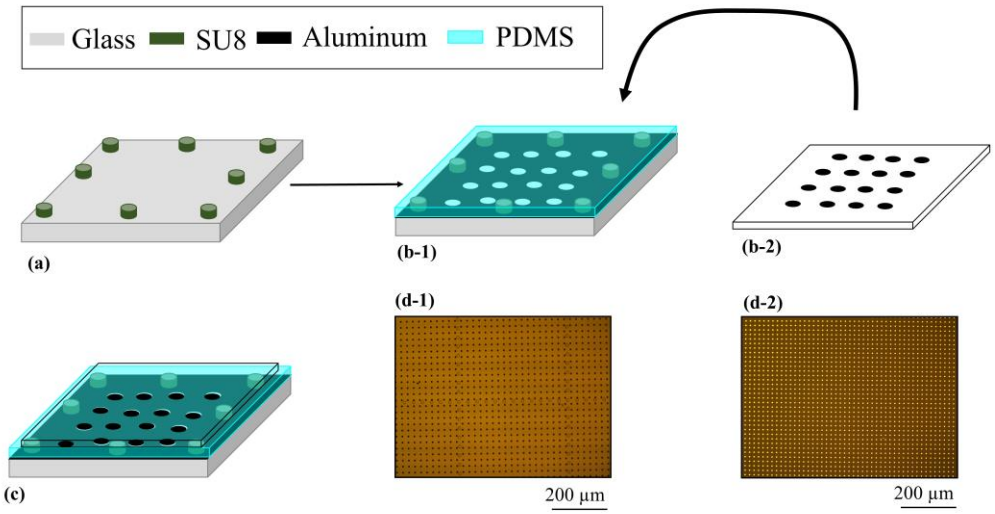

Figure 2.14 Fabrication process of calibration device.

The microscope photos and the measured diffraction patterns of the calibration device in the LAMBDA setup are shown in **Figure 2.15 (a) and (b)**, respectively. Array of 13x13 elements is shown with the centre 7x7 elements displayed in the zoomed-in image. As expected, the elements with larger displacement generate brighter diffraction patterns and the displacements increasing in a radiating way from the centre spot.

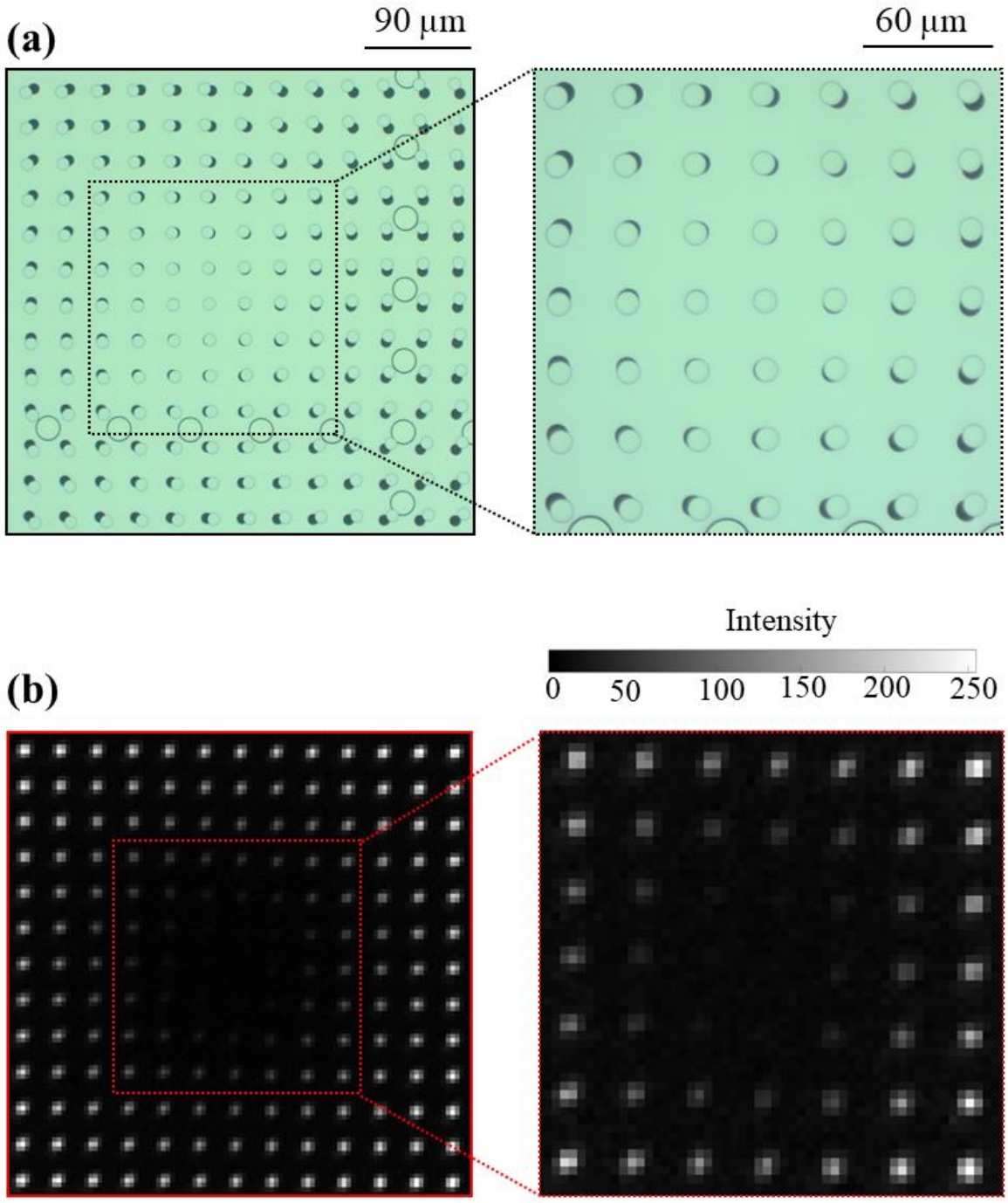

Figure 2.15 Calibration device (a) microscope photos (b) measured diffraction patterns.

Using high-magnification microscope images of the calibration device, we can measure the displacements directly and associate them with their intensity sum and diffraction pattern. The intensity sum is calculated by adding all pixels of the diffraction pattern from a single diffractive element. For the 13x13 elements shown in **Figure 2.15**, **Figure 2.16 (a)** displays the distributions of their intensity sum while **Figure 2.16 (b)** presents the corresponding displacements distribution. The values are also shown on the figures for quick visualization. For identification of each individual diffractive element, each column is assigned an alphabet (From A to M) and each row is assigned a number (From 1 to 13), as indicated on **Figure 2.16 (a)** and **(b)**. For example, element G7 has intensity sum equal to 48 and the displacement equal to 0. It is the element with the best alignment and the smallest displacement. The relationship of the displacements and the intensity sum is plotted in **Figure 2.16 (c)**.

In an ideal situation, without any traction force applied, the initial displacement of the diffractive elements for our real device should be close to zero; therefore, we first consider the case where the change in intensity sum and displacement are with respect to the element with the smallest displacement (i.e., element G7 of calibration device). **Figure 2.17 (a)** displays the change of intensities and the corresponding change of displacements using element G7 as the fiducial point. The curve seems to be piecewise linear composed of two slopes, with the boundary lies approximately at change in displacement equal to 2.5 μm.

Next, we move to the situation where there are non-zero initial displacements. **Figure 2.17 (b)** shows the cases where element F7, H9 and M13 are used as fiducial points. Case F7 (initial displacement = 0.57 μm) and case H9 (initial displacement = 1.81 μm) shows similar trends as case G7 (initial displacement = 0 μm) except that the boundaries that separate the two slopes become smaller and there is a vertical offset along y axis. On the other hand, for the very extreme

case M13 (initial displacement = 7.7 μm), the change seems to be saturated and slow down as the change of displacements increase.

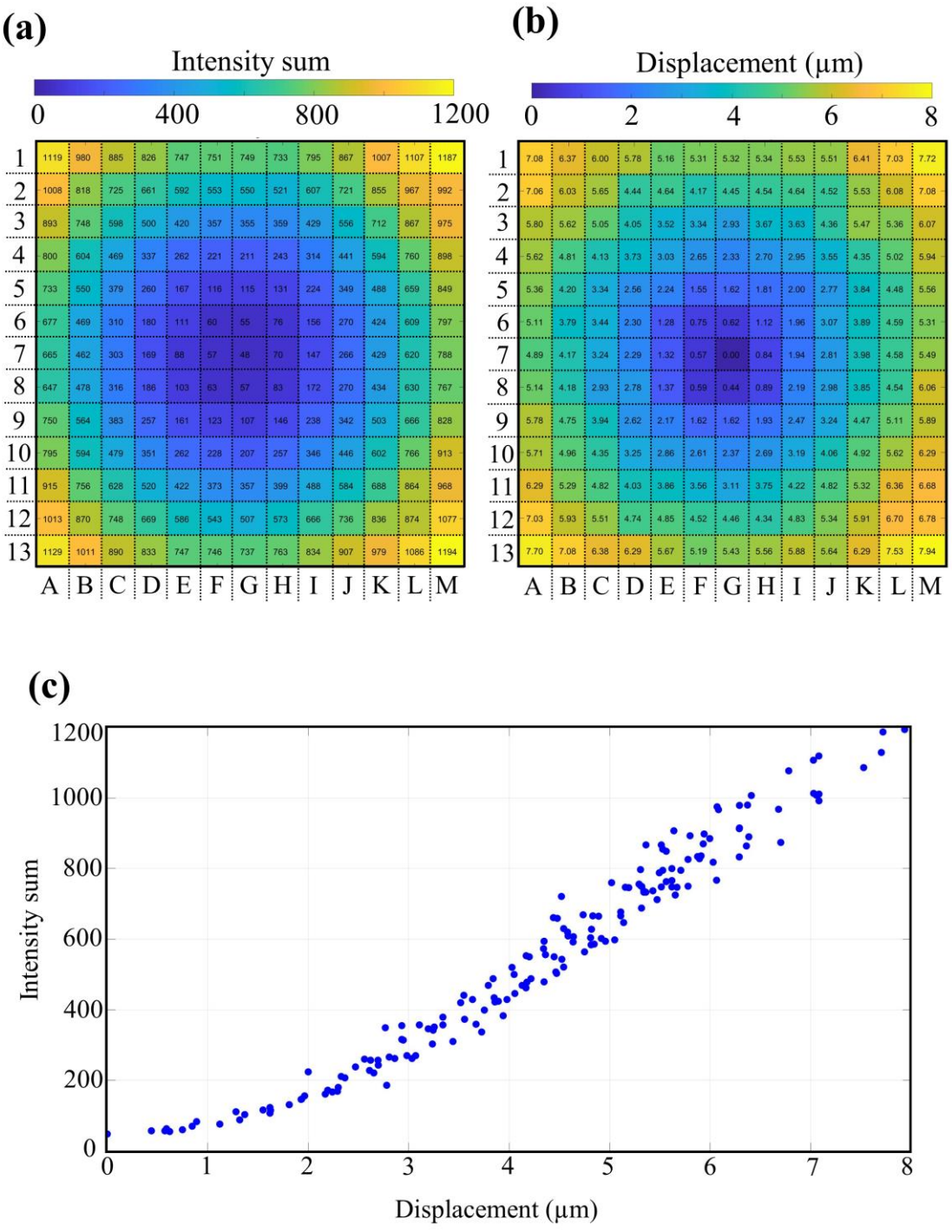

Figure 2.16 (a) Distribution of intensity sum, and (b) distribution of the displacements of the 13x13 elements shown in Figure 2.15 (c) relationship of the displacement and intensity sum of the calibration device.

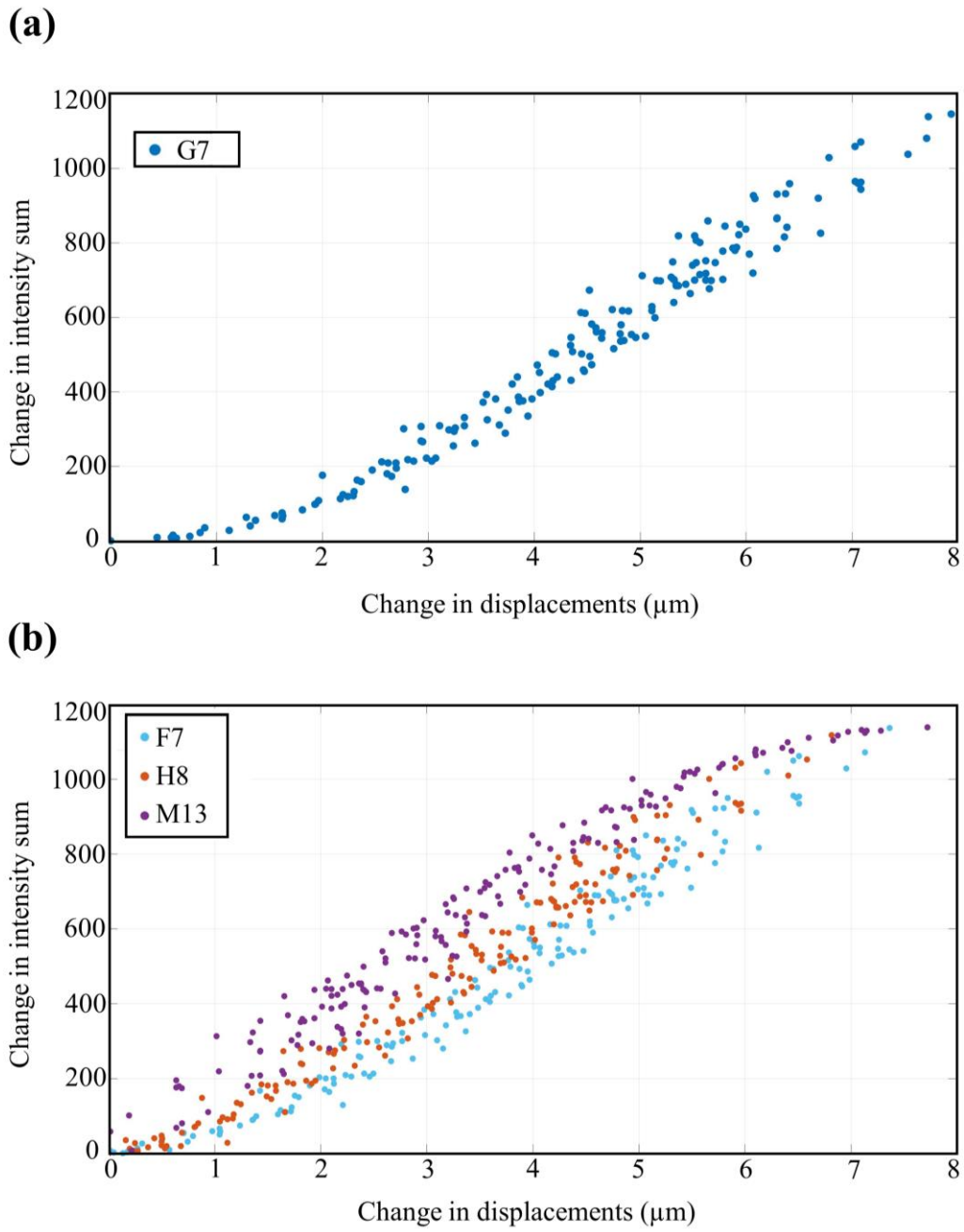

Figure 2.17 The relationship between change in displacement versus change in intensity sum based on diffractive elements with different initial displacements (a) element G7 (b) element F7, element H8 and element M13.

2.4.3 Discussions

From the measured diffraction patterns of calibration devices, we can conclude that the change of intensity sum is approximately proportional to the change of displacements. That is, the larger the change of intensity sum, the larger the change of displacements for a diffractive element. Since the displacements of a diffractive element in the cell experiments are induced by the cellular traction force, we can further infer that the change of intensity sum is also proportional to the cellular traction force. However, this qualitative statement assumes the fact that all diffractive elements are identical with zero initial displacements after fabrications. In practice, there exist variations between the initial displacements after fabrication, especially for a large-area device that spans over 1cm x 1cm dimension with almost ten thousand of diffractive elements. It should also be noted the intensity sum and its change with respect to the displacement is a function of the PDMS thickness. In addition, the absolute value of intensity sum is a function of illumination condition and exposure time of camera sensors. Therefore, to extract the cellular traction force quantitatively, more statistical analysis and complex calibration model are needed to account for all possible variations.

Although the current calibration device doesn't allow us to extract the cell-induced displacements from the measured diffraction pattern during experiments, it provides a qualitative proof for us to interpret the change of intensity sum obtained in the experiment. It can be considered as the ideal situation and serve as the foundation for a more complex model that can be further developed in the future. In short, what the LAMBDA platform measure is a direction indication of cellular traction force even though we are not able to quantitively extract the cellular traction force with high accuracy at this moment. Nonetheless, the transient biomechanics

dynamics profiled using LAMBDA platform is of great potential to be converted to traction force map in the future with a comprehensive calibration model.

Chapter 3 Real-Time Visualization of Large-Area Cellular Biomechanical Dynamics using the LAMBDA Platform

3.1 Introduction

To demonstrate the capabilities of the LAMBDA platform for visualizing the large-area cellular biomechanical dynamics in real-time, monolayer tissue sheet composed of a few hundreds of thousands of neonatal rat ventricular myocytes (NRVMs) are seeded on the devices. Various beating patterns are recorded. Observation field-of-view up to 10.6 mm by 10.6 mm is achieved. Meanwhile, high spatiotemporal resolution is maintained (with temporal resolution up to 130 frames per second and spatial resolution down to 20 μm). Hence, global beating behavior and local heterogeneity can be readily recognized at the same time. Moreover, several conditions such as spontaneous beating, electrical stimulation and chemical stimulation are included to illustrate our strengths for real-time monitoring of fast biomechanical dynamics. Additionally, the label-free nature of our platform allows long-term observation with minimized perturbation of the physiological environment. Recordings of biomechanical dynamics from the same cell cultures up to 7 days are reported. Finally, we integrate the LAMBDA platform with fluorescent microscope to conduct simultaneous mapping of the calcium concentration and biomechanical transient. The results verify the potential of combining the LAMBDA platform with conventional optical mapping to further study the coupling and interplay between biomechanical, biochemical, and bioelectrical properties.

3.2 Experimental setup

3.2.1 Stage Top Incubator

To keep the seeded cells in a native environment for long-term, continuous monitoring of their behaviors and minimize interference while they grow and mature. A homemade stage top incubator is integrated into the platform. The incubator provides a constant temperature environment and supplies the desired gas mixture optimized for cell growth. In our experiments, constant temperature at 37°C and humid gas mixture (95% air, 5% CO_2) is adopted if otherwise specified.

3.2.2 Illumination, Image sensor and Control Circuit

The intensity and homogeneity of illumination are critical for large-area measurements. Monochromatic LED chip (Chanzon, 3W, 450mA) is soldered on a heat sink and the diverging beam from the LED chip is collimated by a plano-convex lens (focal length = 75 - 100mm) to provide a uniform illumination. A 90° prism mirror is used to turn the illumination direction from horizontal to vertical. Deep red LED (wavelength = 660 nm) is selected for the experiments to minimize light scattering in the tissue if not otherwise specified.

To offset the image plane for easy configuration of devices and the image sensor, a 90° prism mirror is placed below the stage top incubator to project the transmitted diffraction patterns to the camera lens (0.727x magnification) and the image sensor (Emergent Vision Technologies, HB25000-SB-M). The data acquisition can be done automatically by incorporating switches and an Arduino circuit board as the control circuit.

3.2.3 Cell Seeding Procedure

Neonatal rat ventricular cardiomyocytes (NRVMs) are seeded with a density 0.2 - 0.25 millions/cm^2 to form a confluent monolayer tissue sheet over a 4cm^2 device area (active area ~

1cm^2). To allow the observation of cells via phase contrast microscope, a small transparent window is usually made at the edge of device. Typically, the cells will start beating 24 to 48 hours after seeding. 5% Fetal Bovine Serum (FBS) in Dulbecco's Modified Eagle Medium (DMEM) is used as the culture medium for NRVMs. Fresh medium is changed every other day.

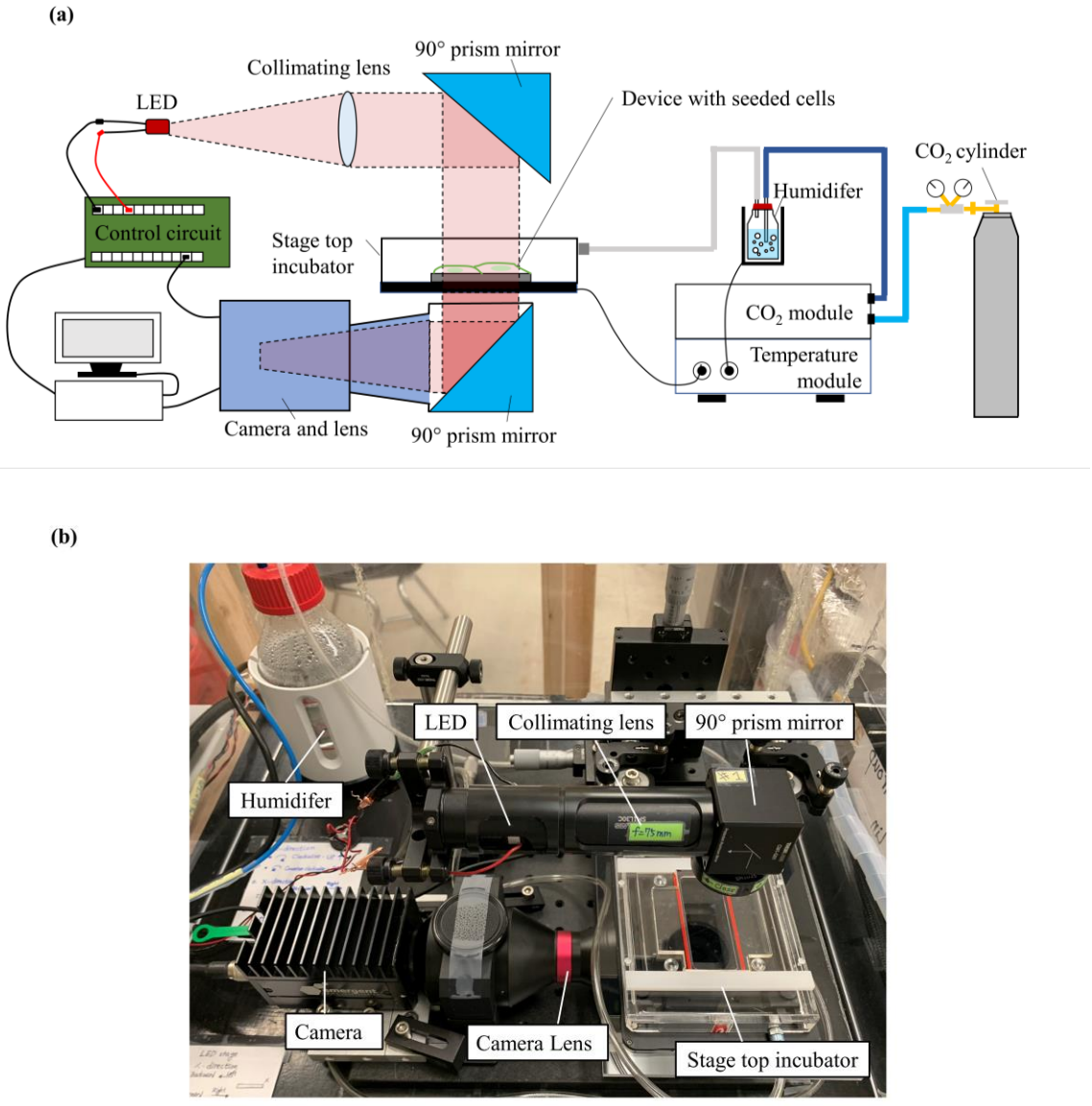

Figure 3.1 (a) Schematics and (b) photo of the stage top incubator and the LAMBDA platform.

3.3 Methods

3.3.1 Representative Pixels of Diffractive Elements

As illustrated in **Section 2.4**, each diffractive element will generate a diffraction pattern depending on the applied cellular traction force and will change over time according to the beating behaviors of cells. To clearly visualize the biomechanical dynamics, we define the representative pixel of a diffractive element to be the pixel that undergoes the maximum intensity change over time. **Figure 3.2 (a)** presents an example of 3x3 diffraction patterns with their representative pixels marked by blue circles while **Figure 3.2 (b)** shows an example of the time-course intensity of a representative pixel at certain location. Since the pixel intensity is a function of both time and spatial location, we denote it as I(t; x, y) for easy explanation hereafter.

To distinguish the signals generated by cellular activities from the fluctuated noise, the diffractive element is considered to be "activated" only when its representative pixel has intensity change larger than a certain threshold ($\Delta I > I_{thres}$). The intensity threshold is adjusted according to the noise levels from different measurement conditions. The noise level is often related to the stability of illuminating light, exposure time and electronic noise of the image sensor. For an activated diffractive element, the intensity of its representative pixel is normalized to lie between zero and one (**Figure 3.2 (c)**) to extract the "activation time (AT)" and "activation duration (AD).

First, the activation time is a figure-of-merit to characterize the timing when the beating wave arrives at a certain position. In conventional optical mapping, it is often defined as the point with the steepest change of fluorescent intensity and can be obtained by finding the maximum value of the first derivative (dI/dt_{max}) Here, to enhance the accuracy from our discrete data points, the rising part of the normalized intensity is fitted by a logistic curve and the midpoint of the logistic function (t_0) is considered as the activation time (**Figure 3.2(d)**). Next, the activation

duration is how long the beating lasts at a certain location. Mimicking the common definition of activation potential duration (APD), we define the activation duration to be the interval between the time where the intensities are half of its maximum value (Normalized intensity = 0.5). It is denoted as AD50 in **Figure 3.2 (c)**.

Finally, in addition to the time-course intensity, activation time and activation duration, beating frequency is another critical characteristic. It can be obtained by calculating the frequency spectrum of the time-course intensity by fast Fourier transform (FFT).

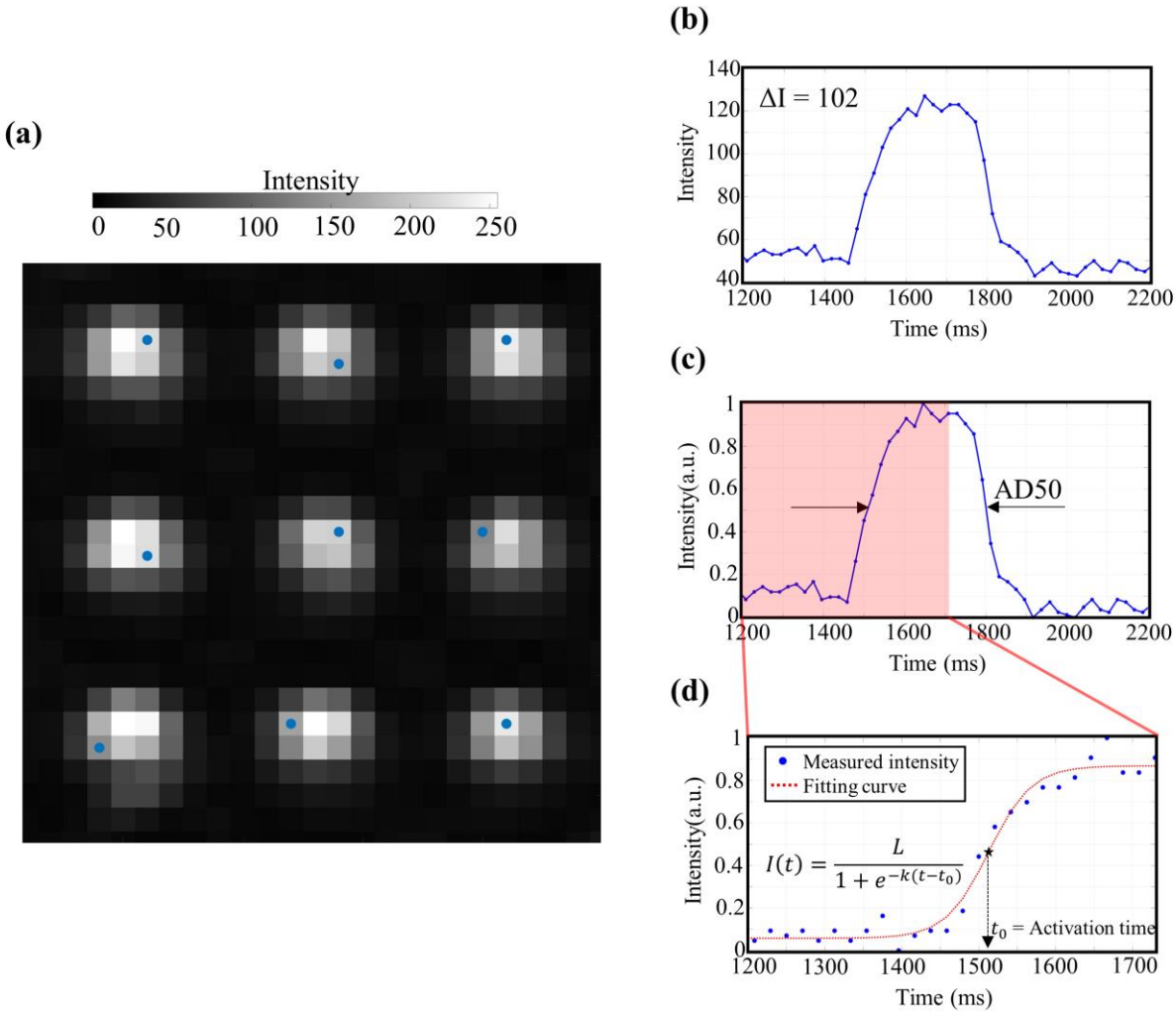

Figure 3.2 (a) Diffraction patterns with representative pixels marked by blue circles (b) time-course intensity of a representative pixel (c) normalization of time-course intensity (d) definition of activation time.

3.3.2 Intensity Sum and Diffraction Pattern

The representative pixels discussed in **Section 3.3.1** allow us to quickly retrieve some crucial properties of biomechanical dynamics including beating pattern, beating frequency and activation time. On the other hand, the diffraction pattern, along with the intensity sum of all the pixels in a diffraction pattern, contains rich information for extracting cellular traction force

quantitively. Although the compressive calibration model has not been established, it is worth discussing the idea here for future reference. For example, **Figure 3.3 (a) to (f)** demonstrates the change of diffraction patterns from a diffractive element during a beating. The summation of all the pixel intensities from a single diffractive element (5x5 pixels here) is displayed in **Figure 3.4 (a)**. Meanwhile, each pixel is plotted in **Figure 3.4 (b)** and the naming of their locations are highlighted in **Figure 3.4 (c)**. It should be noted that to better visualize the time-course change of individual pixel, there are three different intensity spans (y axis) in **Figure 3.4 (b).** They are marked with different outline colors for clear identification (Black: intensity span = 20; Green: intensity span = 30; Red: intensity span = 50). The maximum intensity change of each pixel (ΔI) is also displayed on the figure. The time span (x axis) for all the figures in **Figure 3.4 (b)** is identical.

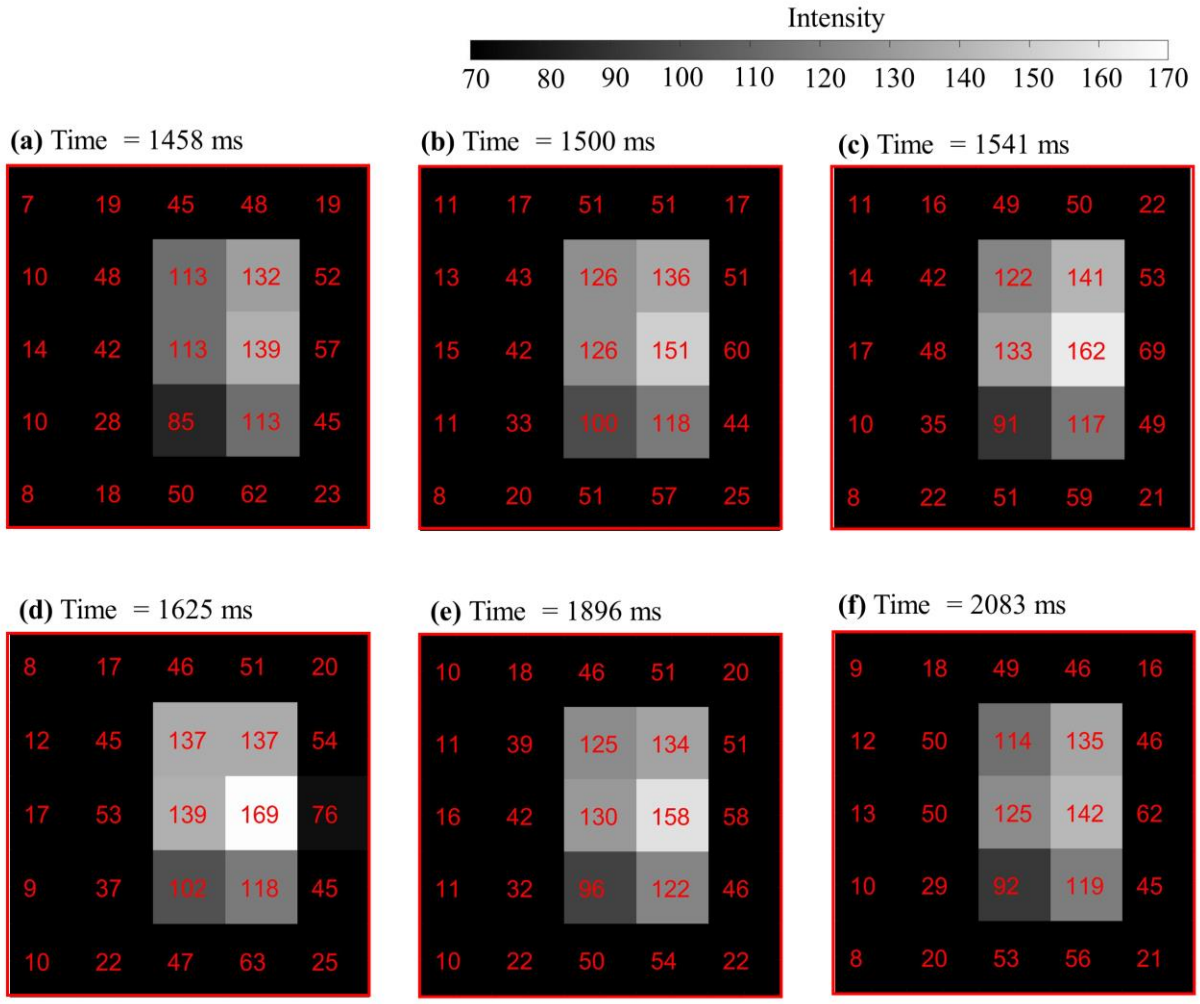

Figure 3.3 Change of diffraction patterns over time during a beating.

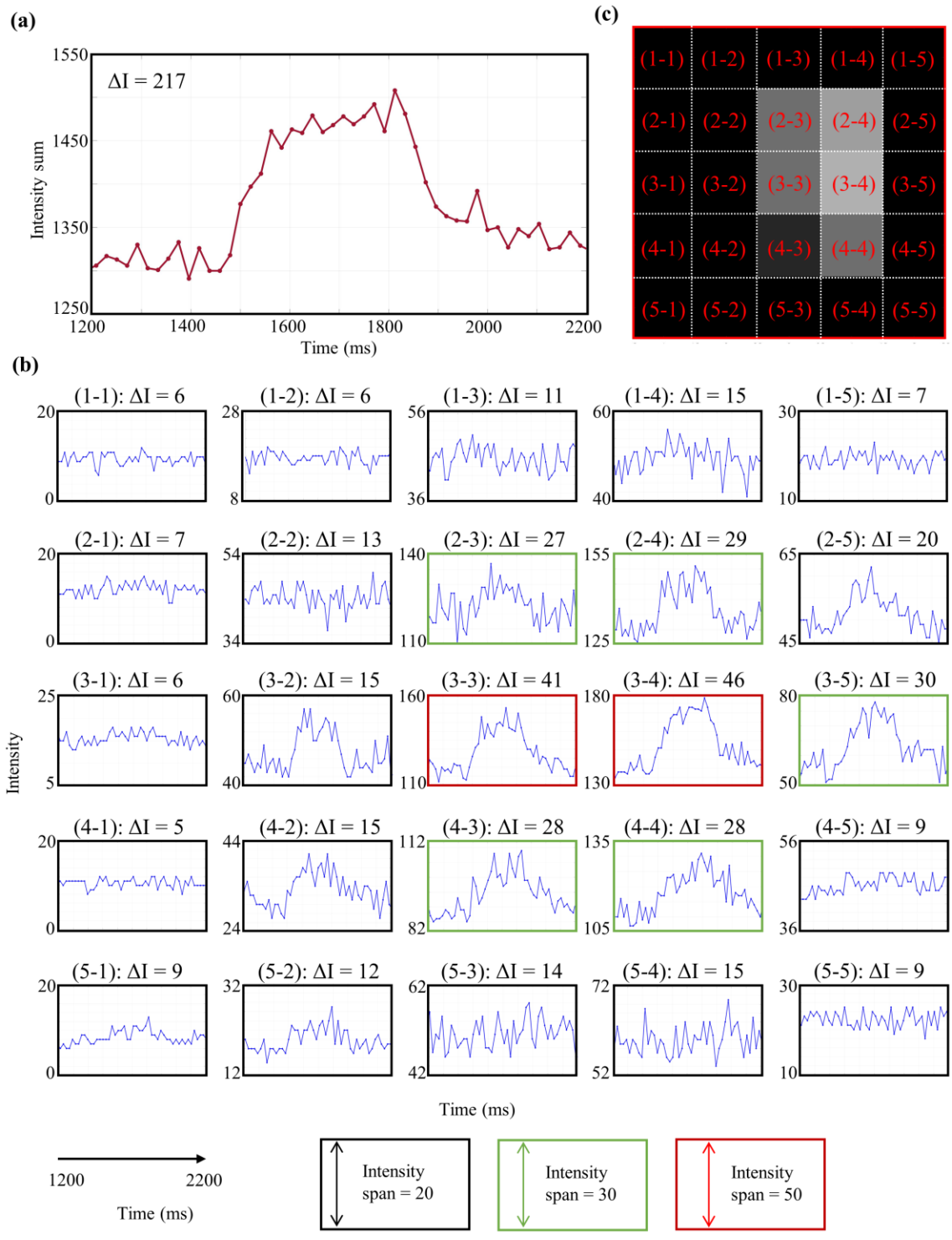

Figure 3.4 (a) Time-course intensity sum (b) time-course intensities of each pixel from a diffraction pattern (c) naming for the location of each pixel.

3.4 Experimental Results

To demonstrate the strengths of the LAMBDA platform, in the following, different scenarios of cell experiments are presented in each subsection. To be more specific, spontaneous beating, electrical stimulation, chemical stimulation, and long-term observations of biomechanical dynamics up to 7 days are included. Additionally, we integrated fluorescent imaging with the LAMBDA platform. Simultaneous measurements of calcium concentrations and biomechanical dynamics are conducted.

3.4.1 Spontaneous Beatings and Beat-to-Beat Variations

Figure 3.5 and **Figure 3.6** show the time-course intensity changes over the entire field-of-view (10.6 mm x 10.6mm) of two consecutive beatings from a NRVM monolayer. These two beatings feature completely distinct spatial patterns with a 7.8-second time difference in between. The 14-second recording captures three beatings, with the first one having a different pattern from the other two. For the first beating, it is initiated roughly from the center and propagate along both the right and left arc to the bottom left end (**Figure 3.5 (b) to (p)**). On the other hand, for the second and third beating, their onset is from the left-hand side and the wave travels to the right-hand side (**Figure 3.6 (b) to (p)**). The difference between the beating patterns can also be clearly seen from the activation time maps presented in **Figure 3.7 (a)** and **(b)**.

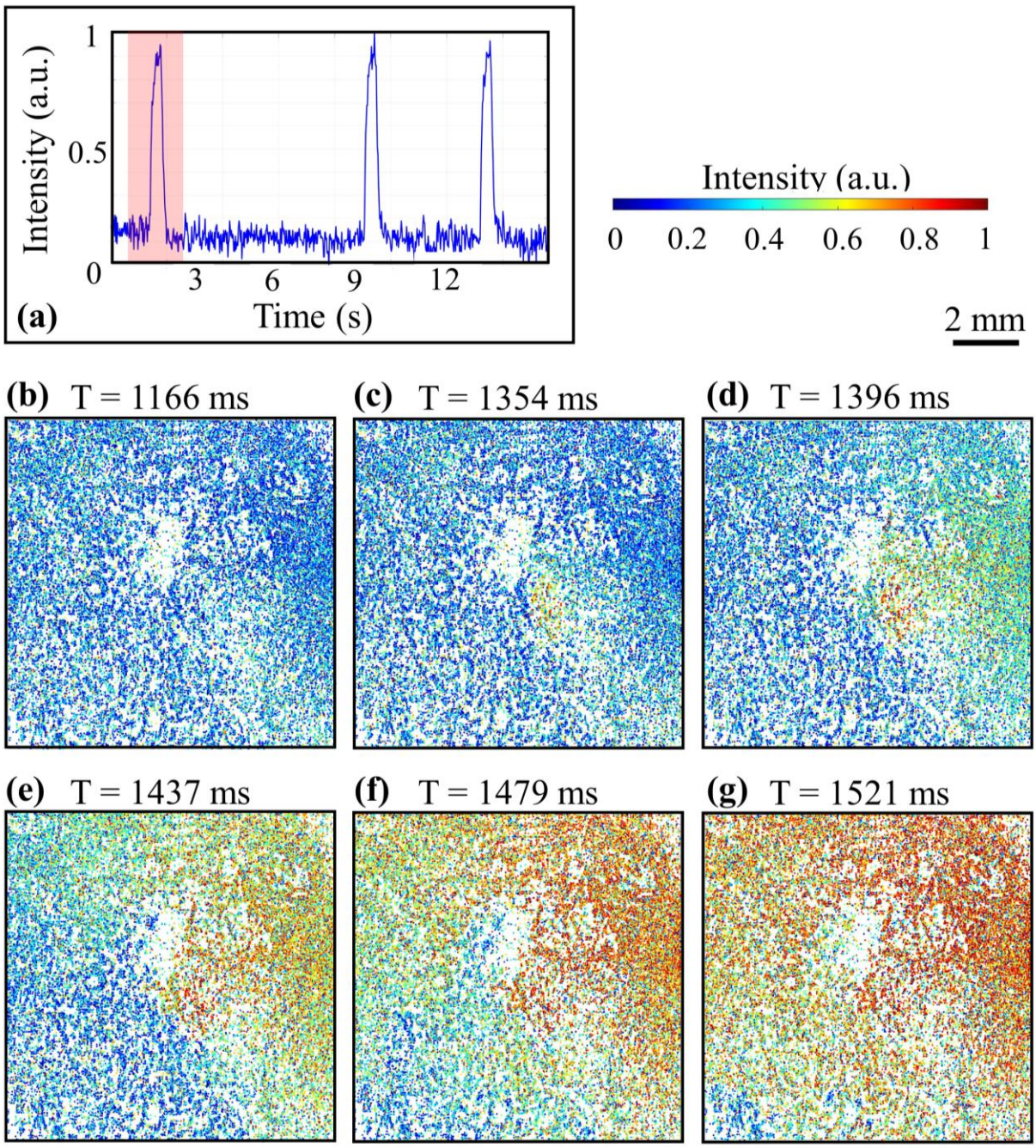
Intensity (a.u.)
1
0.5
0
3
6
9
12
Time (s)
(a)
Intensity (a.u.)
0
0.2
0.4
0.6
0.8
1
2 mm
(b) T = 1166 ms
(c) T = 1354 ms
(d) T = 1396 ms
(e) T = 1437 ms
(f) T = 1479 ms
(g) T = 1521 ms

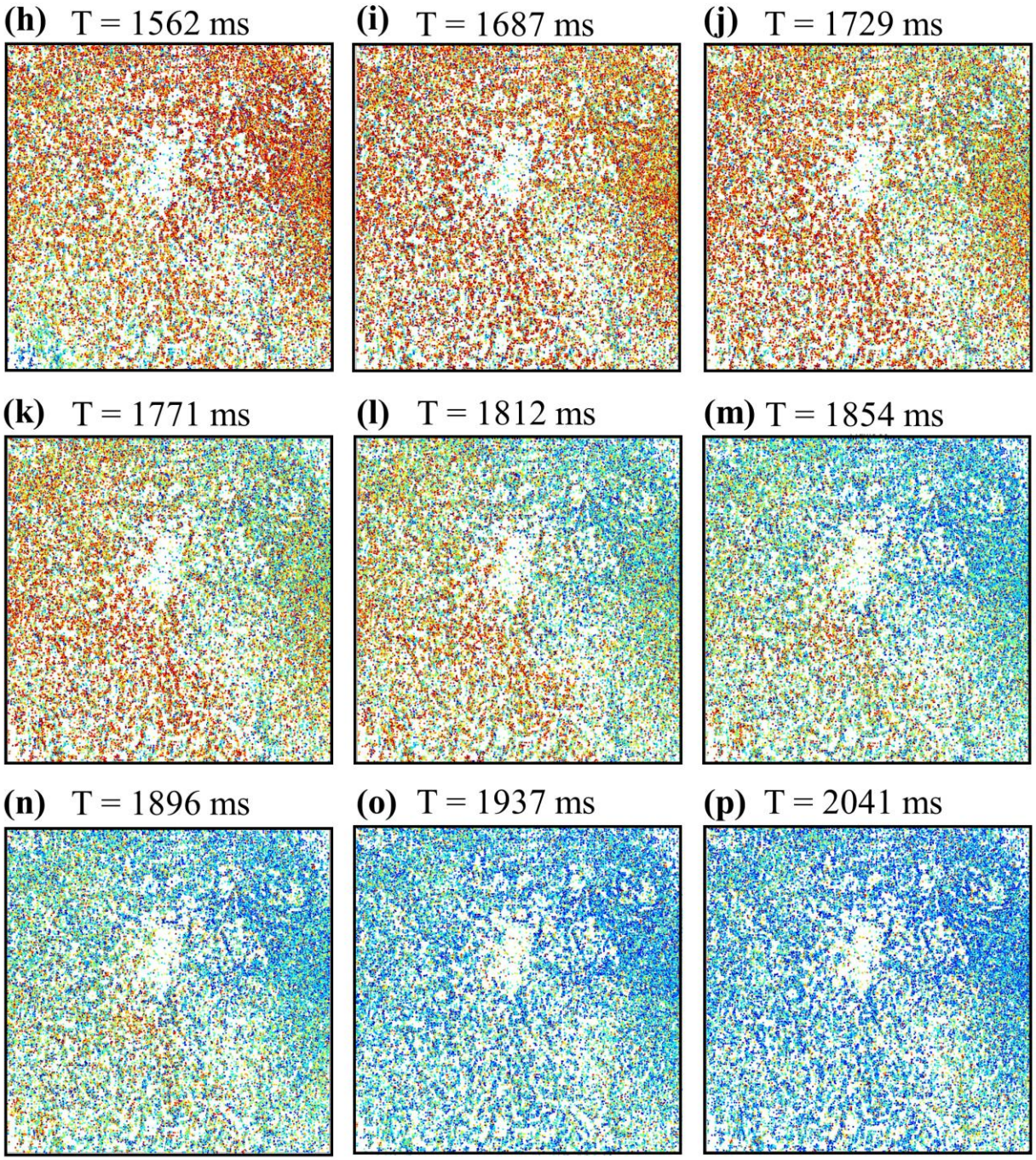

Figure 3.5 Time-course intensity change of the first beat during the recording.

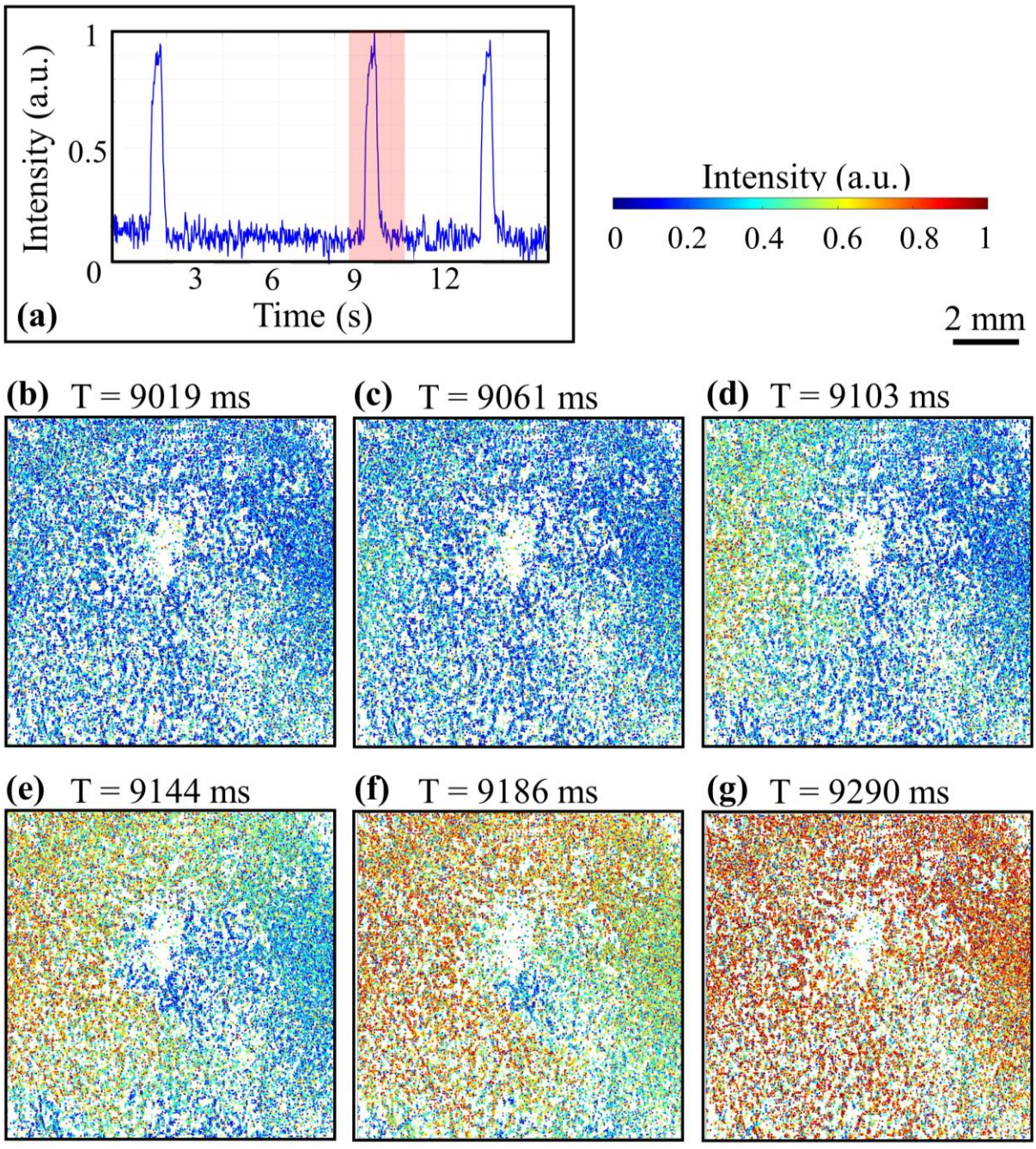
Intensity (a.u.)
1
0.5
0
3
6
9
12
Time (s)
(a)
Intensity (a.u.)
0
0.2
0.4
0.6
0.8
1
2 mm
(b) T = 9019 ms
(c) T = 9061 ms
(d) T = 9103 ms
(e) T = 9144 ms
(f) T = 9186 ms
(g) T = 9290 ms

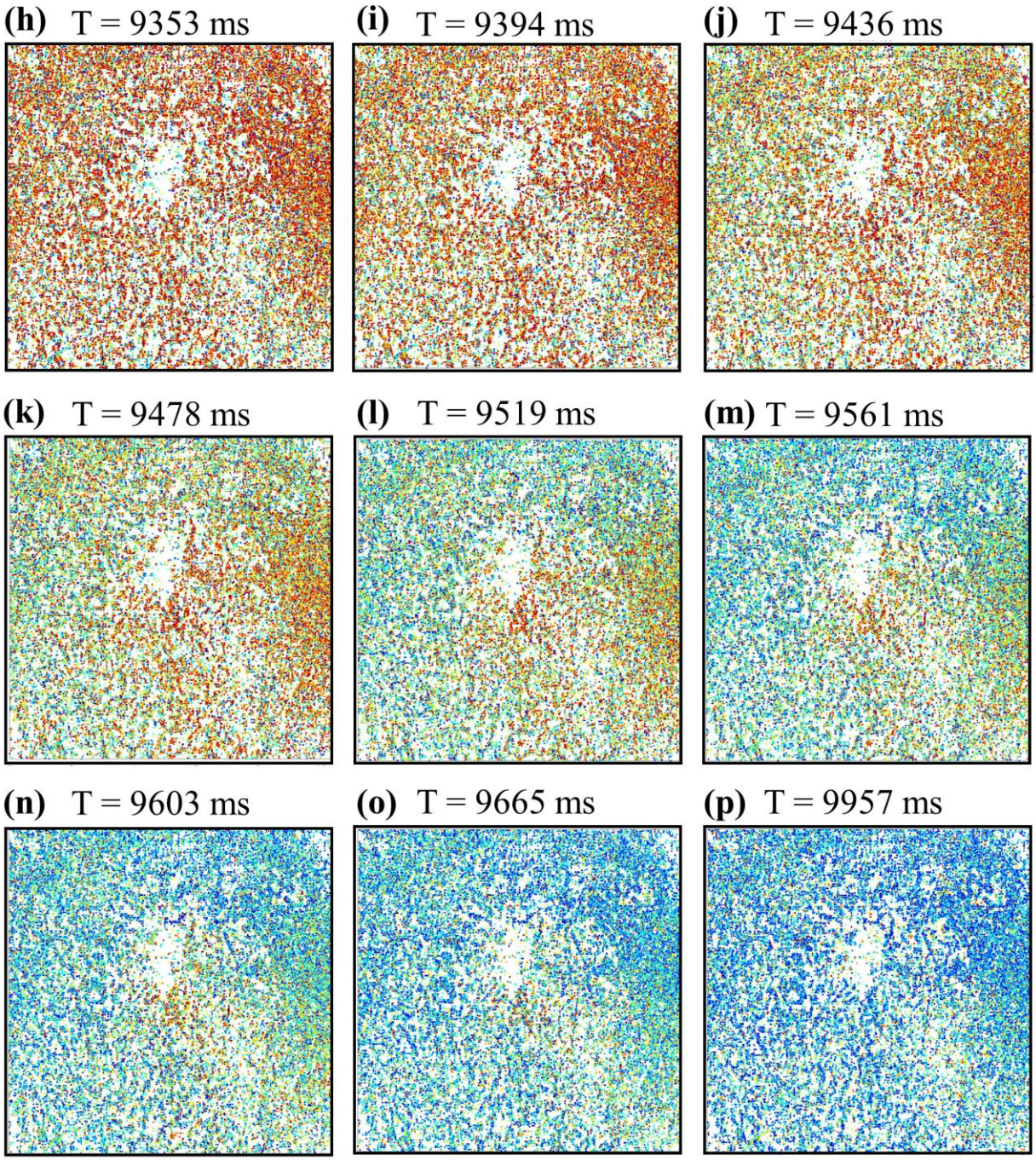

Figure 3.6 Time-course intensity change of the second beat during the recording.

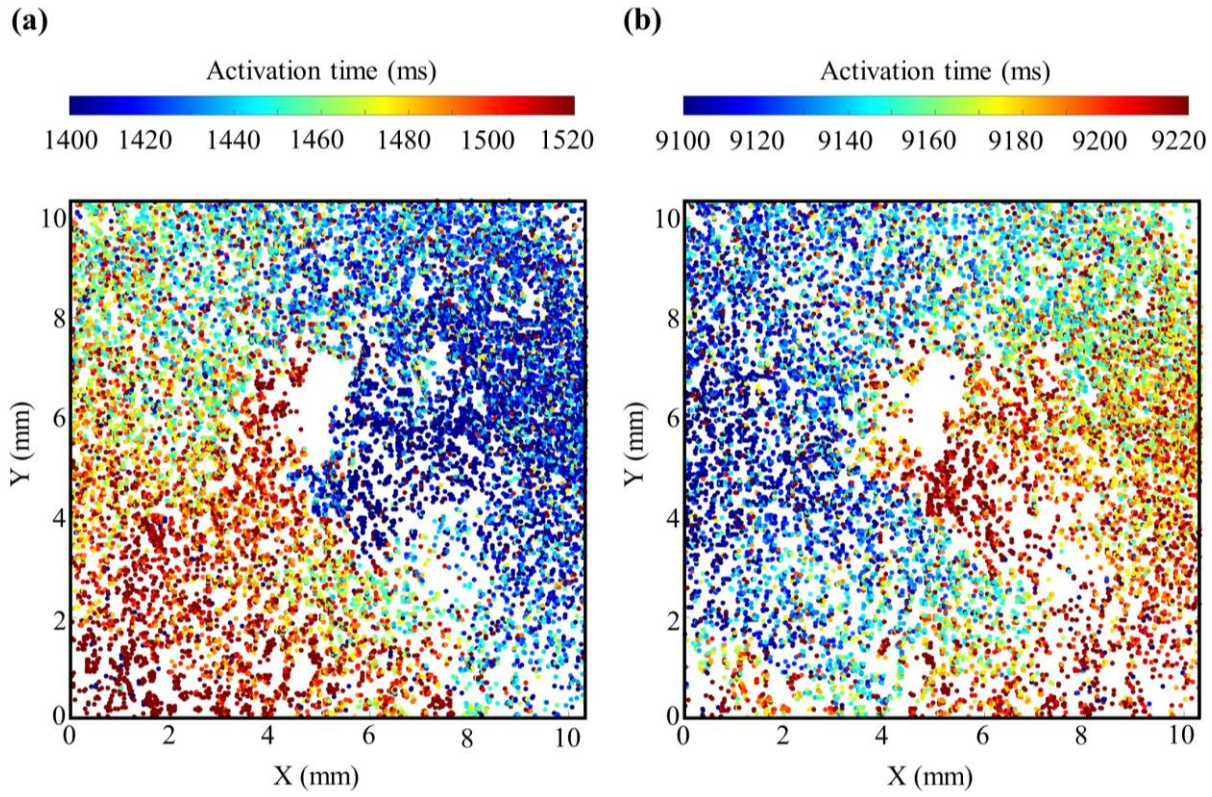

Figure 3.7 Activation time map of the (a) first beating (b) second beating.

To further illustrate the propagation of mechanical wave, four pixels at different locations are picked with their intensity change over time plotted in **Figure 3.8 (a) to (d)** for the first beating and in **Figure 3.9 (a) to (d)** for the second beating. The calculated activation time for each pixel is marked in the figure and labelled as "AT". The global conduction velocity (CV) can be approximately estimated if we divide the distance between the two pixels by the difference in their activation time. The distribution of these pixels and the conduction velocities are highlighted in **Figure 3.8 (e)** and **Figure 3.9 (e)**.

In addition to the global trend of beating pattern, we can observe a lot of heterogenous points that don't follow the main beating from the bulk, thanks for the high spatial resolution of

our platform. Some represented heterogeneous points are plotted in **Figure 3.10** (**(a) to (e)** for the first beating and **(f) to (j)** for the second beating). We can see that the contours of the intensity changes over time are very diverse. For instance, some of the traces display a peak while some of them have two peaks; however, none of them coordinated with the main beating exhibited by the majority. On the other hand, some of the traces experience very slow changes and do not show clear beating activities.

Furthermore, considering the entire span of recording (14 seconds), the intensity traces are very disparate including the number of beatings occurred, the trace shape and the signal to noise ratio. Some chosen examples are demonstrated in **Figure 3.11 (a)** to **(t)**.

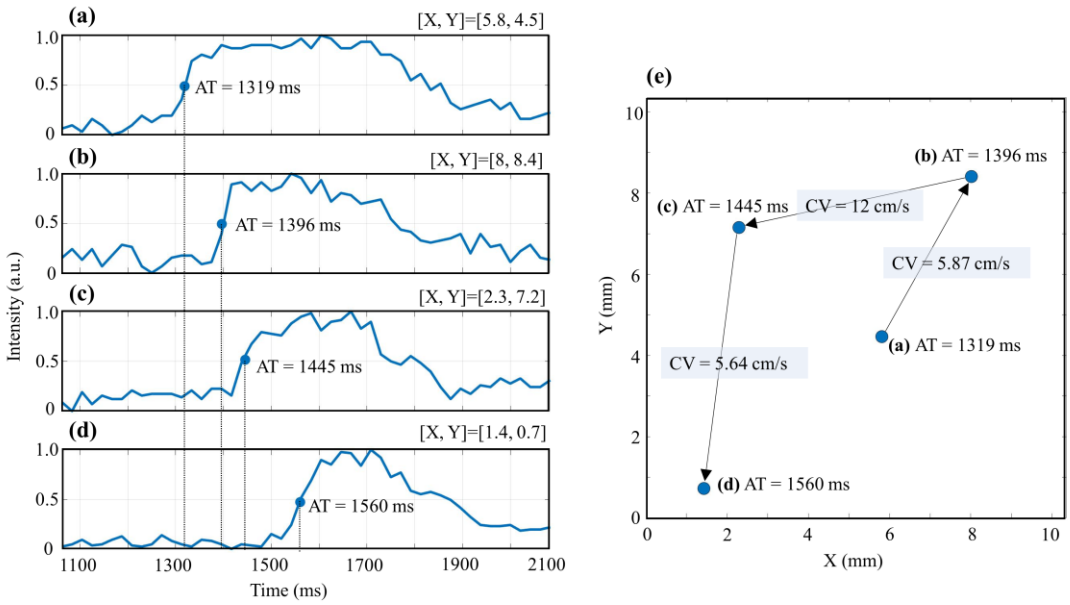

Figure 3.8 (a) to (d) Time-course intensities from some selected pixels for the first beating (e) distribution of the pixels and the calculated conduction velocity. (AT = activation time; CV = conduction velocity).

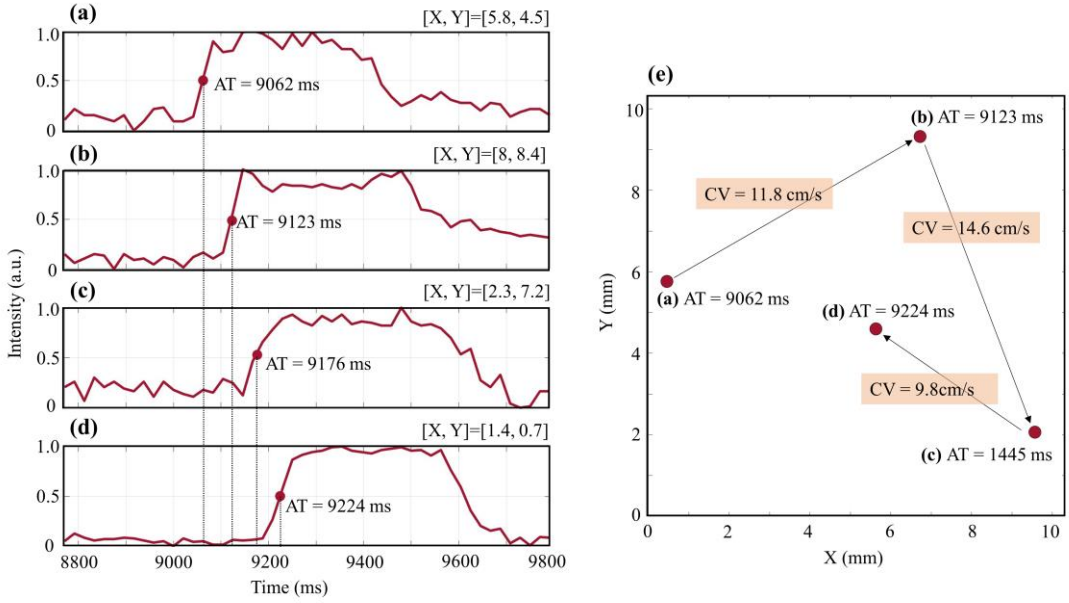

Figure 3.9 (a) to (d) Time-course intensities from some selected pixels for the second beating (e) distribution of the pixels and the calculated conduction velocity. (AT = activation time; CV = conduction velocity).

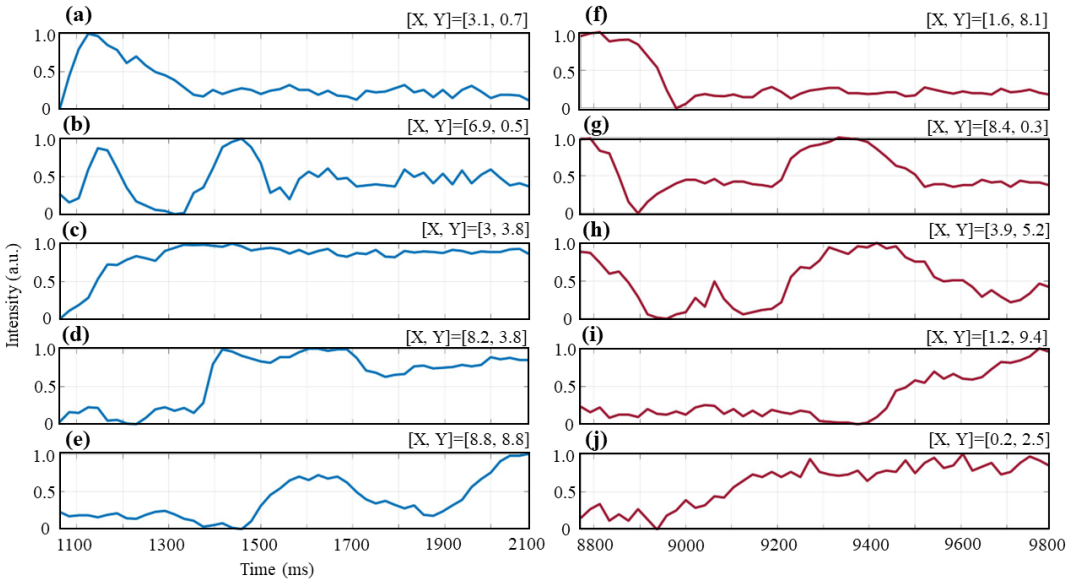

Figure 3.10 Time-course intensity from some selected heterogeneous points: (a) to (e) first beating; (f) to (j) Second beating.

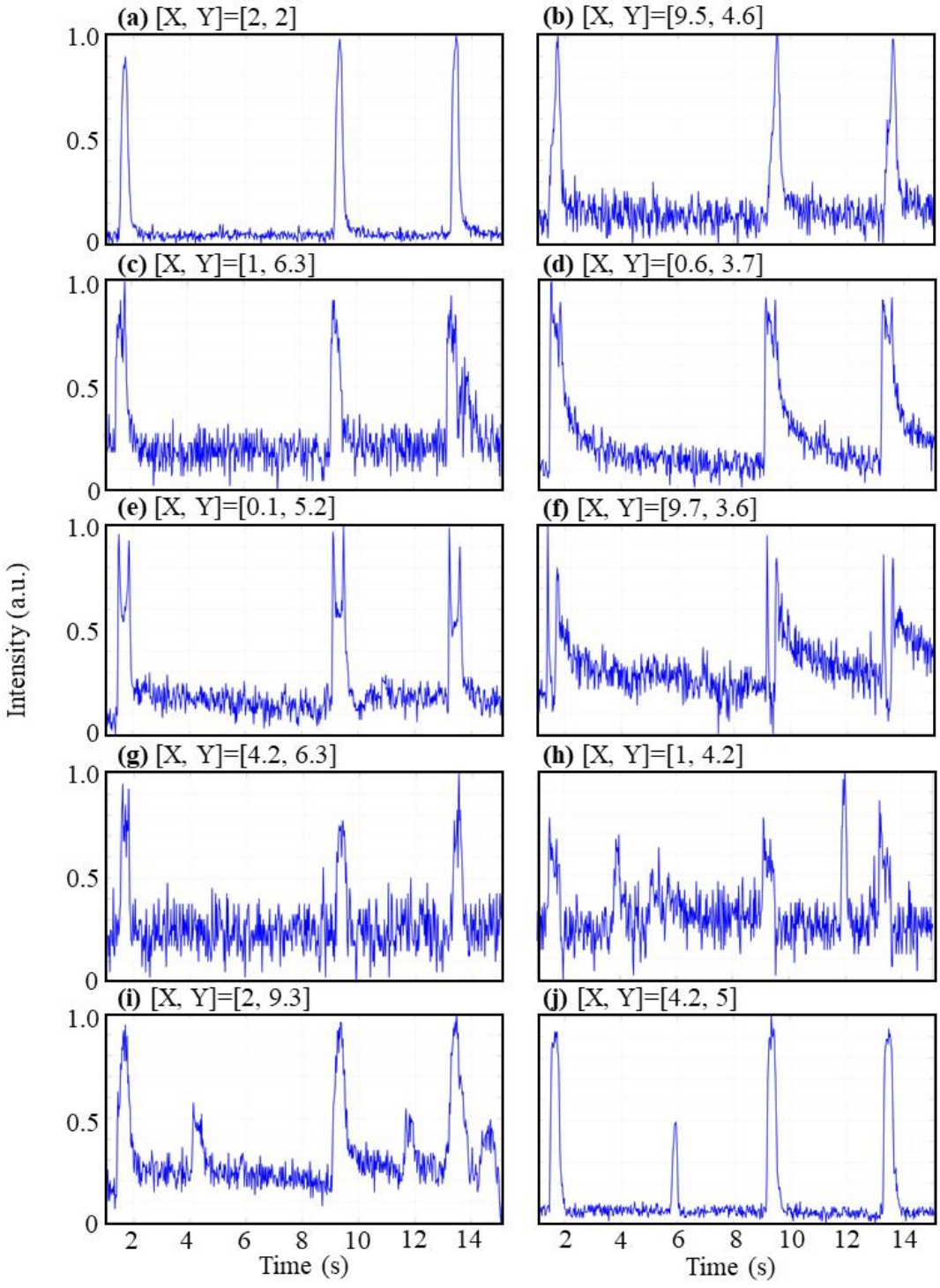
(a) [X, Y]=[2, 2]
(b) [X, Y]=[9.5, 4.6]
(c) [X, Y]=[1, 6.3]
(d) [X, Y]=[0.6, 3.7]
(e) [X, Y]=[0.1, 5.2]
(f) [X, Y]=[9.7, 3.6]
(g) [X, Y]=[4.2, 6.3]
(h) [X, Y]=[1, 4.2]
(i) [X, Y]=[2, 9.3]
(j) [X, Y]=[4.2, 5]
Intensity (a.u.)
1.0
0.5
0
2 4 6 8 10 12 14
Time (s)

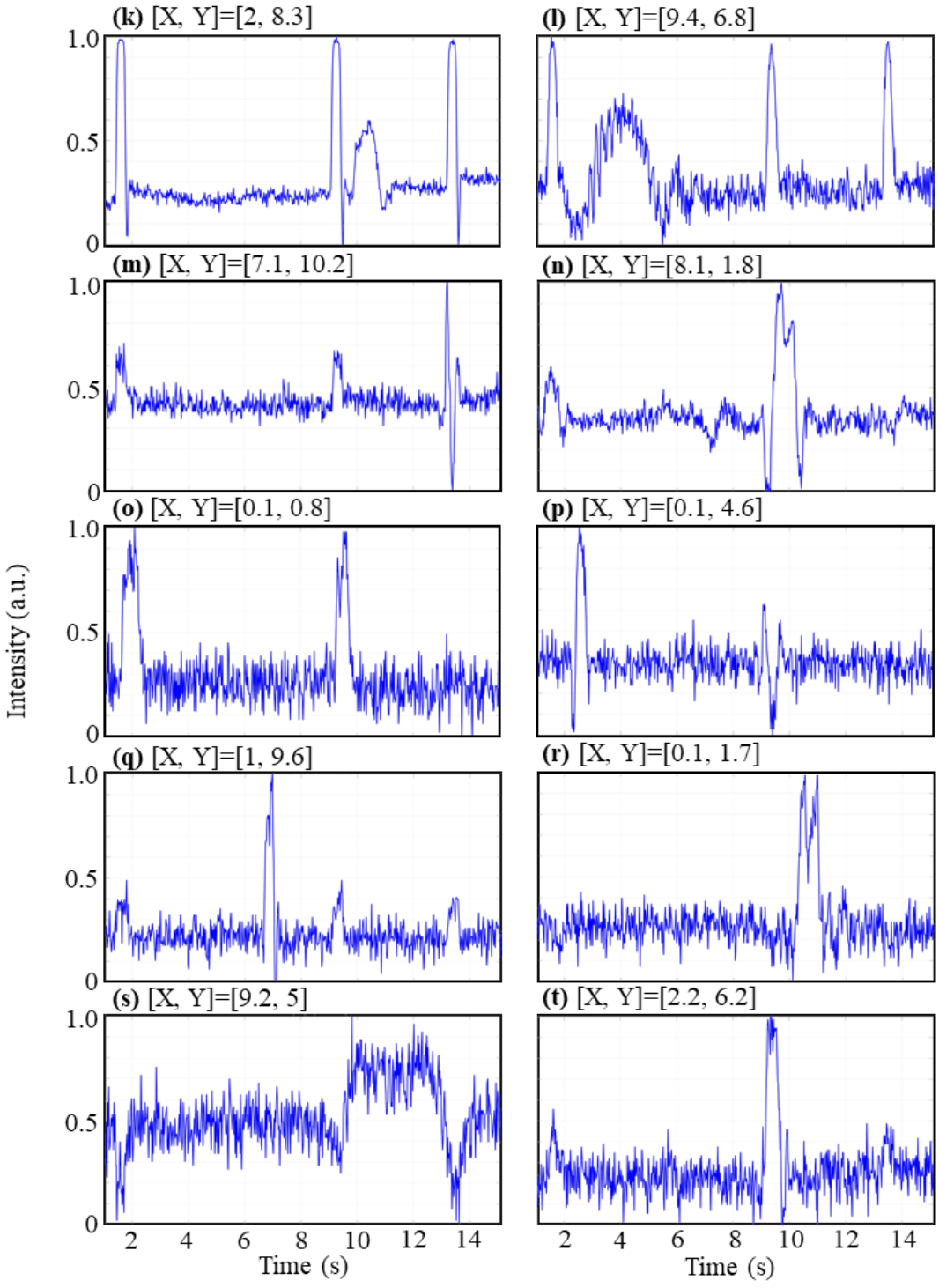

Figure 3.11 Time-course intensity from some selected pixels at different positions during the entire 14-second recording.

Next, the activation duration (AD) is another parameter worth some investigations. **Figure 3.12** and **Figure 3.13** present the activation duration for the first and second beating, respectively. Overall, for both cases, the activation durations follow normal distributions with the majority fall between 250 to 500 ms (**Figure 3.12 (a)** and **Figure 3.13 (a)**). Manifolds ranges of activation time are illustrated in **Figure 3.12 (b)** and **Figure 3.13 (b)**. Spatial distribution of activation duration is divided into three groups: 50 to 250ms, 250 to 500ms and 500 to 750ms. The three groups are plotted separately in **Figure 3.12 (c) to (e)** and **Figure 3.13 (c) to (e)**.

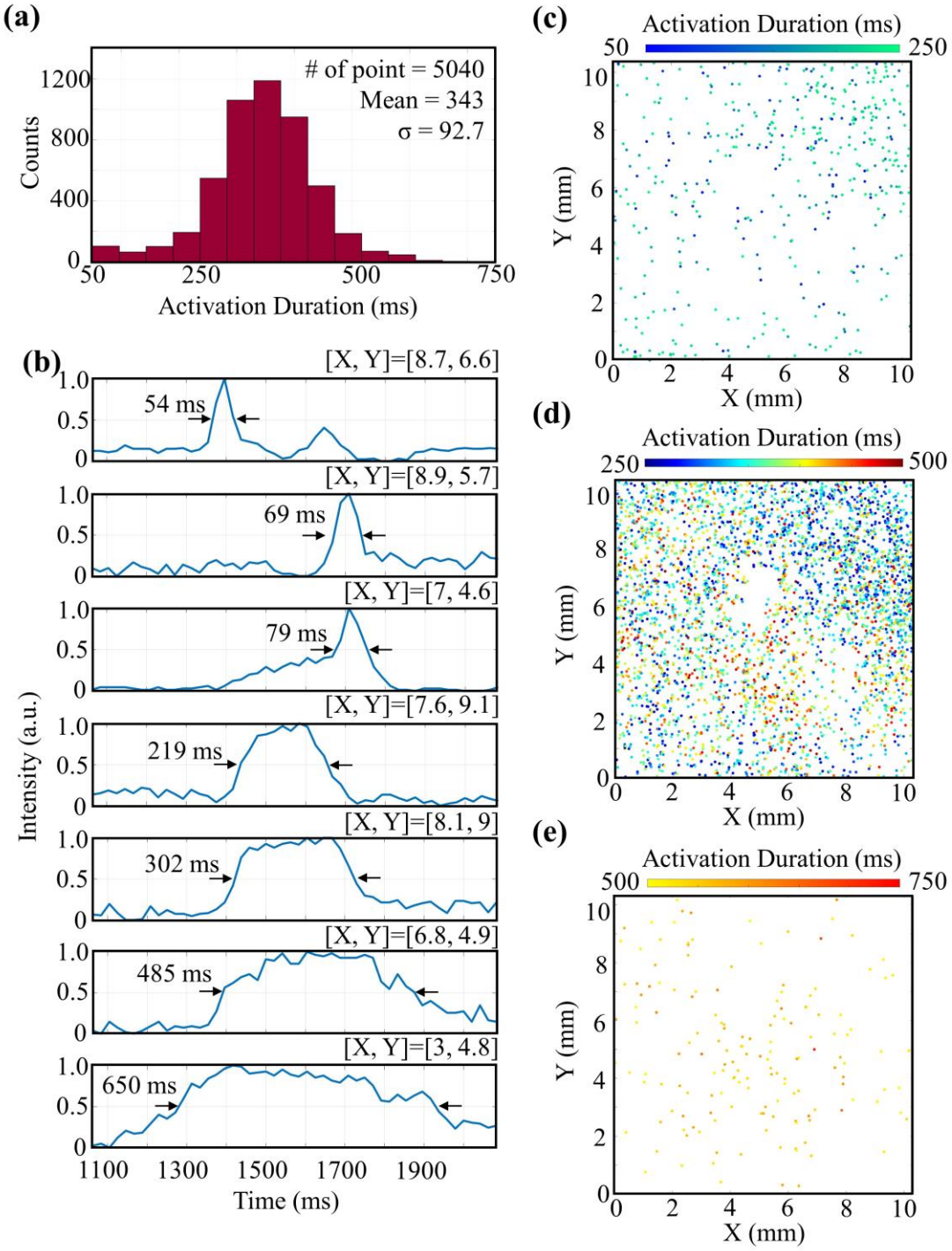

Figure 3.12 Activation duration of the first beating (a) histogram (b) selected time-course intensity to demonstrate various activation duration recorded (c) to (e) distribution of activation duration within certain range: (c) 50 to 250ms (d) 250 to 500 ms (e) 500 to 750 ms.

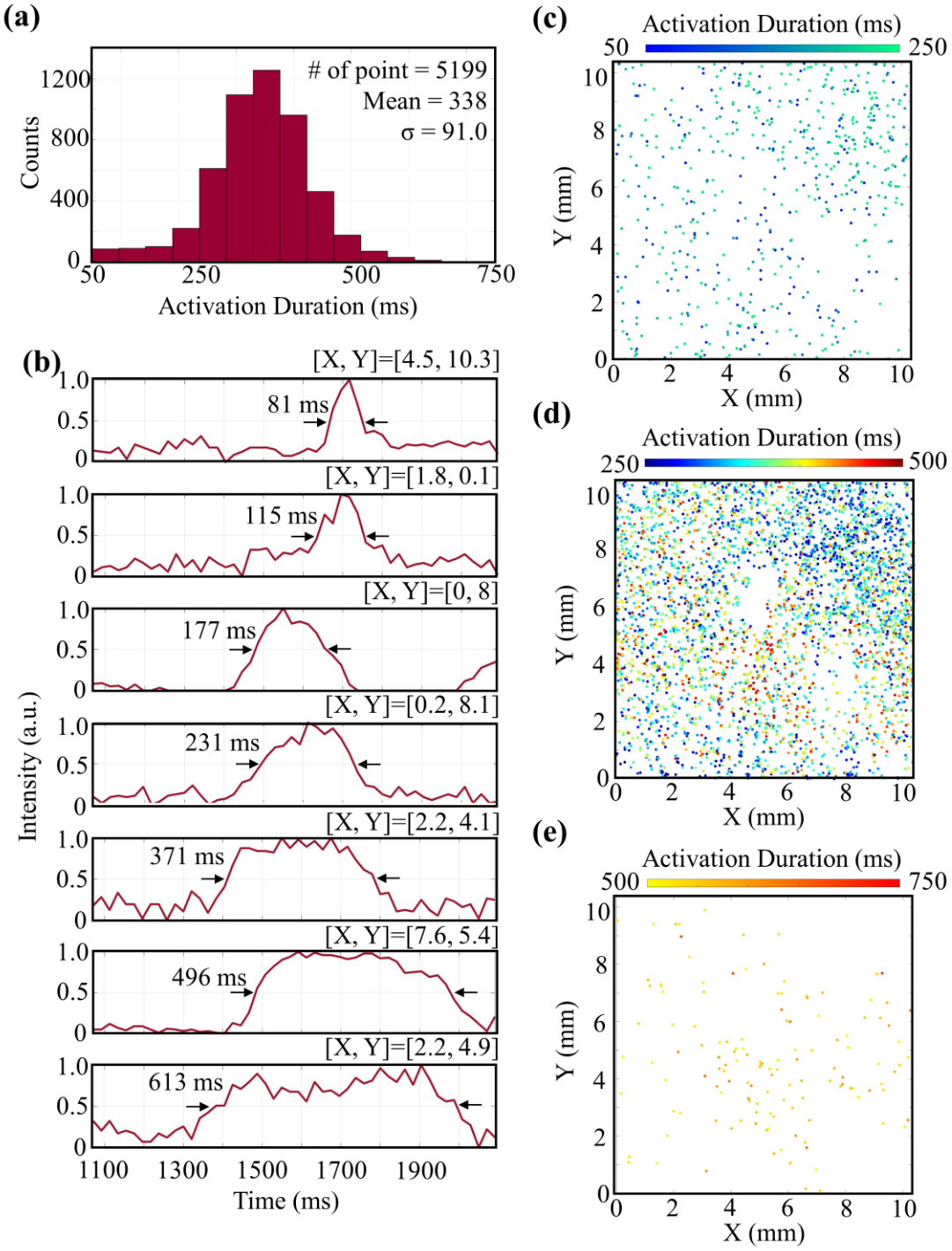

Figure 3.13 Activation duration of the second beating (a) histogram (b) selected time-course intensity to demonstrate various activation duration recorded (c) to (e) distribution of activation duration within certain range: (c) 50 to 250ms (d) 250 to 500 ms (e) 500 to 750 ms.

3.4.2 Electrical Stimulation

Dynamic spiral wave of cardiomyocytes is often associated with abnormal beating and cardiac arrhythmia. Our platform has captured this dynamic change with an unprecedent spatial resolutions compared to conventional optical mapping techniques that measure transmembrane potential or calcium concentration.

The time-course intensity distribution of a spiral wave exhibited by a monolayer of cardiomyocytes is shown in **Figure 3.14**. The spiral wave is initiated slightly to the left of the center and rotates counterclockwise. After this recording, to terminate the spiral wave arrhythmias, electrical stimulation is performed. A 1Hz, 50% duty cycle square wave with peak-to-peak voltage 200 mV is used to pace the sample for 1 min. Then, the recording is conducted 6 minutes and 18 minutes after stimulation. Their time-course intensity distributions are shown in **Figure 3.15** and **Figure 3.16**. Obviously, after the electrical stimulation, the spiral wave pattern disappears, and the waveform starts to propagate from right to left, corresponding to the fact that the stimulating electrode is at the right-hand side of the sample. Although the spiral pattern disappeared almost right after stimulation, it is interesting to note that the intensity plots expresses more heterogeneity as the wave propagates to the left end in **Figure 3.15** (6-minture after stimulation) but showing a more uniform intensity in **Figure 3.16** (18-minture after stimulation).

The activation time map presenting in **Figure 3.17 (a) to (c)** again highlight the pattern difference before and after electrical stimulation and the effect of cardioversion. The schematic of electrical stimulation and the relative location between the stimulating electrodes and sample is given in **Figure 3.17 (d)**. The electrodes are about 2mm away from the active area**.** The results strongly demonstrate our system's capabilities to track large-area biomechanical dynamics in real

time with high spatiotemporal resolutions that cannot be achieved by any of the existing technologies.

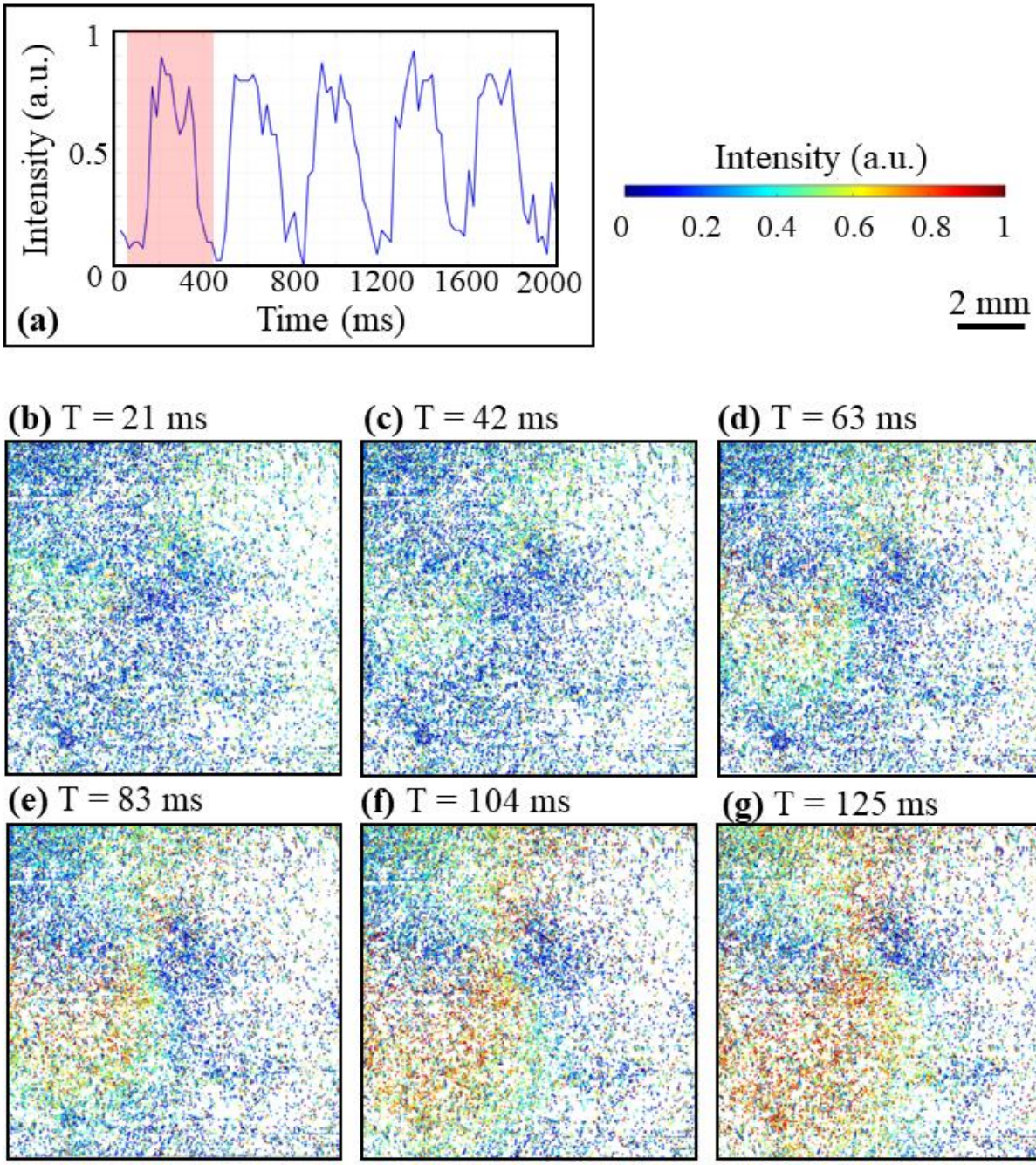

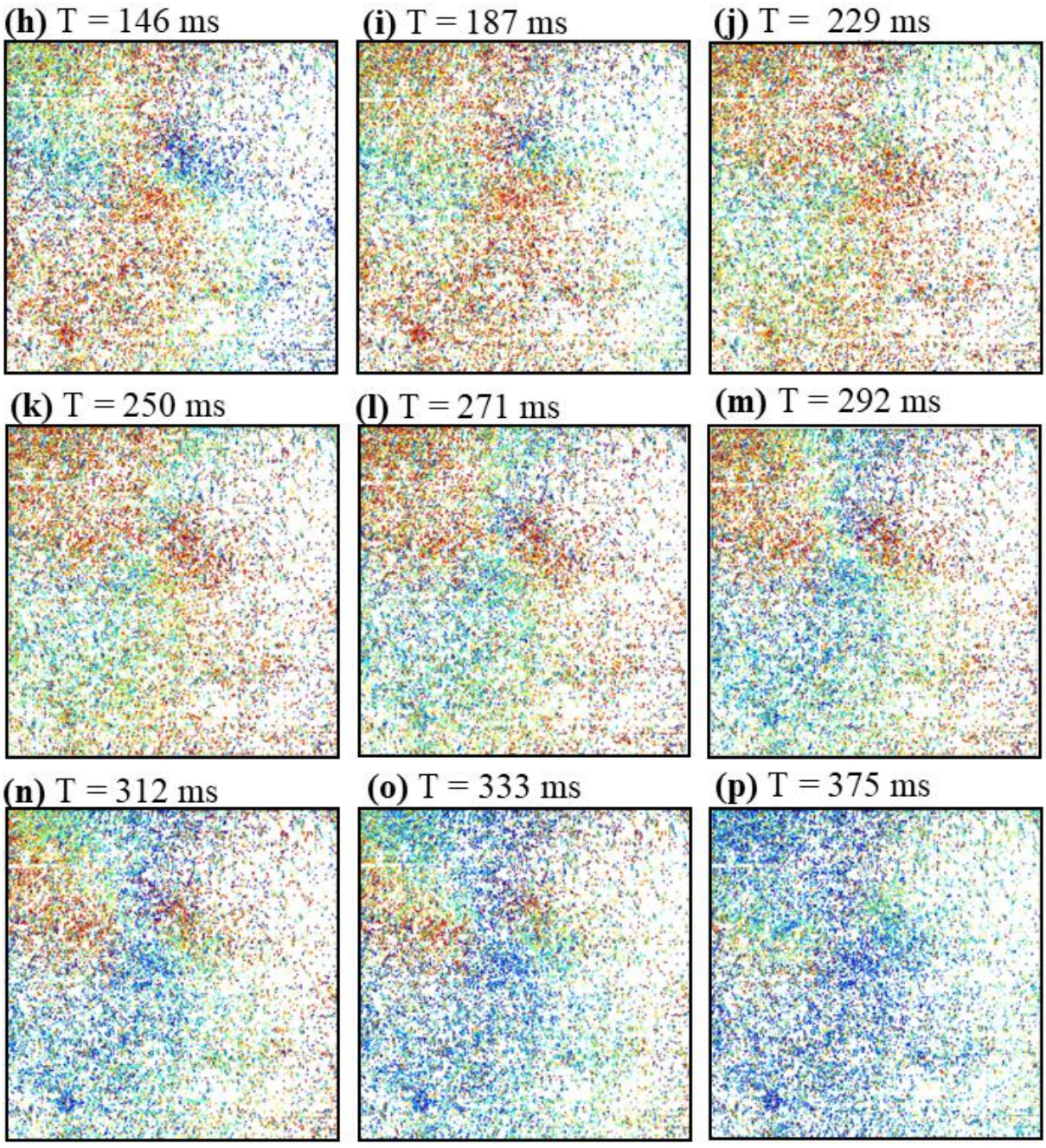

Figure 3.14 Time-course intensity change of the spiral wave before electrical stimulation.

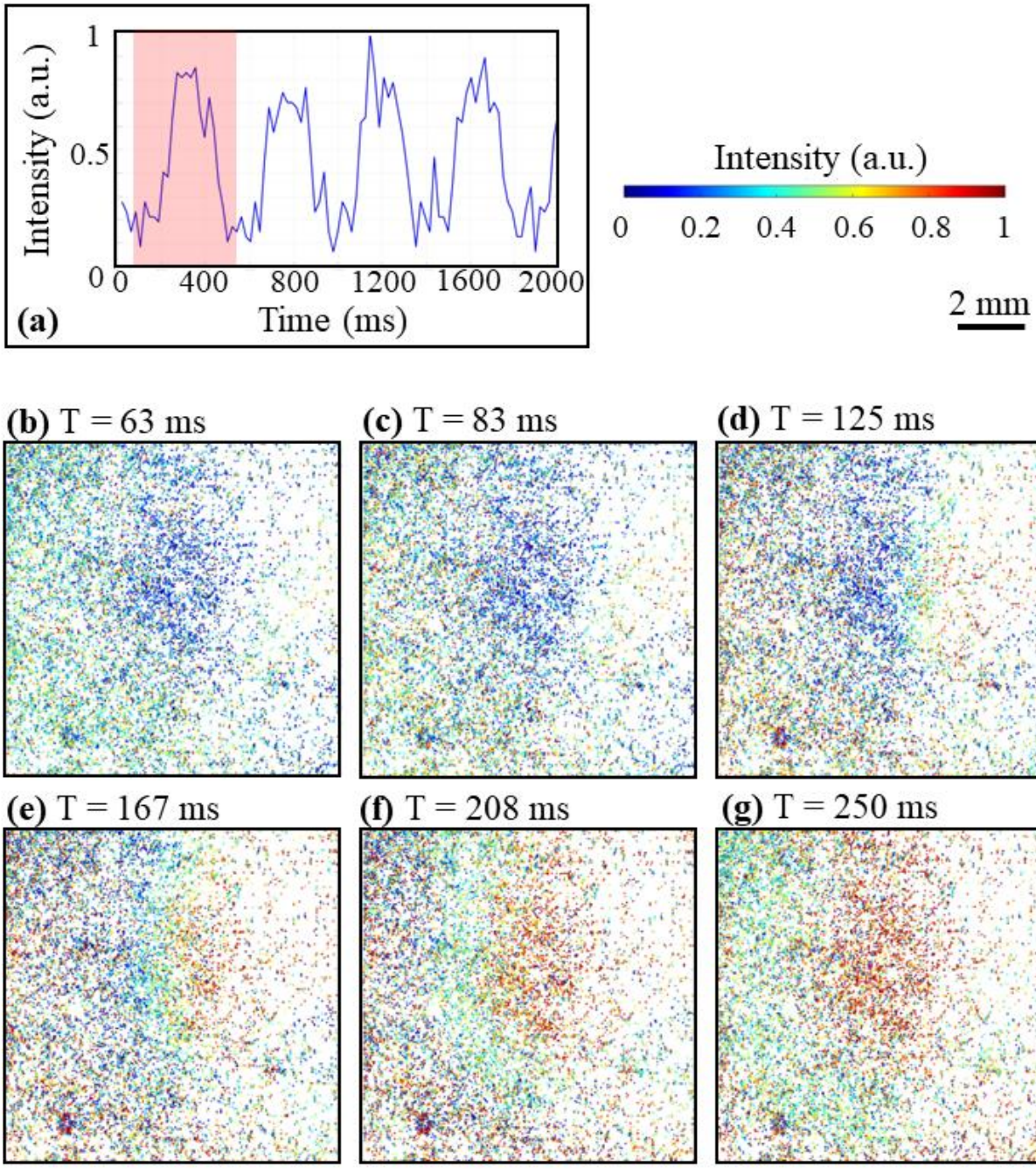
Intensity (a.u.)
1
0.5
0
0
400
800
1200
1600
2000
Time (ms)
(a)
Intensity (a.u.)
0
0.2
0.4
0.6
0.8
1
2 mm
(b) T = 63 ms
(c) T = 83 ms
(d) T = 125 ms
(e) T = 167 ms
(f) T = 208 ms
(g) T = 250 ms

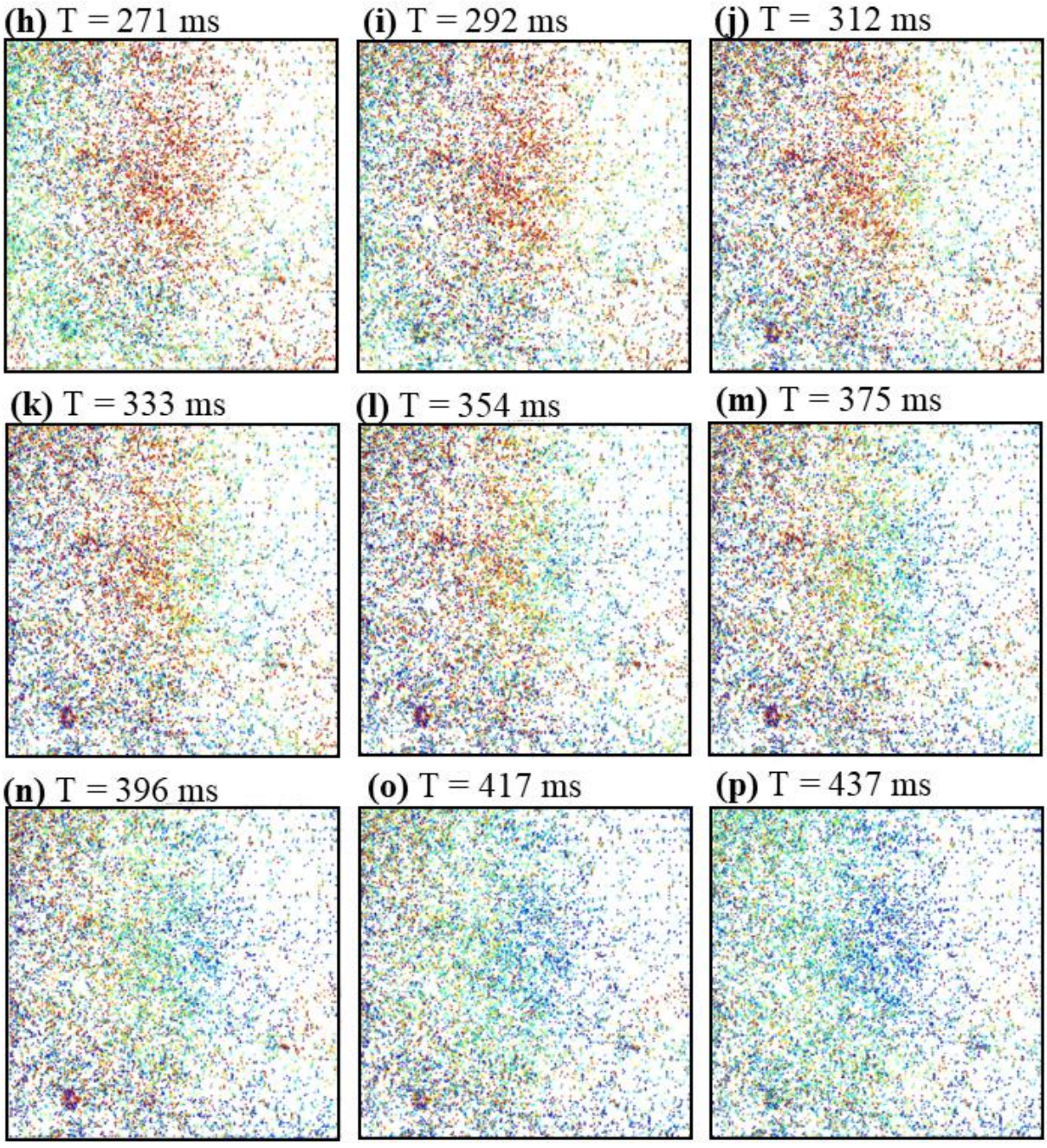

Figure 3.15 Time-course intensity change of the spiral wave 6-minute after electrical stimulation.

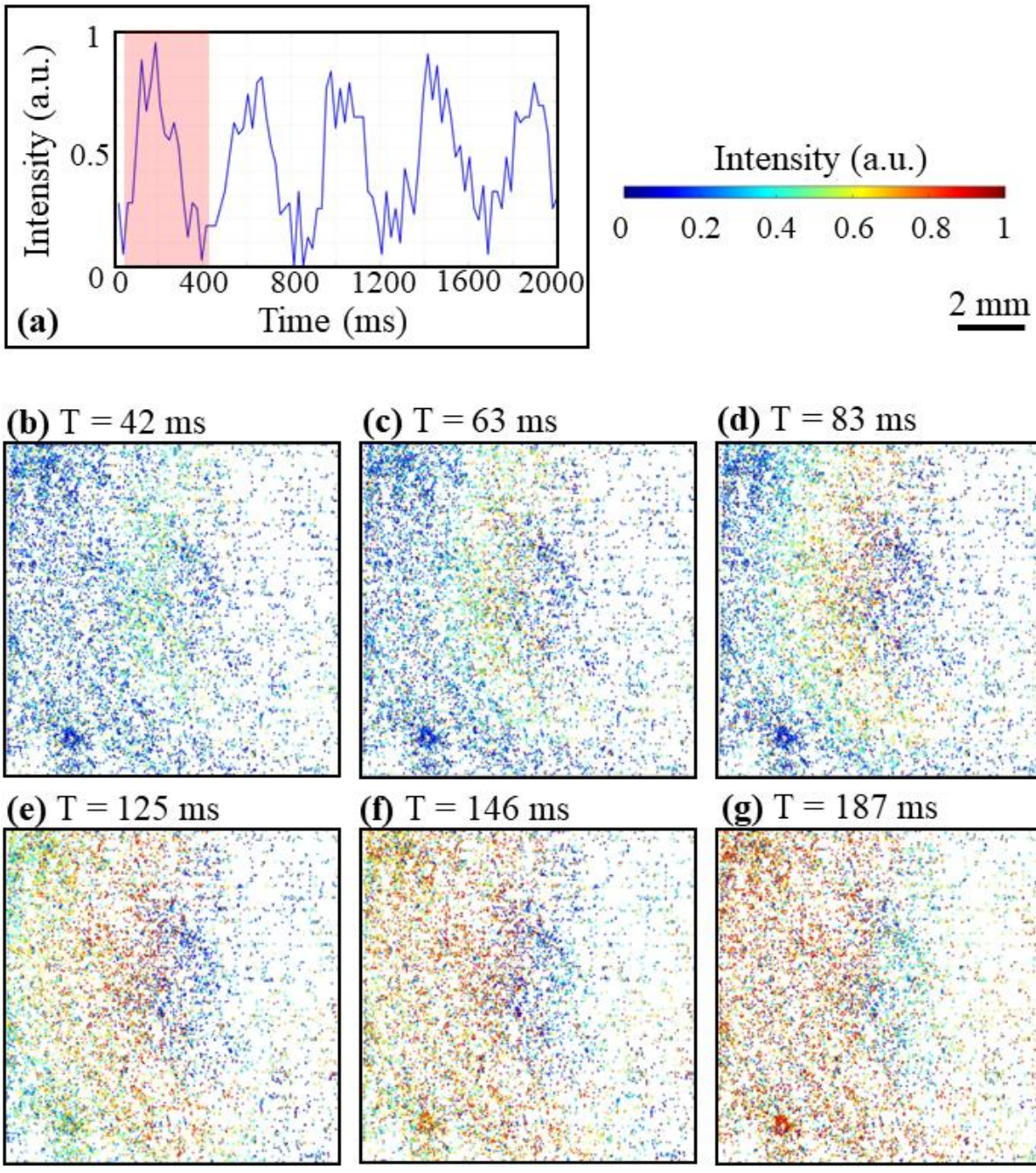
Intensity (a.u.)
1
0.5
0
0
400
800
1200
1600
2000
Time (ms)
(a)
Intensity (a.u.)
0
0.2
0.4
0.6
0.8
1
2 mm
(b) T = 42 ms
(c) T = 63 ms
(d) T = 83 ms
(e) T = 125 ms
(f) T = 146 ms
(g) T = 187 ms

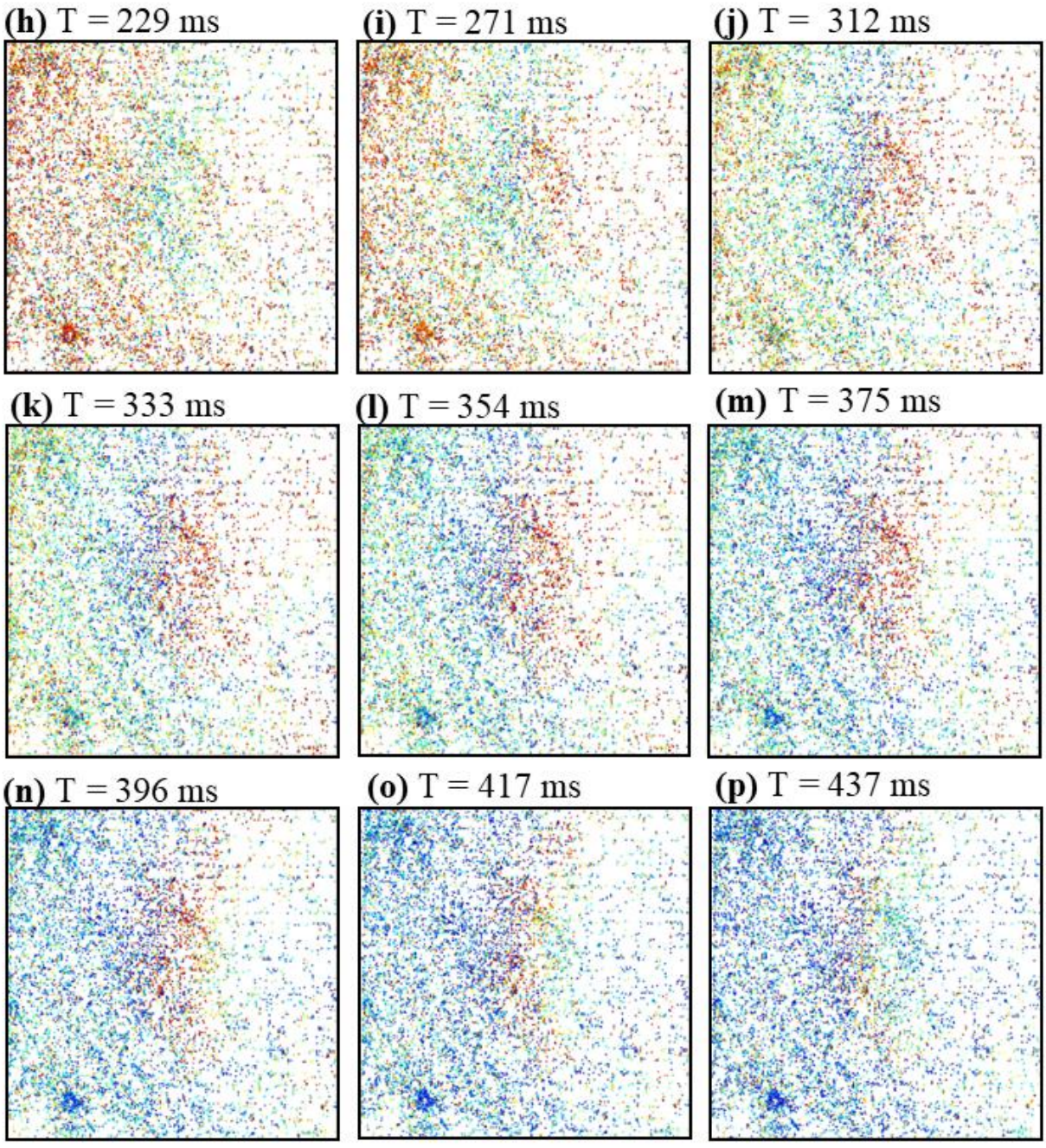

Figure 3.16 Time-course intensity change of the spiral wave 18-minute after electrical stimulation.

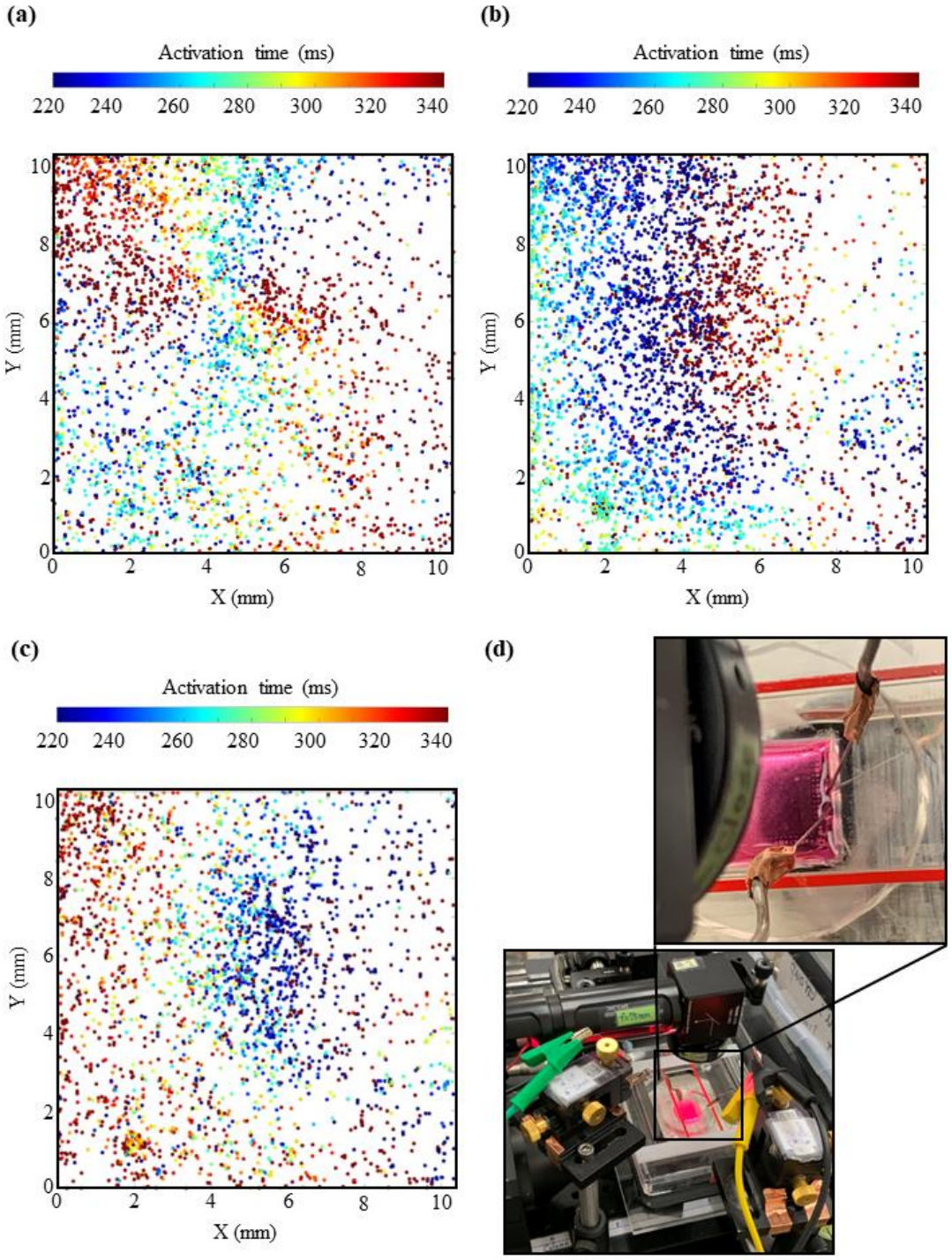

Figure 3.17 Activation time map (a) before electrical stimulation (b) 6-minute after stimulation (c) 18-minute after stimulation (d) photo of the stimulating electrodes.

Next, the dominant frequency of the constantly beating cells are calculated before and after electrical stimulation. In **Figure 3.18**, the time-course intensity traces are presented in the left column while their frequency spectrums obtained by fast Fourier transform are displayed in the right column. The frequency spectrums again are versatile, reflecting the diverse shapes of their counterparts in time domain. For example, some pixels beat consistently with a single dominant frequency (**Figure 3.18 (a)**) while some pixels contain two peaks in their frequency spectrum (**Figure 3.18 (b)**). On the other hand, there exist traces that feature abrupt changes or slow variations. The frequency spectrums are more broadband for those cases in general. Depending on the transient time, their spectrums will shift toward the high-frequency end (**Figure 3.18 (d) and (e)**) or the low-frequency site (**Figure 3.18 (c) and (f)**)). It should be noted that to remove the high-frequency noise and obtain a precise estimation of dominant frequency, a low pass filter (Cut-off frequency = 15 Hz) is first applied to the time-course intensity before taking the Fourier transform. The raw data and the filtered data are displayed as red dot line and blue solid line in the left column of **Figure 3.18**.

The frequency component that has the largest intensity value is considered as the dominant frequency of that pixel. The dominant frequency maps before electrical stimulation, 6-minute after stimulation and 18-minutes after stimulation are given in **Figure 3.19 (a)**, **(b)** and **(c)**, respectively. The mode values (most frequent number) of each case are 2.7 Hz, 2.32 Hz and 2.32 Hz. Thus, it seems that most cells beat slightly slower after electrical stimulation. Moreover, the histograms shown in **Figure 3.19 (d)**, **(e)** and **(f)** suggest that the percentages of the pixels with low dominant frequency somewhat decreased after electrical stimulation.

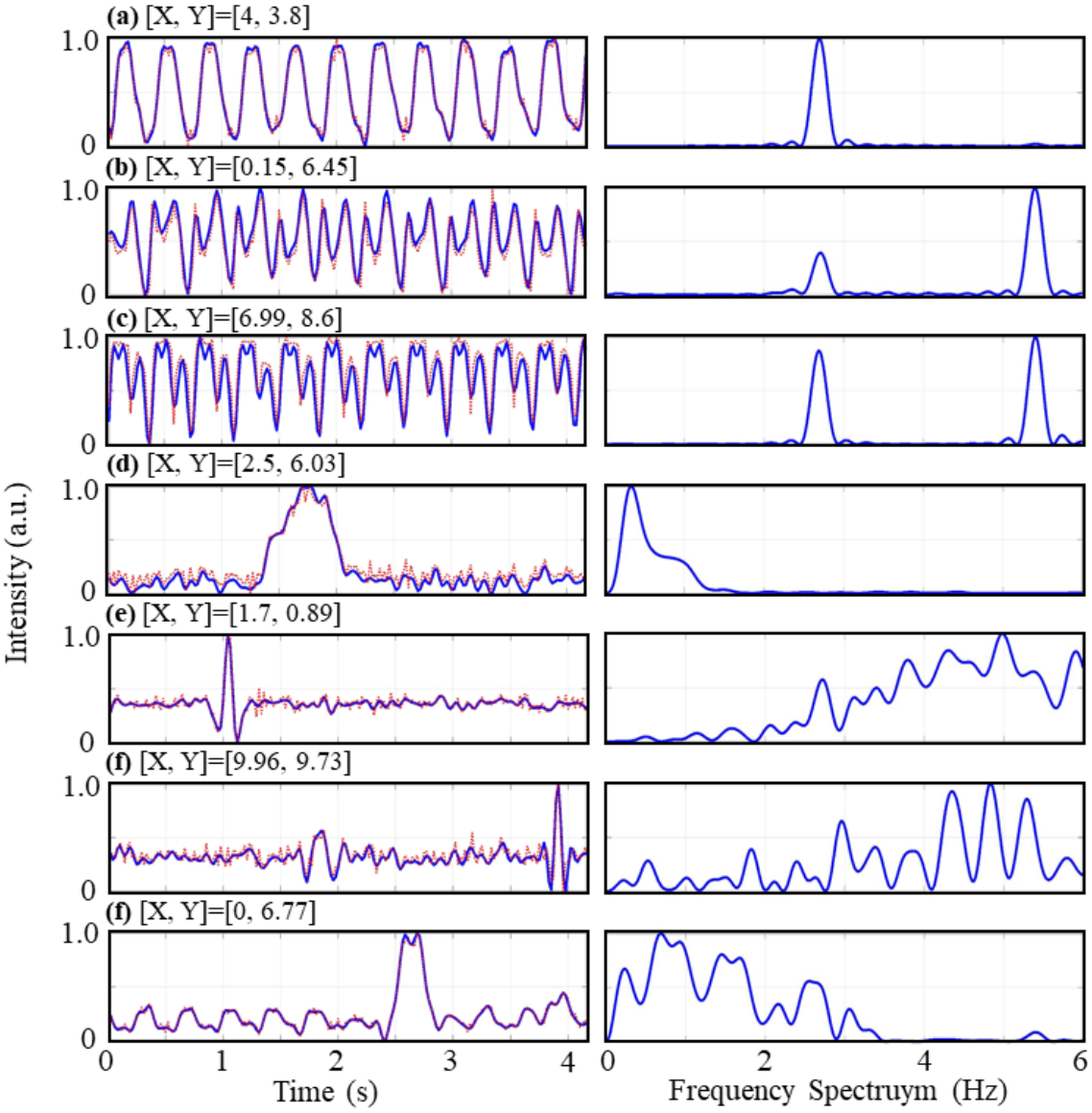

Figure 3.18 Time-course intensities and the frequency spectrum for some selected pixels.

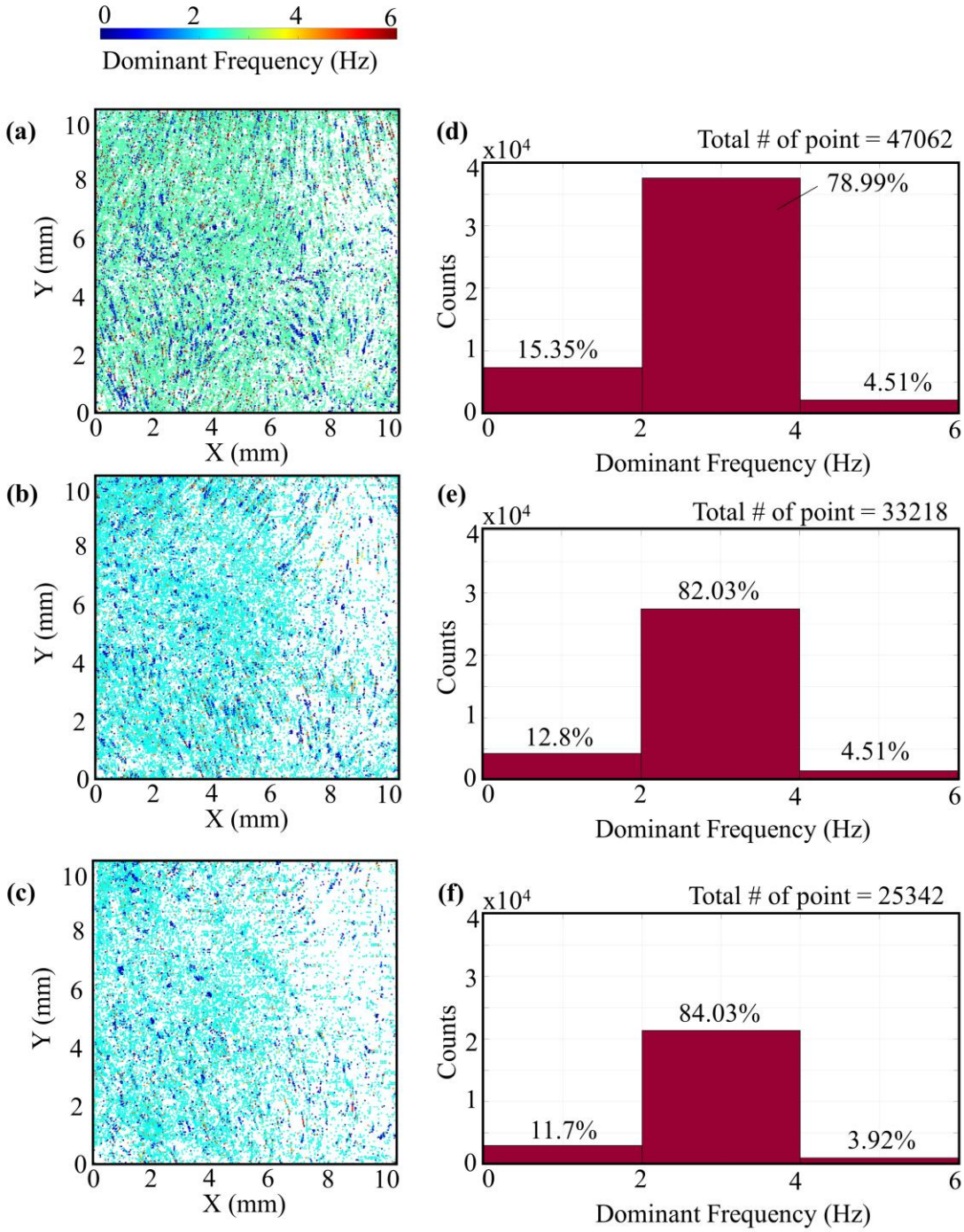

Figure 3.19 Dominant frequency map and histogram of the dominant frequency (a)(d) before electrical stimulation (b)(e) 6-minute after stimulation (c)(f) 18-minute after stimulation.

3.4.3 Chemical Stimulation

Next, to highlight the advantages of our platform in continuous, uninterrupted monitoring of biomechanical dynamics, a feature that is particularly desirable in drug testing and pathological evolution, the cells are treated with low-concentration (1 μM) phenylephrine (PE) and their responses over time are recorded. PE is a kind of α-1 adrenergic receptor agonist and will often induce hypertrophic responses of cardiomyocytes. The timing when PE is added to the sample is labelled as zero along the time axis. Thus, the measurements conducted before adding drug will have a negative time while the measurements performed after adding drug will have a positive time. The total treatment time is 153 mins. It should be noted that for the device used for this experiment, the left-top corner is damaged by defects. Therefore, no information can be collected for that area.

To begin with, the change of the dominant frequency over time from the bulk of cells is given in **Figure 3.20 (a)**. Overall, the dominant frequency continually increased with a drop at Time = 13 minutes. Then, the increase slowed down. A plateau period is observed between Time = 23 minutes and Time = 43 minutes. Afterward, the dominant frequency grew steadily till the end of the experiment (Time = 153 minutes), with a smaller increasing rate compared to the one at the beginning.

Figure 3.20 (b) to (k) demonstrates the spatial distribution of dominant frequencies at different times before and after drug treatment. The evolution of spatial patterns can be clearly inspected. Specifically, at the beginning, there are three main clusters of cells, appearing at the top-right, bottom-left, and bottom-right corner (Time = -18 minutes and -13 minutes, **Figure 3.20 (b)** and **(c)**). The bottom-left cluster disappeared just before adding drug (Time = -3 minutes, **Figure 3.20 (d)**). In general, the cells in different clusters beat with the same frequencies.

Subsequently, after adding drug, the two separated clusters at the top-right and bottom-right corner gradually connected and beat more synchronically (**Figure 3.20 (e)**, **(f)** and **(g)**). Moreover, the connections are further extended to the bottom-left corner as time evolved (**Figure 3.20 (h)**, **(i)**, **(j)**, and **(k)**). On the other hand, the histograms of the dominant frequency are shown in the inset of each figure from **Figure 3.20 (b) to (k)**. In addition to the increase of the dominant frequency, we noticed that after drug treatment, the percentage of cells that beat coordinately with the majority rose while the percentage of cells that show slow response declined over time.

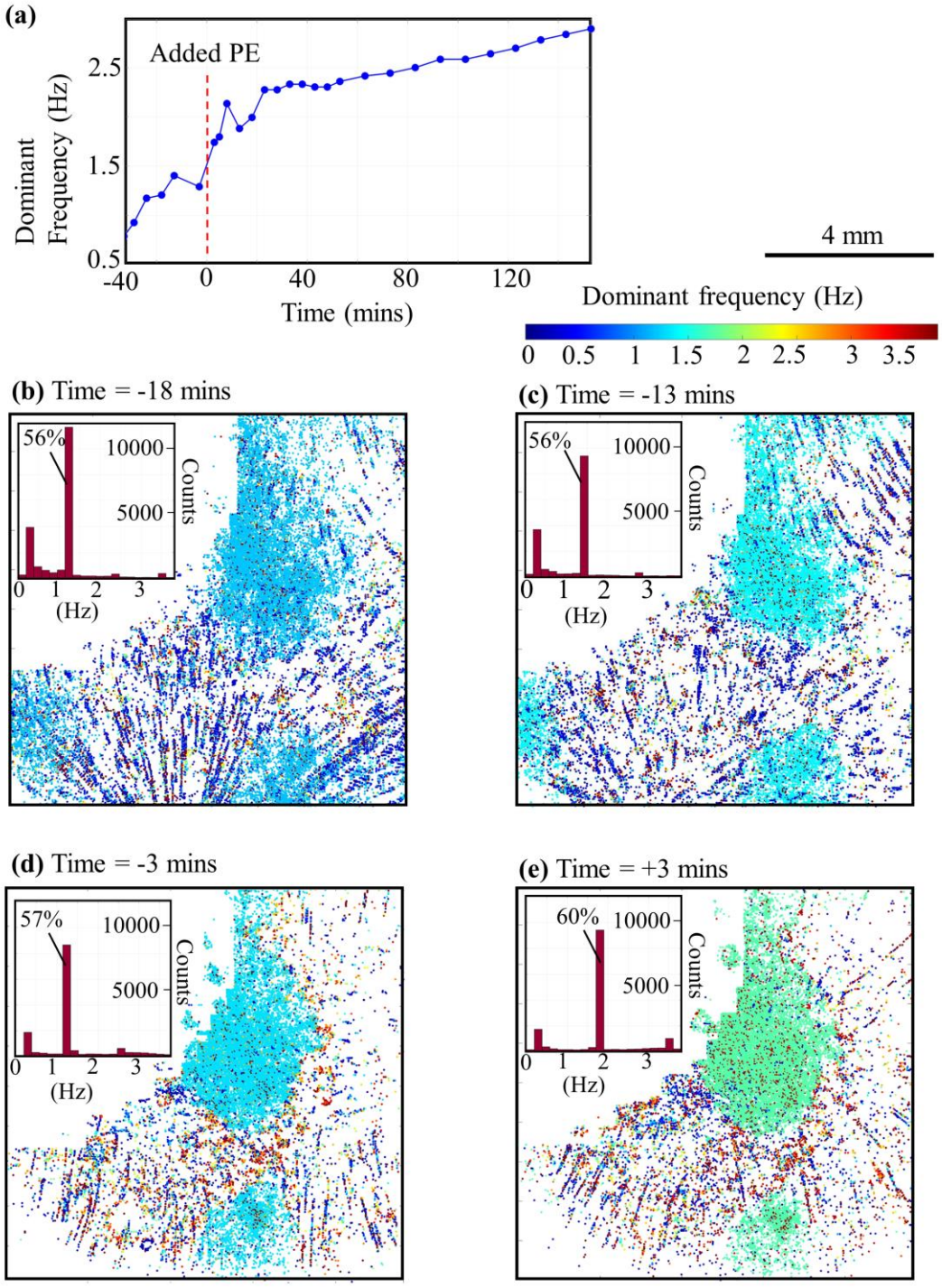
(a)
Added PE
Dominant Frequency (Hz)
2.5
1.5
0.5
-40
0
40
80
120
Time (mins)
4 mm
Dominant frequency (Hz)
0 0.5 1 1.5 2 2.5 3 3.5
(b) Time = -18 mins
56%
10000
5000
Counts
0 1 2 3
(Hz)
(c) Time = -13 mins
56%
10000
5000
Counts
0 1 2 3
(Hz)
(d) Time = -3 mins
57%
10000
5000
Counts
0 1 2 3
(Hz)
(e) Time = +3 mins
60%
10000
5000
Counts
0 1 2 3
(Hz)

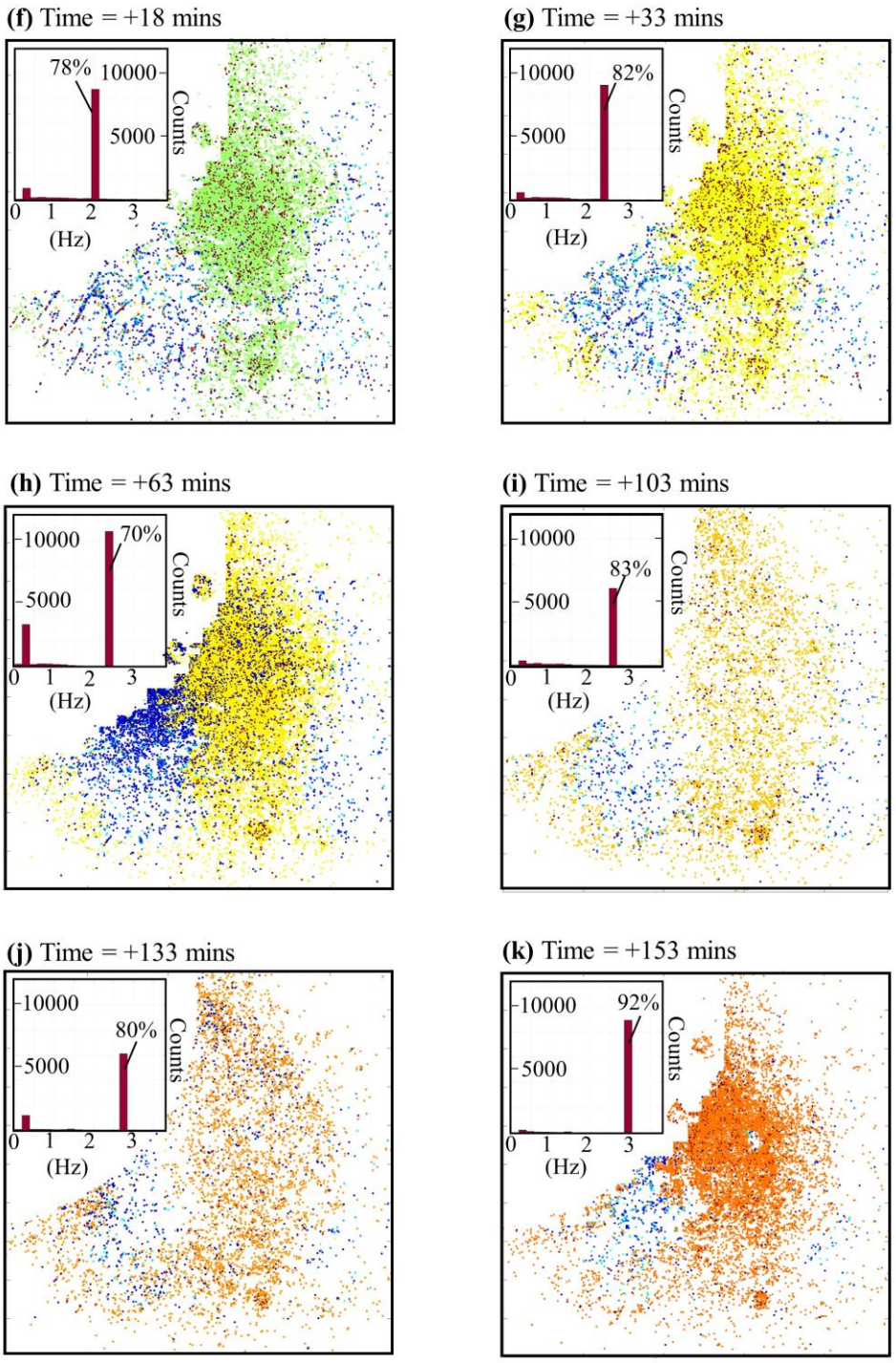

Figure 3.20 (a) The change of the dominant frequency over time for the majority of cells. (b) to (k) the dominant frequency maps at certain times before and after adding drug. The inset shows the histogram of dominant frequency.

Additionally, we observe that there existed radiating patterns, mainly appeared in between the three major clusters. The patterns are particularly evident before drug addition (Time = -18 minutes and -13 minutes, **Figure 3.20 (b)** and **(c)**). The dark blue color suggests that their dominant frequencies are lower than the main beating. To further investigate these points, we plot the distribution of low frequency component (dominant frequency < 1 Hz) separately in **Figure 3.21** and track those points for their time-course intensity change (**Figure 3.22 (a) to (n)**).

The left column and the right column of **Figure 3.22** follow two neighbouring radiating lines. The tracked points along the two lines are marked in **Figure 3.22 (o)** with blue and red color, respectively. From the traces of **Figure 3.22 (a)** to **(g)** and **Figure 3.22 (h)** to **(n)**, the radiating distribution are originated from slow-propagating waves that occur randomly and uncoordinatedly with the main beating. The conduction velocities between these points are estimated by dividing the distance by the difference in the arriving time of the main peak. The arriving time of the main peak is labelled in **Figure 3.22 (a)** to **(n)** while the conduction velocities (CV) are illustrated in **Figure 3.22 (o)**. The unit of conduction velocity in the figure is mm/s. Since the trace shapes are very versatile and multiple peaks emerged for some cases, it is possible that they are initiated from different origins and the selection of the main peak may cause the calculation error of conduction velocity to some degree.

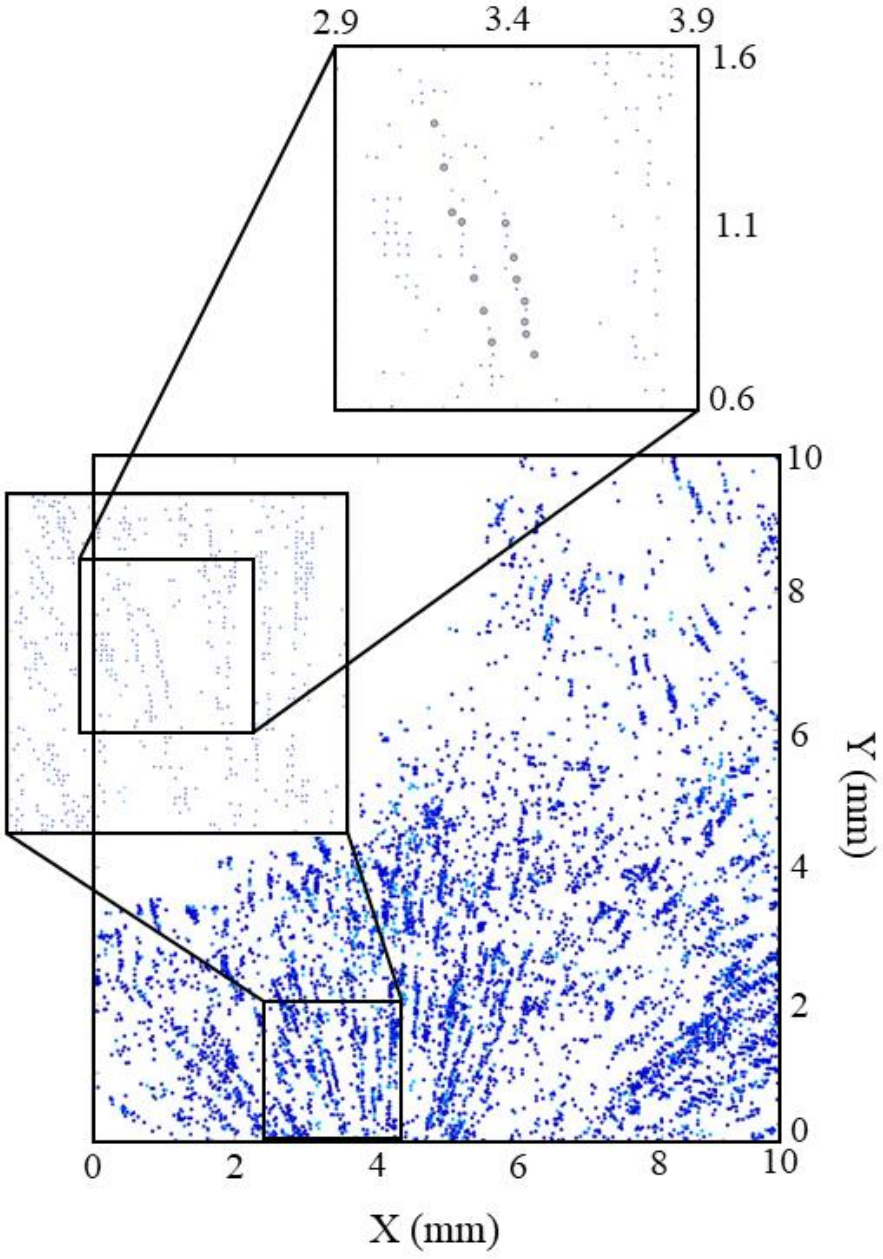

Figure 3.21 Distribution of pixels with dominant frequency <1Hz. The points with their time-course intensities plotted in Figure 3.22 are marked by the black circles in the inset.

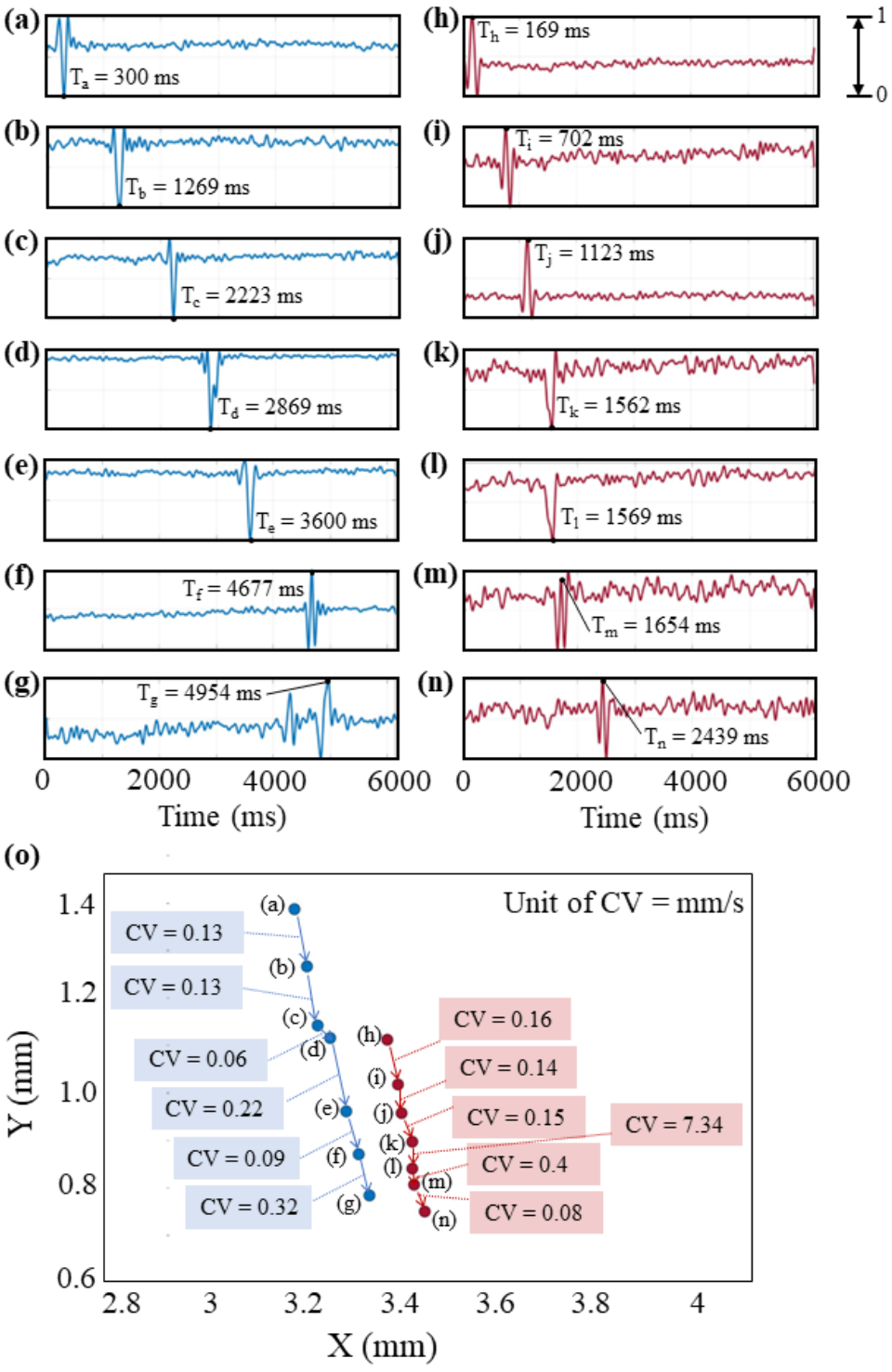

Figure 3.22 (a) to (n) Selected pixels with low dominant frequency along two radiating direction. (o) the conduction velocities between the selected points along two radiating lines.

On the other hand, there exists some points oscillating at higher frequencies than the majority. The distribution of the pixels with their dominant frequencies larger than 2Hz are plotted in **Figure 3.23 (a)** with three selected traces of time-course intensity displayed in **Figure 3.23 (b)**.

Finally, maps of activation time at four different timings before and during the drug treatment are given in **Figure 3.24** with three time-course intensity displayed in the insets. To be more specific, at Time = -18 minutes, the onset of the waveform is from the cluster at the bottom right and then propagates to the bottom left and then the top right (**Figure 3.24 (a)**). Nevertheless, as time went on and after drug addition, the waveform started to initiate from the top and progressed to the bottom, with the linkage between the top and bottom clusters (**Figure 3.24 (b), (c), and (d)**), especially at the end of the drug treatment.

To summarize, our platform is a powerful tool to profile the evolution of biomechanical dynamics in both temporal and spatial domain with unprecedented resolution and considerably large field-of-view. This will be extremely effective and useful for applications such as screening of candidate drugs and studies of the pathological developments.

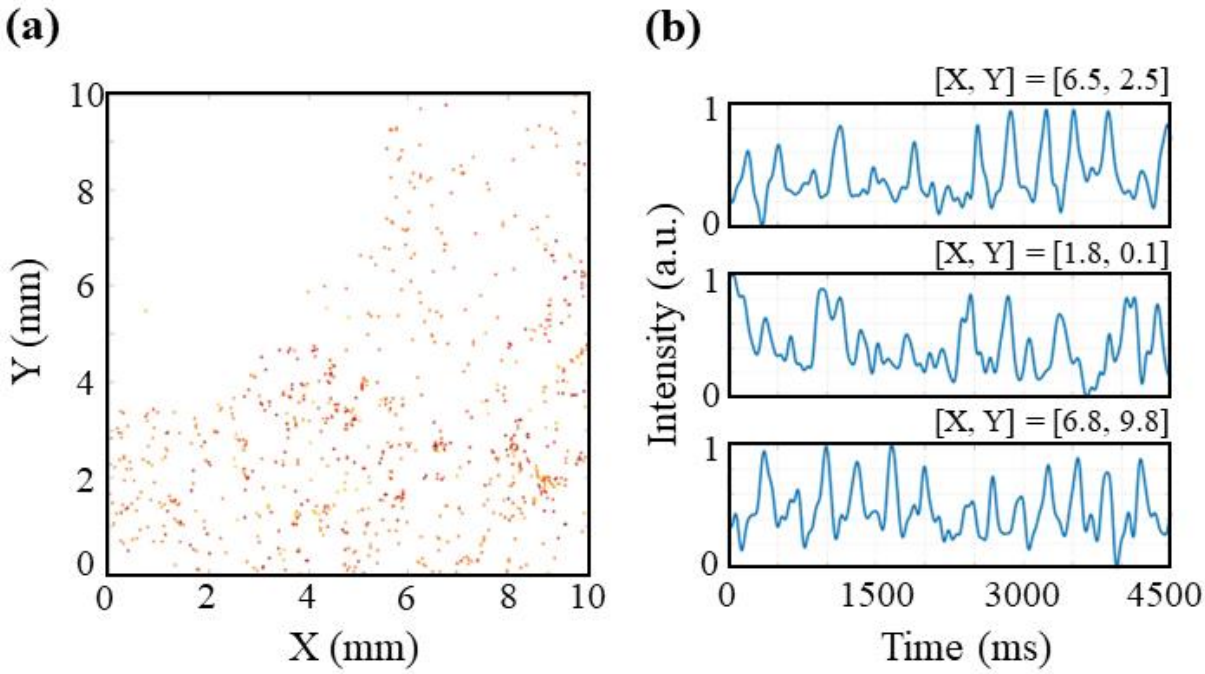

Figure 3.23 (a) Distribution of pixels with high dominant frequency (>2Hz) (b) time-course intensity change of three selected pixels.

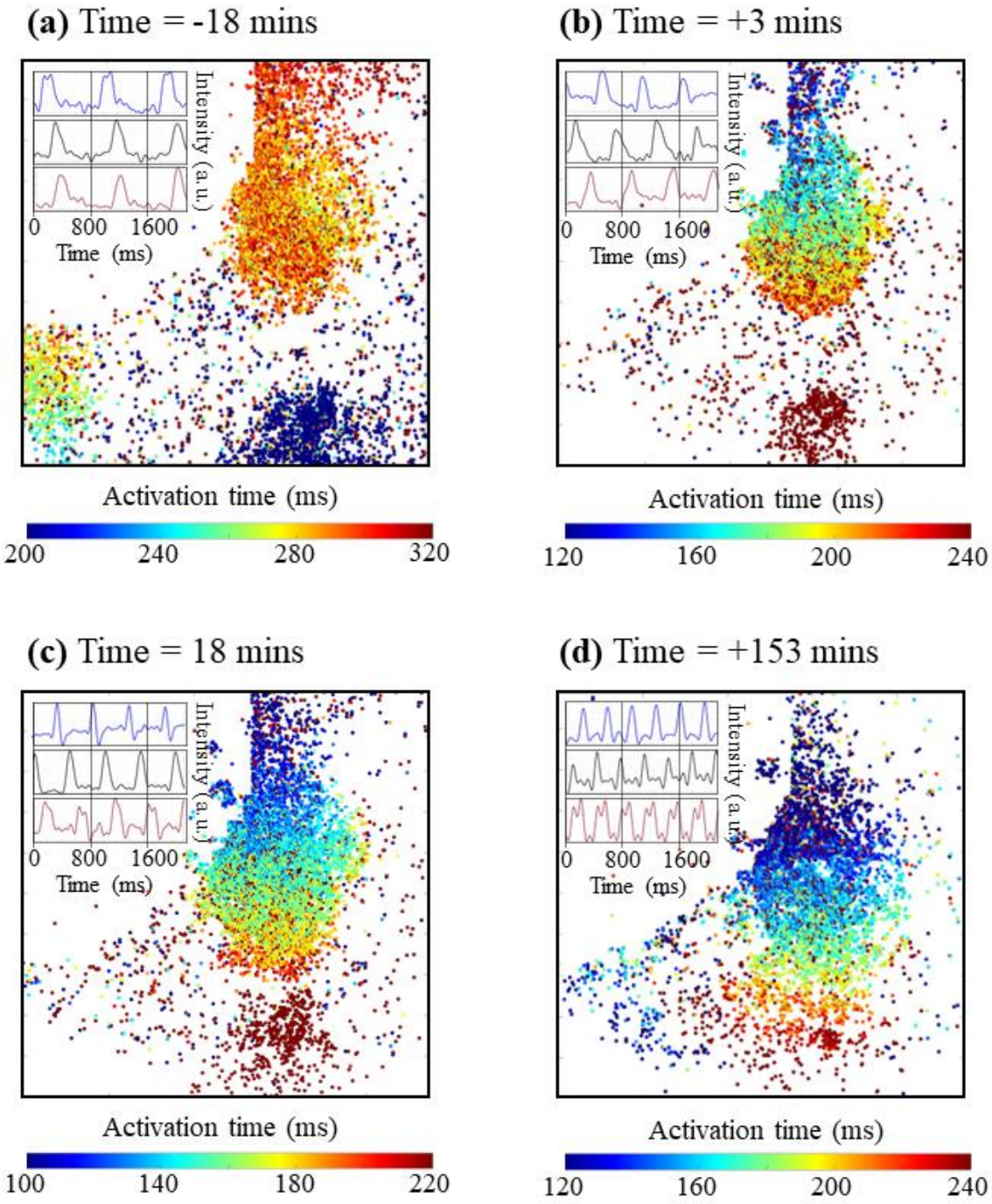

Figure 3.24 Activation time map before and during drug treatment (a) 18-minutes before treatment (b) 3-minute after treatment (c) 18-minutes after treatment (d) 153-minute after treatment.

3.4.4 Long-Term Observations of Biomechanical Dynamics

As cell cultures grow and mature over time, if their biomechanical dynamics can be recorded without disturbing their physiological activities, the uncertainty associated with external factors can be excluded readily. Therefore, it will be more straightforward to recognize the causality of certain biological events and study their interactions. Hence, in this subsection, we would like to emphasize our platform's strength to conduct long-term observation of cells under native conditions by continually logging the biomechanical dynamics of the same cell culture daily for up to 7 days. The day that the NRVM cells are isolated and seeded on the device is called Day 0. The cells usually start beating 24 to 48 hours after seeding. We started the measurement on Day 3 and repeated it every day till Day 9 (Detailed time frame is given in **Appendix C**). The maps of activation time, along with three chosen time-course intensity traces on each day are shown in **Figure 3.25**. The cell cultures and device were used for the chemical stimulation on Day 7 (for the data presented in **Section 3.4.3**). Therefore, the same as the situation presented in **Section 3.4.3**, the top-right corner of the device is unable to collect useful information due to the defects.

On Day 3, regular beatings with 0.81 Hz rate were recorded. The onset of the beating was from the top-left and propagated to the bottom-right corner (**Figure 3.25 (a))**. Then, on Day 4, the beating pattern followed the same spatial arrangement, that is, traveling from the top-left to the bottom-right. However, the beatings were not consistent. Only two were captured over the entire 16.8-second recording. Although the beating activity was not steady, the captured two beatings have similar time difference as those on the previous day (1.25s). Interestingly, the activation time map has denser points compared to the one on the previous day (Day 3). This may somewhat indicate that there were more cells engaged in the beating activities; therefore, larger traction forces were applied on the device to activate more diffractive elements (**Figure 3.25 (b)**).

Next, no clear beatings were recorded on Day 5. Subsequently, on Day 6, a spiral pattern appeared with a beating rate of 4.4 Hz (**Figure 3.25 (c)**). Afterward, chemical stimulation was performed on Day 7. That is, low-concentration (1 μM) phenylephrine (PE) was added to the culture medium and treated for 153 minutes. As described in **Section 3.4.3** and illustrated in **Figure 3.25 (d)**, there were two clusters at the top right and top bottom, beating with a 1.29 Hz rate just before the drug administration (time = -3 minutes). At the end of the treatment, the beating frequency increased to 2.89 Hz with the two clusters becoming more connected (**Figure 3.25 (e)**). The drug was removed at the end of the experiment. Fresh medium was replenished to the cells culture. After the cells were incubated overnight, the recording was conducted again on Day 8. The connected clusters separated and there was a longer delay between their activation time. The bulk of the cells beat at 0.51 Hz. Nonetheless, some heterogeneous pixels have more beatings in between the main ones (**Figure 3.25 (f)**). Lastly, on Day 9, only the cluster on the top-right corner remains constantly beating at 2.5Hz. The beating was initiated from the bottom of the cluster and travelled to the top, as opposite to the directions shown in the previous few days. Also, it is interesting to note that there were two consecutive peaks associated with each beating **Figure 3.25 (g)**.

In short, long-term observations of large-area biomechanical dynamics are achieved with the span extended to a week, with minimum interruption to the physiological activities of cells. This cannot be accomplished by the conventional optical mapping using fluorescent dyes. Dye internalization, photobleaching and phototoxicity all impose limitations on the maximum observation duration. Observation window cannot exceed several hours typically. Moreover, the physiological impacts of dyes on cells are still under debate and will vary from different dyes used specifically in the experiments.

(a) Day 3

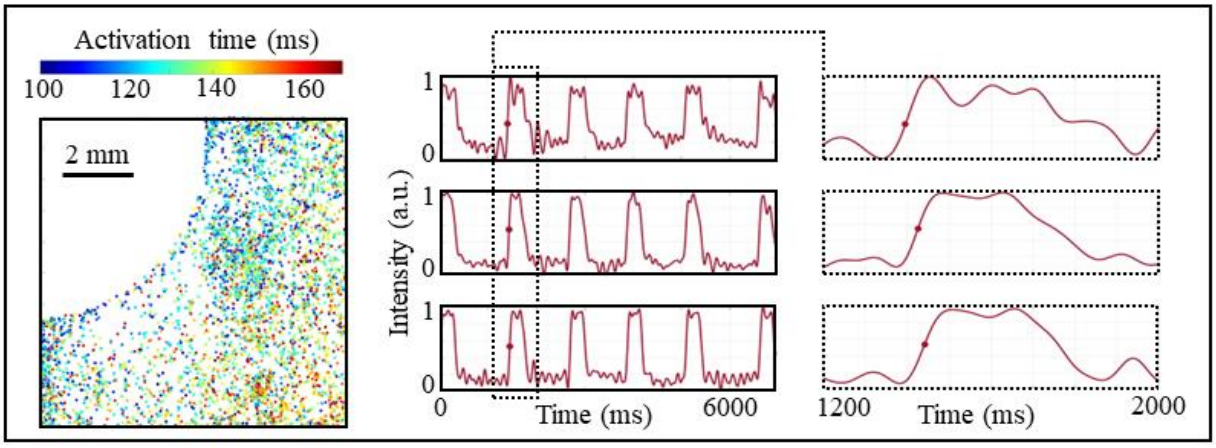

(b) Day 4

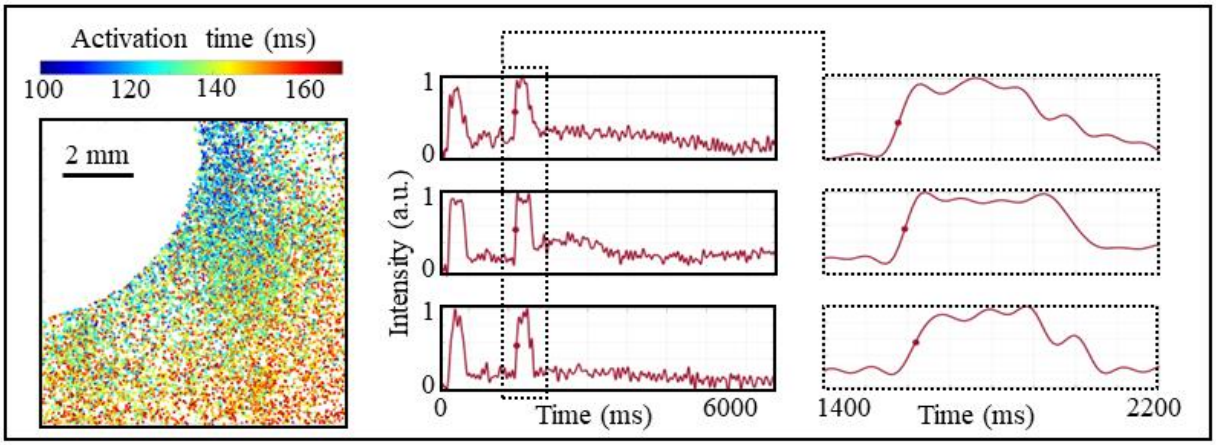

(c) Day 6

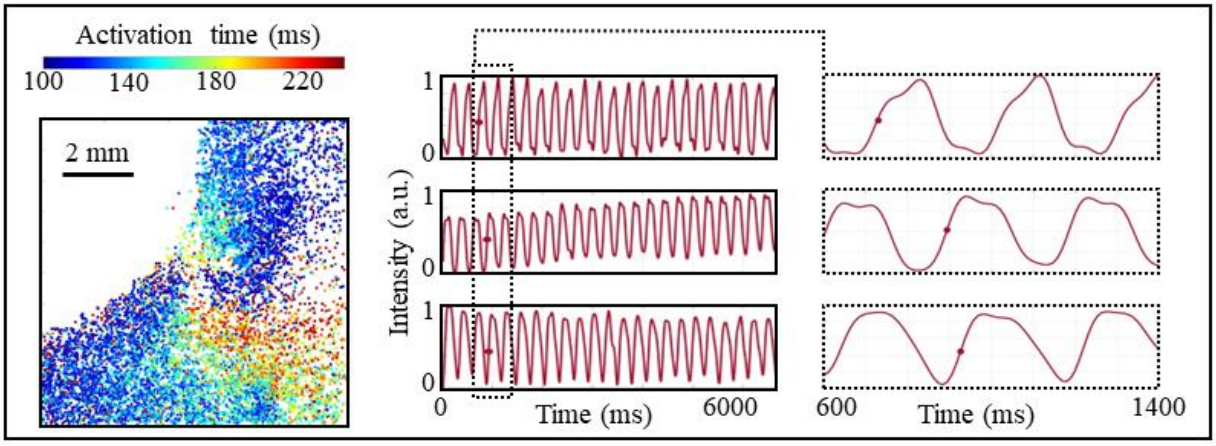

(d) Day 7 (Before drug treatment)

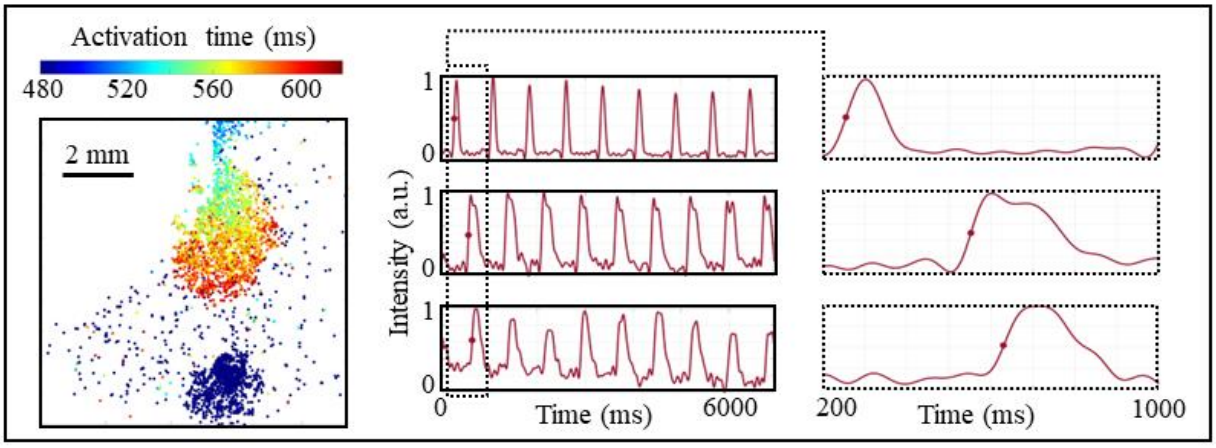

(e) Day 7 (After drug treatment)

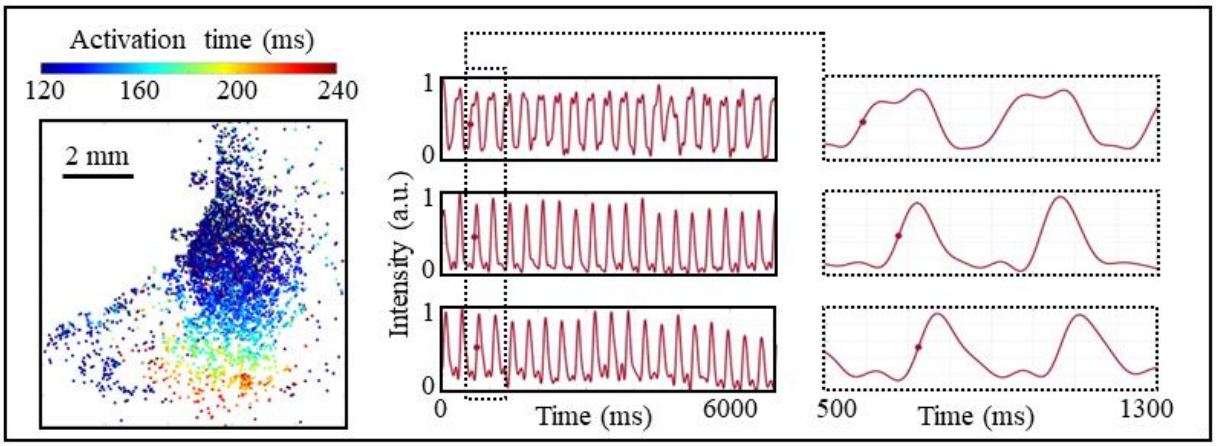

(f) Day 8

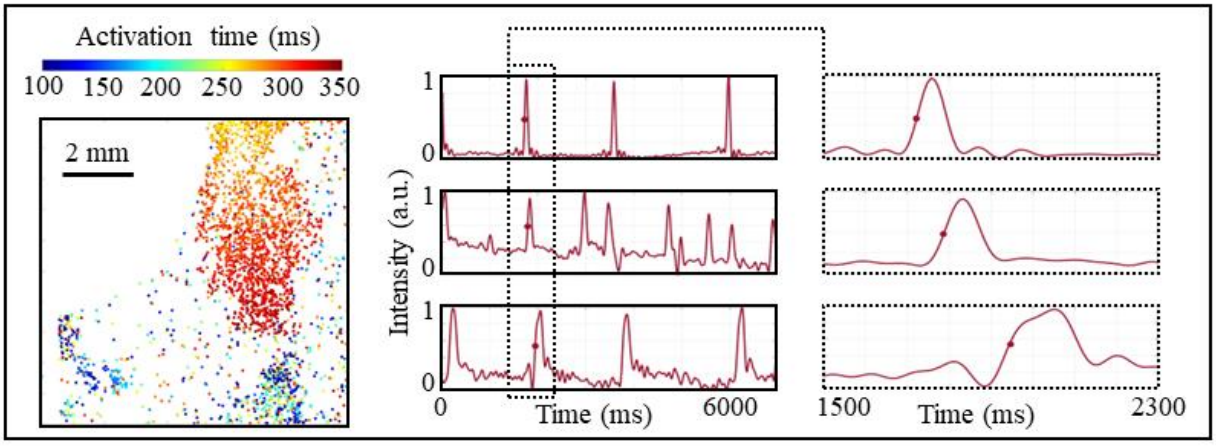

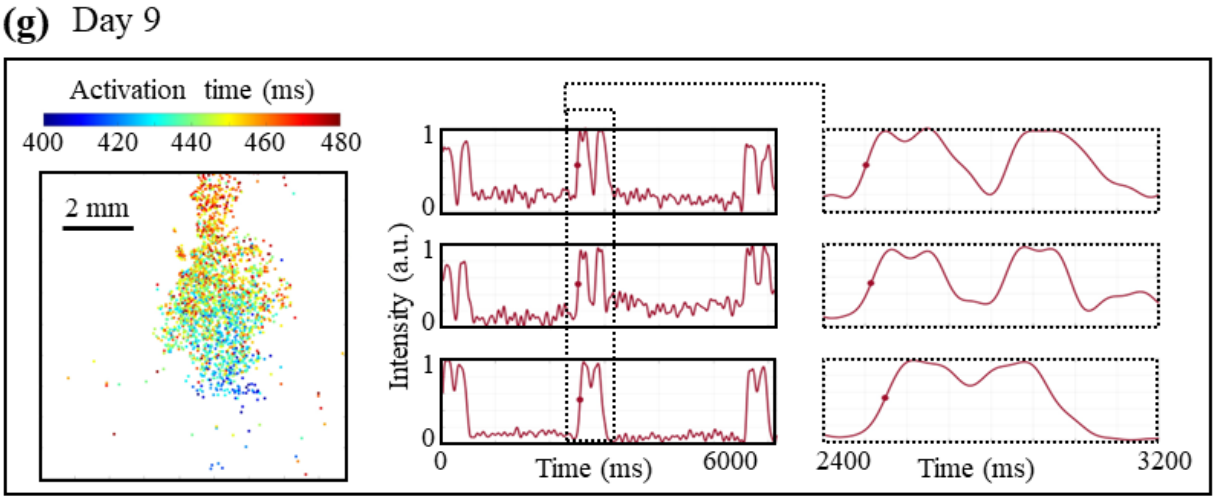

Figure 3.25 Long-term measurements of biomechanical dynamics. Activation time map and selected time-course intensities are shown (a) Day 3 (b) Day 4 (c) Day 6 (d) Day 7 before drug treatment (e) Day7, after drug treatment (f) Day 8 (g) Day 9.

3.4.5 Simultaneous Measurements of Calcium Ions Concentrations and Biomechanical Dynamics

As discussed in **Section 1.2**, dynamic equilibrium in biological systems and coupling between different properties are crucial for a multicellular system to function properly. Therefore, although fluorescent dyes may slightly alter physiological activities of cells, they can still provide critical information complementary to our measured biomechanical properties in some situations. Examples of informative details that can be offered by fluorescent imaging are the action potentials, ion concentrations, or morphological configurations. Furthermore, simultaneous measurements of multiple parameters, such as bioelectrical, biomechanical, biochemical properties, allow us to investigate the cellular system from different aspects and understand the interplays between these properties. Hence, we upgraded our platform to include the optics required to conduct fluorescent imaging. Consequently, concurrent measurements of calcium ion concentration with the biomechanical dynamics are performed as a proof-of-concept.

The schematics and the photo of the upgraded setup with the functionality of fluorescent imaging are displayed in **Figure 3.26 (a)** and **(b)**. The dichroic mirror, emission filter, camera lens and camera are arranged and aligned along the reflective path to capture the fluorescent signal emitted by the cells after staining. Meanwhile, biomechanical dynamics can still be measured using the transmitted path without modification. The reflective and transmitted path shared the same illumination. Thus, the illumination wavelength is chosen according to the excitation spectrum of the fluorescent dyes. The two cameras (for measuring fluorescent signals and measuring biomechanical dynamics) are synchronized temporally by operating them in hardware trigger modes and feeding them the same trigger signal. On the other hand, to spatially align the images acquired by the two cameras, the images are first converted to millimeter unit and then align using the alignment markers on the device (seeded with cells). Due to the size of the alignment markers

and the small magnifications (0.5x to 0.73x) of our system, this step only gives us a rough idea of the relative locations. More details of the experimental setup can be found in **Appendix B**.

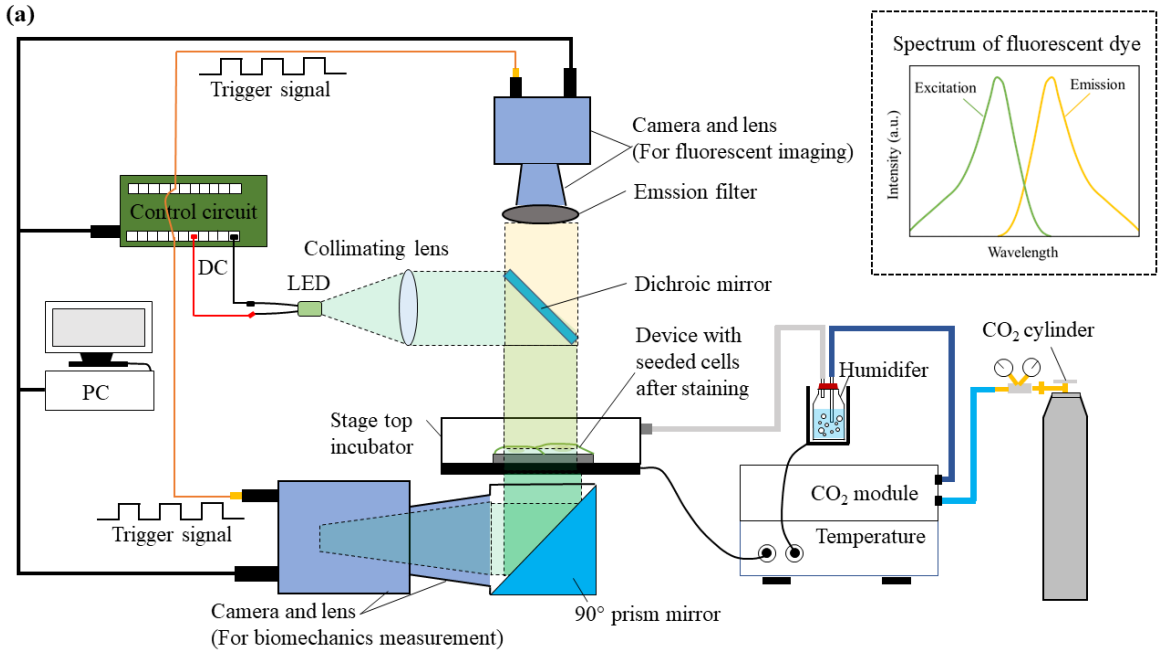

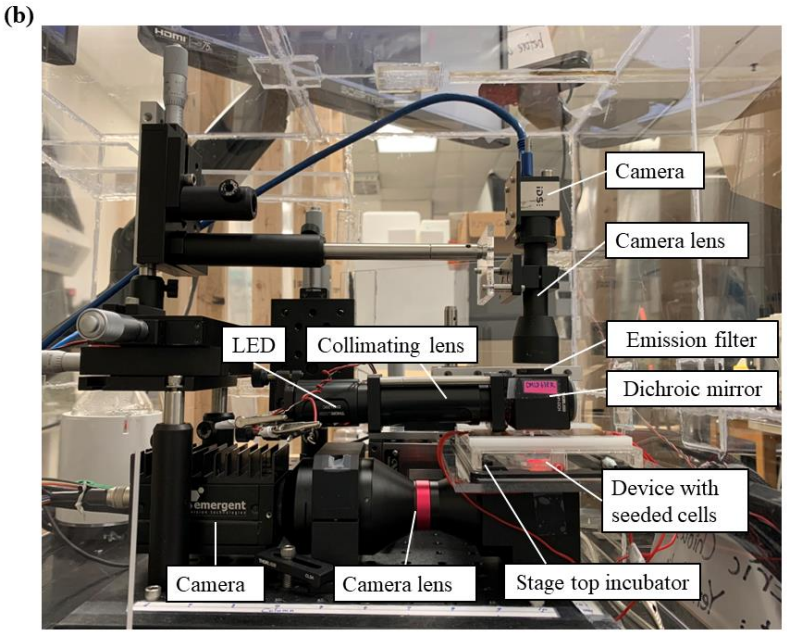

Figure 3.26 (a) Schematics of the LAMBDA platform integrated with a reflective-type fluorescent imaging (b) photo of the updated setup.

Calcium ions (Ca^{2+}) are essential elements in muscle contractions. Without Ca^{2+}, muscles cells won't be able to contract and relax properly. Therefore, Ca^{2+} concentration is usually measured as an indirect indication of muscle contraction or cardiac beating. High-affinity calcium ion (Ca^{2+}) dye "Rhod-2" is utilized for fluorescent imaging in our experiments. Detailed dye loading protocol is given in **Appendix B**. Rhod-2 is a common fluorescent dye used in optical mapping to profile large-area Ca^{2+} concentrations. Its high affinity feature allows fast and transient change of Ca^{2+} concentrations to be accurately captured. However, this high-speed nature imposes an ultimate restriction on the exposure time of the image sensor (Maximum exposure time = 1/frame rate). Consequently, the signal acquired is often low. In addition, we rely on the "change" of fluorescent signal to track the change of Ca^{2+} concentration. Nonetheless, typically, the fractional change of these fluorescent dyes is not significant (< 30% for most of the dyes). Taken together, to overcome these challenges, conventional optical mapping often relies on specialized equipment to collect fluorescent signals for the large-area measurements during the short exposure period. For example, the cameras adopted in optical mapping often have extremely large pixel sizes (few tens of micrometers to a few hundred micrometers per pixel) but small pixel numbers (256x256 to 16x16). Additionally, these specialized setups are often expensive and will cost almost $100k USD for the whole system.

Due to the challenges of optical mapping using fluorescent dyes aforementioned, with our current fluorescent imaging setup, we cannot capture the change of fluorescent signal that reflects the Ca^{2+} concentration for the whole field-of-view (16mm x 14mm). The distribution of the pixels that show large change in the fluorescent intensity is plotted in **Figure 3.27 (a)**. They are sparsely scattered, and it is difficult to recognize any spatial beating pattern from these scattered points. On the contrary, for the same beating, the map of activation time measured by our LAMBDA platform

that indicate the biomechanical dynamics is shown in **Figure 3.27 (b)**. The spiral pattern is clearly visualized. Apparently, the data obtained by our platform provides much more details including the spatial beating patterns and the fine spatial resolutions.

Then, we would like to compare the time-course intensities that indicate Ca^{2+} concentration and biomechanical dynamics. Among the pixels that show large change in the fluorescent intensity, we selected those that show constant beatings and plot them in **Figure 3.27 (c)** (Blue curves, labelled as "F[Ca^{2+}]"). Meanwhile, for comparison, we picked up the intensity measured by our LAMBDA platform at the same or neighboring locations and also plot them in **Figure 3.27 (c)** (Red curves, labelled as LAMBDA). It can be observed that the fluorescent signal and the LAMBDA signal are highly correlated with similar trends and shape, verifying the fact that the calcium concentrations and the biomechanical dynamics are closely related in the physiological activities of muscle contractions naturally.

Next, it was brought to our attention that, for the distribution of pixels with large change in fluorescent intensity (**Figure 3.27 (a)**), there exist radiating patterns, very similar as the patterns we observed in **Section 3.4.3** for the slow-wave propagation (**Figure 3.21** and **Figure 3.22**). To check whether there are corresponding patterns in the biomechanical properties, the map of dominant frequencies measured by the LAMBDA platform is demonstrated in **Figure 3.28 (a)**. Two zoom-in areas of **Figure 3.28 (a)** are given in **Figure 3.28 (b)** and **(c)** while **Figure 3.28 (d)** and **(e)** display the same areas from the distribution of pixels with large change in fluorescent intensity (**Figure 3.27 (a)**)). By comparing **Figure 3.28 (b)** with **Figure 3.28 (d)** and **Figure 3.28 (c)** with **Figure 3.28 (e),** there are matching radiating patterns for the data measured by the LAMBDA platform and the fluorescent signal in the same spatial locations. Moreover, some representative pixels from the locations that show radiating patterns are chosen with their time-

course intensity change shown in **Figure 3.29**. Overall, both the fluorescent signal and the intensity measured by the LAMBDA platform feature slow-varying changes at similar timing. Again, the experimental results suggest that the activities of calcium concentrations and the biomechanical dynamics are highly correlative.

Finally, we would like to emphasize the strengths of our platform to provide high spatial resolution and high sensitivity for recording the biomechanical dynamics. While the fluorescent signal can only have sparse points that reflect the change of calcium concentrations, for the same beating, our platform captures the pattern over the entire field-of-view with unprecedented details. The time-course intensity distributions given in **Figure 3.30** is pronounced evidence that our platform outperforms the fluorescent imaging for recording larger-area dynamics in this case.

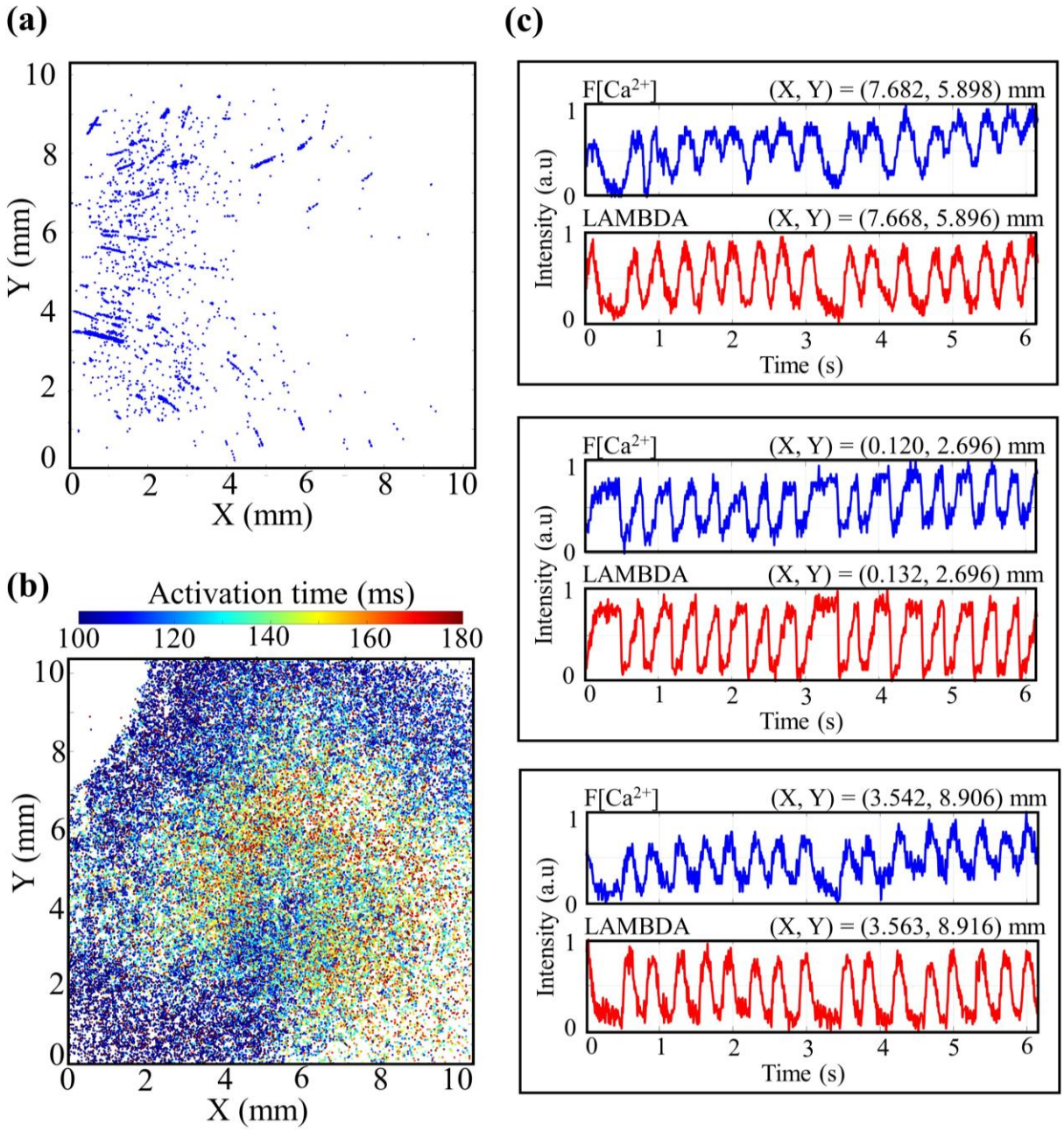

Figure 3.27 (a) Distribution of pixels with large fluorescent signal change (b) activation time map captured by the LAMBDA setup for the same beating (c) comparisons of the calcium concentration measured by fluorescent signal and the intensity measured by LAMBDA setup that reflect biomechanical dynamics from three selected pixels.

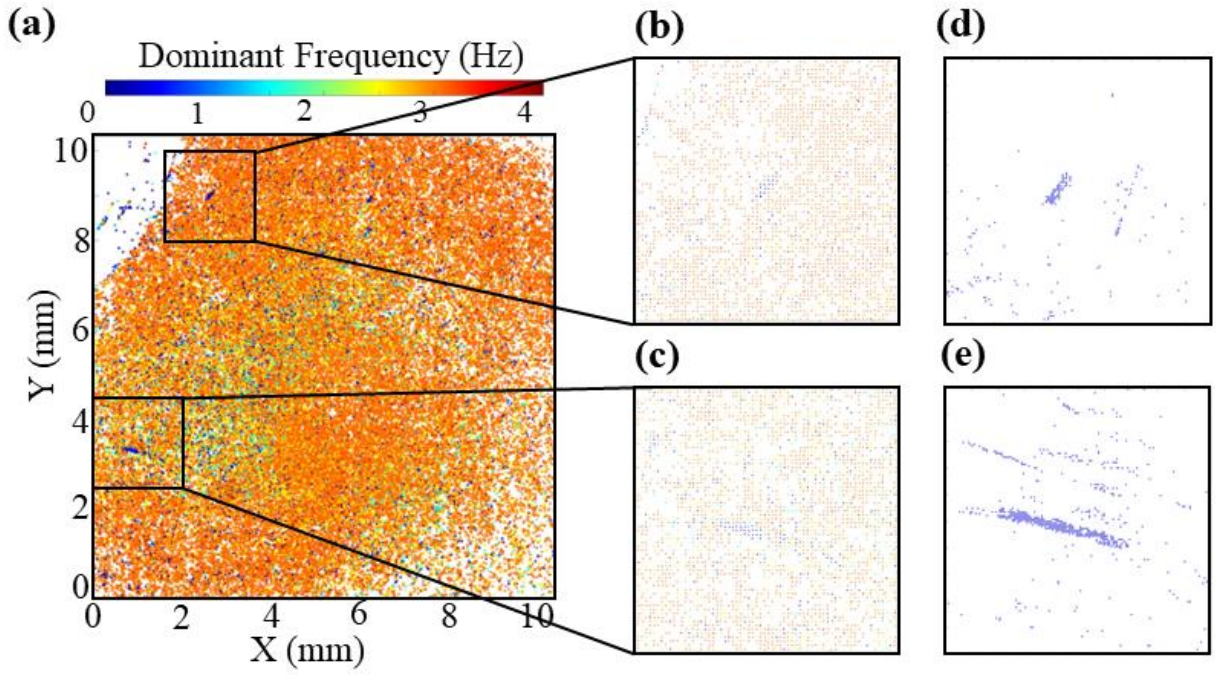

Figure 3.28 (a) Dominant frequency map measured by the LAMBDA platform. (b) and (c) zoom-in areas of the dominant frequency map. (d) and (e) same zoom-in areas from the distribution of large fluorescent change signal shown in Figure 3.27(a).

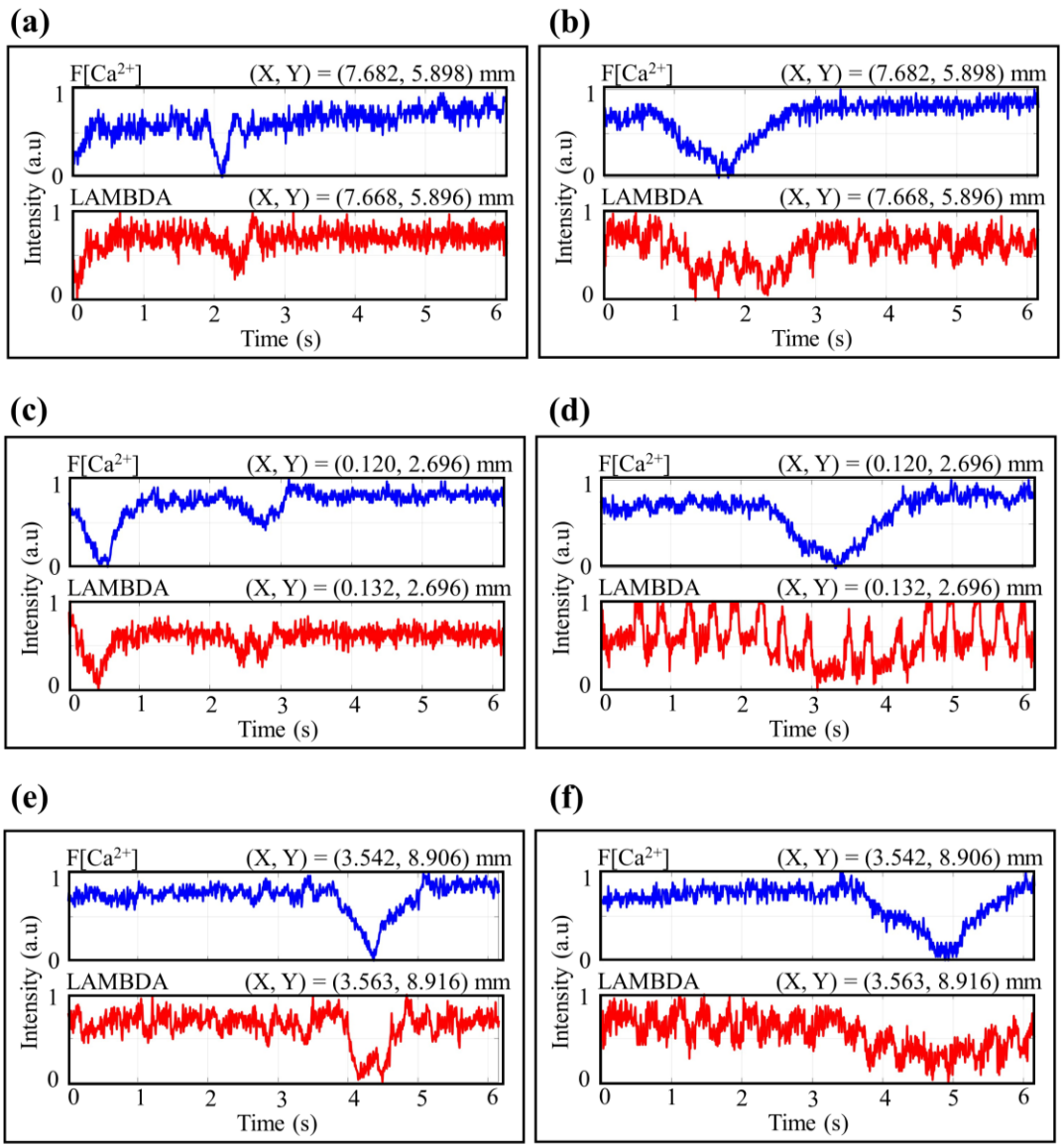

Figure 3.29 Comparisons of the calcium concentration measured by fluorescent signal and the intensity measured by LAMBDA setup that reflect biomechanical dynamics at different locations that radiating patterns.

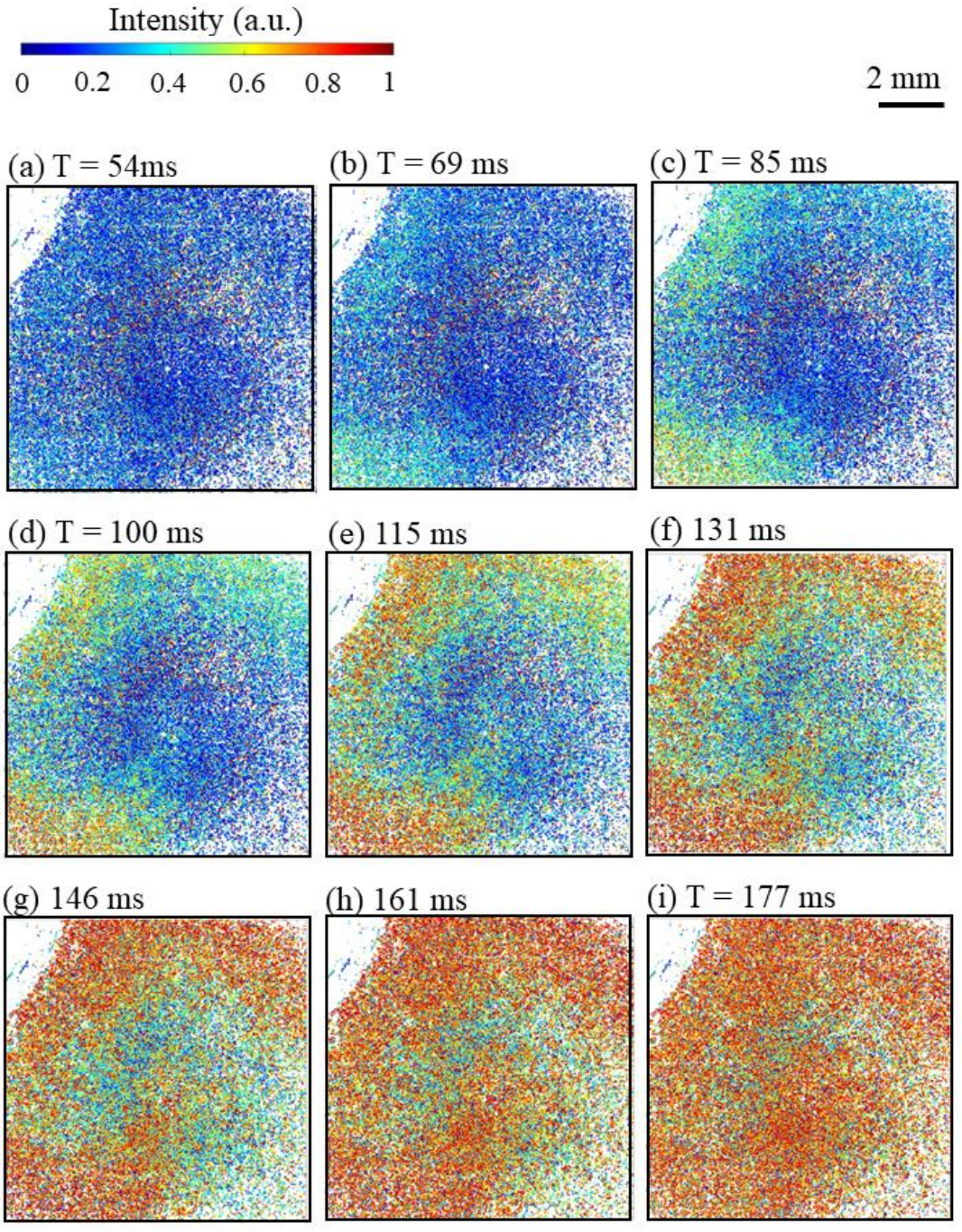
Intensity (a.u.)
0 0.2 0.4 0.6 0.8 1
2 mm
(a) T = 54ms
(b) T = 69 ms
(c) T = 85 ms
(d) T = 100 ms
(e) 115 ms
(f) 131 ms
(g) 146 ms
(h) 161 ms
(i) T = 177 ms

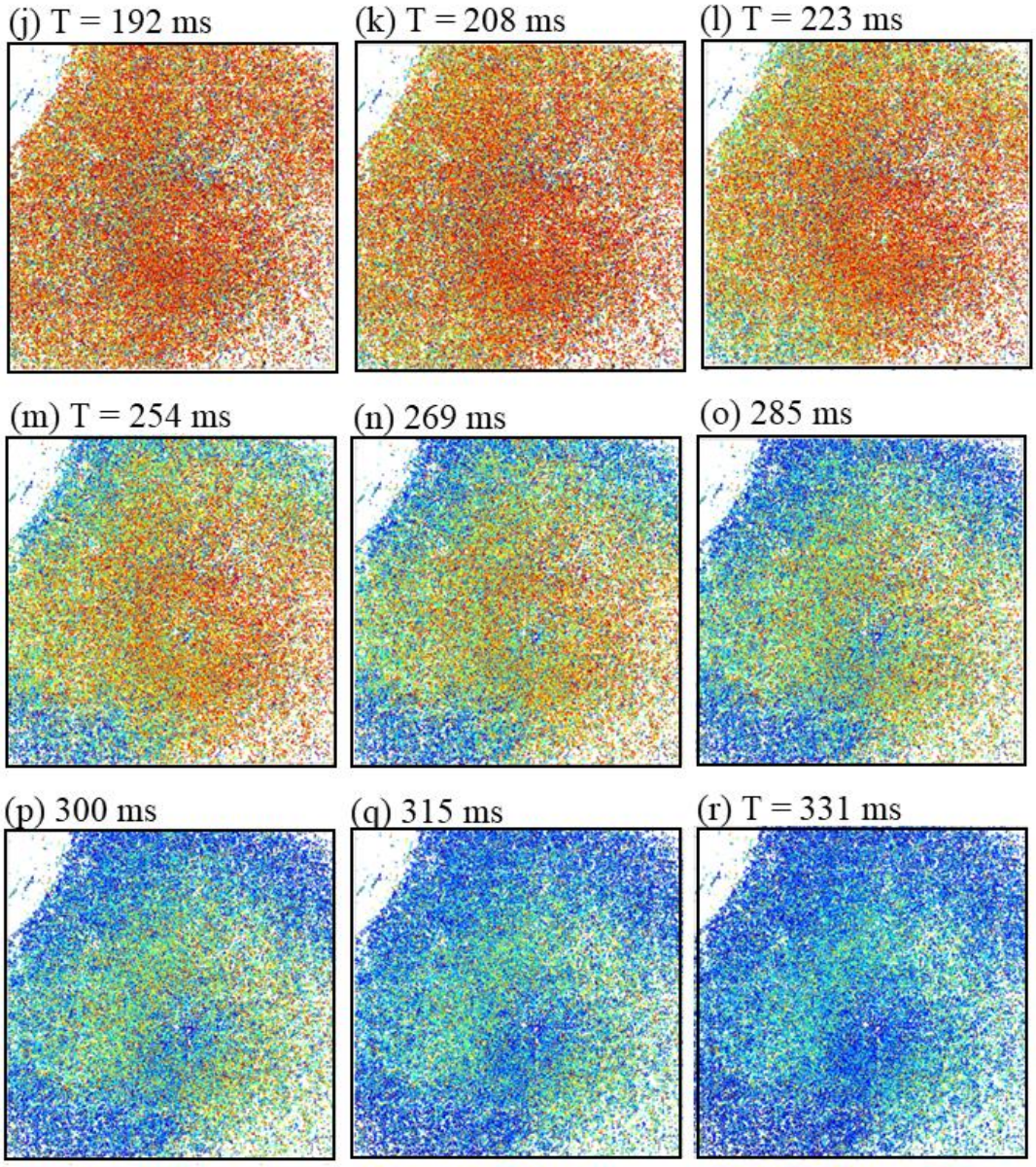

Figure 3.30 Time-course intensity change of captured beating.

Chapter 4 Conclusions and Future Work

To sum up, a novel platform called" LAMBDA" for mapping the large-area biomechanical dynamics is proposed, designed, and established. The platform utilizes a massive number of optical diffractive elements embedded periodically in an elastic membrane to track the traction force generated by the cells seeded on top. Due to the extended field of view and high temporospatial resolution of the LAMBDA platform, it can capture the transient biomechanical dynamics spanning long distances with extremely fine details. Moreover, the label-free feature of our platform introduces minimized interruption to the physiological activities of cells, thereby extending the observation time of experiments. Lastly, the platform can be integrated with conventional optical mapping to further study the complex interplays between biomechanical, biochemical, and bioelectrical properties in the future.

There are different aspects that can be further improved for the current platform. First, the yield and uniformity of devices can be enhanced by advanced fabrication technologies such as direct printing of PDMS. With better yield and uniformity, the device area can be further enlarged to create an even larger field of view. Next, a comprehensive calibration model to bridge up the relationship between the diffraction pattern and the displacements is desirable. This can help quantitatively retrieve the cellular traction force occurred in the dynamic events with both magnitude and direction of the traction force. Additionally, other cell types such as human induced pluripotent stem cell-derived cardiomyocytes can be measured in our platform for more biological studies and discoveries.

Appendix A Fabrication Process

Recipe for Patterning SU8

SU8 2002 (~ 2um thick)

- Oxygen plasma treatment for the glass substrate, 30s (Technics fluorine RIE 800, 500 mTorr, 80 W)
- Spin coating
    - Step 1: rate 1000 rpm, ramp 500 rpm/s, 5s
    - Step 2: rate 3000 rpm, ramp 1000 rpm/s, 45s
- Soft bake 95°C, 1.5 mins
- Exposure 15 s (Lamp power 8mW), hard contact
- Post exposure bake 95°C, 1.5 mins
- Develop in SU8 developer, 1 min
- Hard bake 150°C, 10 mins

Recipe for Patterning AZ5214 Photoresist

AZ5214 (~ 2um thick)

- Vapor deposition of adhesive layer HMDS, 3 mins
- Spin coating
    - Step 1: rate 500 rpm, ramp 250 rpm/s, 5s
    - Step 2: rate 2000 rpm, ramp 1000 rpm/s, 45s
- Soft bake 100°C, 1 min

- Exposure 13.5 s (Lamp power 8mW), hard contact
- Develop in diluted AZ 400K Developer (developer: water = 1:4), 25s

Recipe for Making PVA-Coated Glasses

- 4 %wt PVA solution is spined coat at 2000 RPM on glass substrate, baked at 65°C for 1 minute and then 130°C for 30 minutes.

Recipe for Removing PDMS Residual

- SF_6 = 80.0 sccm, O_2 = 20.0 sccm, RF forward power = 270W, Process pressure = 0.24 Torr

Recipe for Isotropic Metal Deposition

- Metal: SiO_2/Ti/Al/Ti/SiO_2; Thickness: 10nm/10nm/100nm/10nm/10nm; Rate: 1Å/s for SiO_2 and Ti, 3Å/s for Al.
- Titanium and silicon dioxide are used to improve the adhesion in between glass-metal interface metal-PDMS interface.

Appendix B Detailed Setup Schematics and Cell Seeding/Staining Procedure

Stage Top Incubator

A heatable mounting frame with a 47.5mm x 21mm observation window (Zeiss, heatable mounting frame KH-L S) and a plastic cover with slidable opening and gas inlet (Zeiss, CO2 cover micromanipulation K) comprise the main chamber for the stage top incubator. The chamber is mounted on a 5-axis micro-actuated manual stage (Newport, 562 series) to allow adjustment of its position (**Figure B-1**). A gas mixture with 95% air and 5% carbon dioxide (CO_2) is constantly supplied into the chamber. The percentage of the output gas mixture and circulation is controlled by a CO_2 module (Zeiss PeCon CO2 Module S1). The gas mixture is first fed into a humidifier that is filled with warm water (37 °C). Then, the humid gas mixture (95% air, 5% CO2) is fed into the cover of the chamber via the gas inlet. Both the heatable mounting frame and the humidifier bottle are heated to 37 °C using a temperature control module (Zeiss PeCon Temp Module S). The temperature control module and the CO_2 module are connected to a desktop and can be controlled remotely.

During measurements, the device with the seeded cells on top is put on the heatable mounting frame and the active area of the device is aligned with the observation window. To prevent condensation from the evaporated culture medium, the plastic cover is heated by 2 pieces of polyimide heater films (each is supped with DC 8.5V), as shown in **Figure B-1 (a).** The

homemade stage top incubator allows long-term observation of cellular dynamics for several days to weeks. The culture medium is replenished manually every other day.

Illumination

To minimize light scattering in the tissue, deep red LED is selected for most of the experiments. On the other hand, to incorporate fluorescent measurements, the wavelength of LED will be changed according to the excitation spectrum of the fluorescent dyes. Possible combinations of fluorescent dyes, LEDs, dichroic mirrors, and emission filters are given in **Table i**.

Table i Combinations of fluorescent dyes, LEDs, dichroic mirrors, and emission filters.

Fluorescent dye	RH237	Di-4-ANBDQBS	Rhod2-AM
Type	Transmembrane potential	Transmembrane potential	Calcium concentration
$\lambda_{excitation}/\lambda_{emission}$	528nm/782nm	630nm/760nm	552nm/581nm
Illumination	Green (520-525nm)	Red (620-630nm)	Green (520-525)
Dichroic mirror	DMLP567R (Thorlabs) R:380-550nm, T: 584-800nm	HPD 695(Newport) R:630-684nm T: 705-780nm	MD568 (Thorlabs) R:525-556nm T: 580-655nm
Emission filter	FELH0700 (Thorlabs)	FELH0700 (Thorlabs)	FBH580-010 (Thorlabs)

Image Sensors

The CMOS image sensor (Emergent Vision Technologies, HB25000-SB-M) for the LAMBDA platform is connected to a desktop via a 25 GigE network interface card (Mellanox

25G) and controlled through a customized program written by C++ code. To reduce latency during data acquisition, the frames captured by the image sensor are first streamed into the random-access memory (RAM) of the desktop. Subsequently, after the recording is finished, each frame is saved as a raw image file individually.

For the experiments combined with fluorescent images, another CMOS image sensor (IDS, UI-3080CP-M-GL, Rev.2) is utilized to record the fluorescent signals. The image sensor is connected to a desktop via a USB3.0 cable and controlled by the same custom program mentioned in the previous paragraph. To synchronize the two cameras during data acquisition, they are operated in trigger mode and fed using the same control signal.

Control Circuit for Automatic Data Acquisition

To automatically implement the data acquisition, a control circuit is designed. Two NPN transistors are used as switches to control the ON/OFF status of LED illumination and camera triggers. Arduino circuit board is utilized to give the control signal for the switches. The schematics of the control circuit is shown in **Figure B-1(b)**. Finally, the entire data acquisition process can be run automatically using task scheduler (Window's built-in software) at any pre-set time points.

Device Preparation Prior to Cell Seeding

To prepare device for cell seeding, the device is first rinsed by 75% isopropyl solution (IPA) followed by deionized water and then dried with nitrogen. PDMS well with the desired size are bonded to the device after oxygen plasma treatment (Technics fluorine RIE 800, 500 mTorr, 80 W, 30s). The PDMS well is used to confine the culture medium during experiments. Afterward, the device is dried in a vacuum chamber with calcium chloride (as desiccant) overnight. Prior to seeding cells, the device is first coated with dopamine (Alfa Aesar Chemicals) solution (0.01%, w/v in 1M Tris-HCl buffer, Boston BioProducts, Inc.) at 4°C for an hour. Then, the device is

washed twice with phosphate buffered saline (PBS) solution (Corning Inc.) and deionized water, respectively. Afterward, a 35-minutes ultraviolet (UV) sterilization is conducted. Subsequently, Geltrex (83 µL/mL, Thermo Fisher Scientific Inc.) is coated on the device for 1 hour right before seeding cells.

Loading Protocol of Fluorescent Dyes: Rhod-2 AM

First, 1 mM stock solution is made by mixing 44.5 µL dimethyl sulfoxide (DMSO, Thermo Fisher Scientific Inc) with 50 µg Rhod-2 AM (Invitrogen). Then, 44.5 µL Pluronic F-127 (20% w/v solution in DMSO, Thermo Fisher Scientific Inc) is mixed with the stock solution for assisting the dispersion of the nonpolar AM ester. Afterward, 5 µL of the 1mM stock solution is diluted in 1mL buffer solution (DPBS, calcium, magnesium, Gibco™, 14-040-133) and incubated with the cells seeded on the device, The final concentration of Rhod-2 AM is 5 µM. After incubating for 1 hour, the buffer solution with dye is removed and the sample is rinsed with DPBS twice. The cell culture is incubated for another 30 minutes before taking the fluorescent imaging.

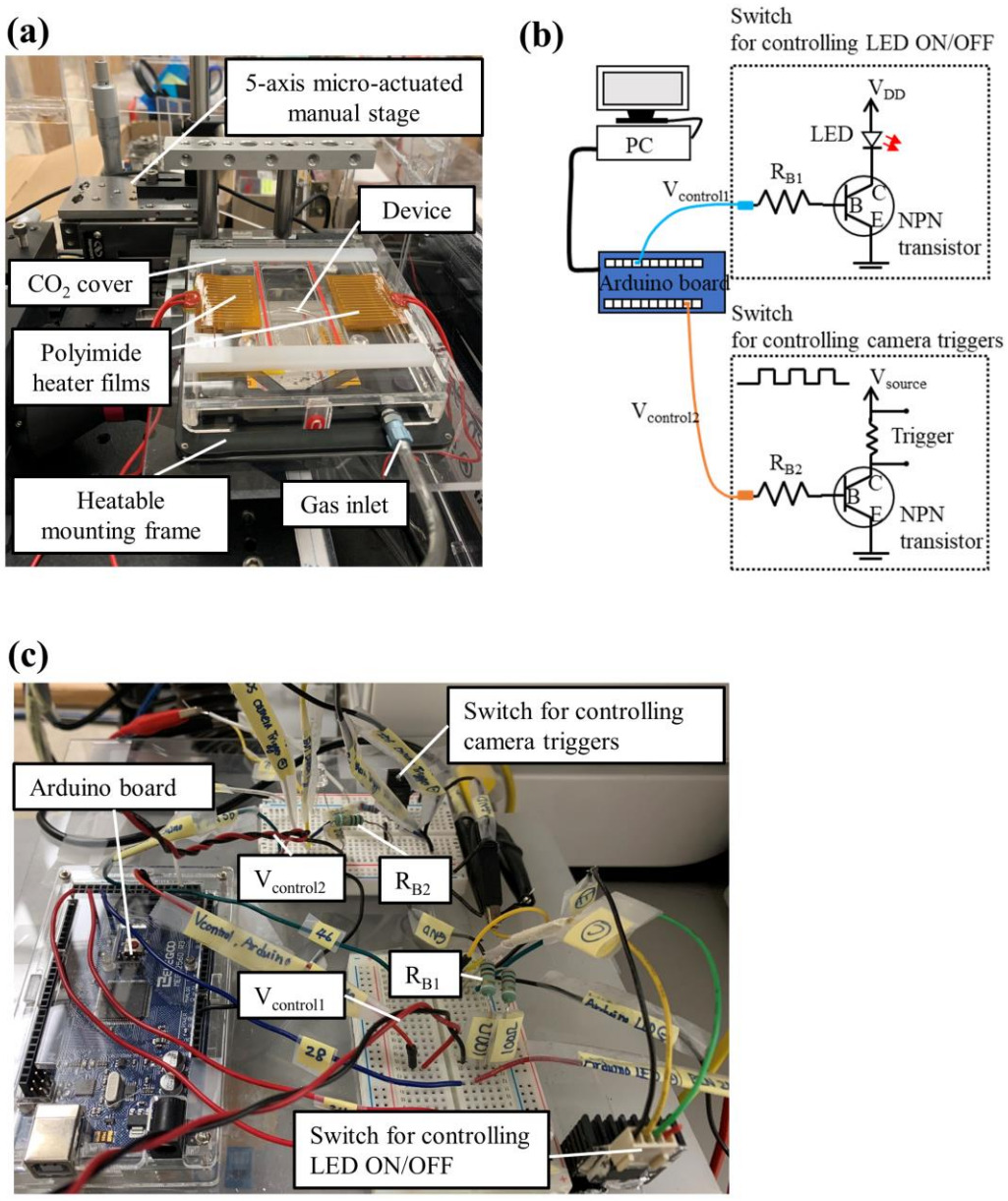

Figure B-1 (a) Stage top incubator: main chamber mounted on a 5-axis micro-actuated manual stage for position adjustment and polyimide heater films to heat the plastic cover to prevent condensation of culture medium. (b) schematics of the control circuit (c) photo of the control circuit.

Appendix C Devices Used for the Cells Experiments

Table ii Summaries of devices and parameters used in cells experiments.

D = diameter of diffractive elements, P = Periodicity of diffractive elements

T = thickness of PDMS, E = stiffness of PDMS

Section	3.4.1	3.4.2
Experiment	Spontaneous beating	Electrical simulation
Device parameters	D = 10 μm, P = 20 μm T = 2 μm, E = 50 kpa	D = 10 μm, P = 30 μm T = 2 μm, E= 50 kpa
Device area	2cm x 2cm	2cm x 2cm
Cell numbers	1 million	0.8 million
Date seeded	Nov. 22, 2022	June 14, 2022
Measurement Date and Time	Nov. 26, 2022 8:54 AM: Recording #1	June 20, 2022 4:07 PM: Recording #1 **4:22 PM: 1 min pacing** 4:28 PM: Recording #2 4:40 PM: Recording #3
Illumination	LED 660nm, 450mA ~3W	LED 660nm, 450mA ~3W
Camera parameters	20 ms (exposure) 48 fps (frame rate), 800 frames	20 ms (exposure) 48 fps (frame rate), 800 frames

Section	3.4.3	
Experiment	Chemical stimulation (phenylephrine)	
Device parameters	D = 15 μm, P = 30 μm T = 2 μm, E= 50 kpa	
Device area	2cm x 2cm (Defect at the left-top corner)	
Cell numbers	0.4 million	
Date seeded	June 14, 2022	
Measurement Date and Time	<u>June 21, 2022</u> 8:04 PM: Recording#1 8:08 PM: Recording#2 8:13 PM: Recording#3 8:19 PM: Recording#4 8:24 PM: Recording#5 8:34 PM: Recording#6 **8:37 PM: Add phenylephrine** 8:40 PM: Recording#7 8:42 PM: Recording#8 8:45 PM: Recording#9 8:50 PM: Recording#10 8:55 PM: Recording#11 9:00 PM: Recording#12 9:05 PM: Recording#13	9:10 PM: Recording#14 9:15 PM: Recording#15 9:20 PM: Recording#16 9:25 PM: Recording#17 9:30 PM: Recording#18 9:40 PM: Recording#19 9:50 PM: Recording#20 10:00 PM: Recording#21 10:10 PM: Recording#22 10:20 PM: Recording#23 10:30 PM: Recording#24 10:40 PM: Recording#25 10:50 PM: Recording#26 11:00 PM: Recording#27 11:05 PM: Recording#28

Illumination	LED 660nm, 450mA ~3W
Camera parameters	Recording #1, #2: 10 ms (exposure) 95 fps (frame rate), 800 frames Recording #3: 5 ms (exposure) 130 fps (frame rate), 1600 frames All other Recordings: 8 ms (exposure) 115 fps (frame rate), 1600 frames

Section	3.4.4	
Experiment	Long-term observation	
Device parameters	D = 15 μm, P = 30 μm T = 2 μm, E= 50 kpa	
Device area	2cm x 2cm (Defect at the left top)	
Cell numbers	0.4 million	
Date seeded	June 14, 2022	
Measurement Date and Time	June 17, 2022 6:01PM (8ms 115fps 800 frames) June 18, 2022 5:34 PM (10ms 95fps 800 frames) June 20, 2022 8:28 PM (10ms 95fps 800 frames)	June 21, 2022 8:34 PM (8ms 115fps 800 frames) **8:37 PM: Add phenylephrine** 11:05 PM (8ms 115fps 800 frames) June 22, 2022 9:55 PM (8ms 115fps 800 frames) June 23, 2022 12:55 PM (5ms 130fps 800 frames)
Illumination	LED 660nm, 450mA ~3W	

Section	3.4.5
	Simultaneous Measurements of Calcium Ions Concentrations and Biomechanical Dynamics (Dye: Rhod2-AM)
Device parameters	D = 10 µm, P = 30 µm T = 2 µm, E= 50 kpa
Device area	2cm x 2cm
Cell numbers	0.8 million
Date seeded	Feb. 21, 2023
Measurement Date and Time	Feb. 24, 2023, 5:53 PM: Recording #1 (5ms 130fps 1600frames)
Illumination	LED 520nm, 900mA ~5W

Reference

[1] E. Moeendarbary and A. R. Harris, “Cell mechanics: Principles, practices, and prospects,” Wiley Interdiscip Rev Syst Biol Med, vol. 6, no. 5, pp. 371–388, 2014, doi: 10.1002/wsbm.1275.

[2] S. Suresh et al., “Connections between single-cell biomechanics and human disease states: Gastrointestinal cancer and malaria,” Acta Biomater, vol. 1, no. 1, pp. 15–30, 2005, doi: 10.1016/j.actbio.2004.09.001.

[3] E. K. Paluch et al., “Mechanotransduction: Use the force(s),” BMC Biol, vol. 13, no. 1, Jul. 2015, doi: 10.1186/s12915-015-0150-4.

[4] B. Ladoux and R. M. Mège, “Mechanobiology of collective cell behaviours,” Nat Rev Mol Cell Biol, vol. 18, no. 12, pp. 743–757, Dec. 2017, doi: 10.1038/nrm.2017.98.

[5] D. E. Jaalouk and J. Lammerding, “Mechanotransduction gone awry,” Nature Reviews Molecular Cell Biology, vol. 10, no. 1. pp. 63–73, Jan. 2009. doi: 10.1038/nrm2597.

[6] P. G. Vikhorev and N. N. Vikhoreva, “Cardiomyopathies and related changes in contractility of human heart muscle,” Int J Mol Sci, vol. 19, no. 8, 2018, doi: 10.3390/ijms19082234.

[7] M. F. Fournier, R. Sauser, D. Ambrosi, J. J. Meister, and A. B. Verkhovsky, “Force transmission in migrating cells,” Journal of Cell Biology, vol. 188, no. 2, pp. 287–297, Jan. 2010, doi: 10.1083/jcb.200906139.

[8] C. M. Nelson et al., “Emergent patterns of growth controlled by multicellular form and mechanics,” PNAS, vol. 102, no. 33, 2005, [Online]. Available: www.pnas.orgcgidoi10.1073pnas.0502575102

[9] D. A. Lee, M. M. Knight, J. J. Campbell, and D. L. Bader, “Stem cell mechanobiology,” J Cell Biochem, vol. 112, no. 1, pp. 1–9, Jan. 2011, doi: 10.1002/jcb.22758.

[10] J. Jalife, “VENTRICULAR FIBRILLATION: Mechanisms of Initiation and Maintenance,” 2000. [Online]. Available: www.annualreviews.org

[11] J. Pellman and F. Sheikh, “Atrial fibrillation: Mechanisms, therapeutics, and future directions,” Compr Physiol, vol. 5, no. 2, pp. 649–665, Apr. 2015, doi: 10.1002/cphy.c140047.

[12] A. K. Nguyen and K. A. Kilian, “Physicochemical Tools for Visualizing and Quantifying Cell-Generated Forces,” ACS Chem Biol, vol. 15, no. 7, pp. 1731–1746, Jul. 2020, doi: 10.1021/acschembio.0c00304.

[13] J. C. Calderón, P. Bolaños, and C. Caputo, “The excitation-contraction coupling mechanism in skeletal muscle,” Biophysical Reviews, vol. 6, no. 1. pp. 133–160, Mar. 2014. doi: 10.1007/s12551-013-0135-x.

[14] J. B. Hurshl, “CONDUCTION VELOCITY AND DIAMETER OF NERVE FIBERS,” American Journal of Physiology, vol. 127, no. 1, pp. 131–139, 1939.

[15] M. Ikeda and Y. Oka, “The relationship between nerve conduction velocity and fiber morphology during peripheral nerve regeneration,” Brain Behav, vol. 2, no. 4, pp. 382–390, Jul. 2012, doi: 10.1002/brb3.61.

[16] M. H. Draper and M. Mya-Tu, “A COMPARISON OF THE CONDUCTION VELOCITY IN CARDIAC TISSUES OF VARIOUS MAMMALS,” Q J Exp Physiol Cogn Med Sci, vol. 44, no. 1, pp. 91–109, Jan. 1959, doi: 10.1113/expphysiol.1959.sp001379.

[17] E. Carmeliet, “Conduction in cardiac tissue. Historical reflections,” Physiological Reports, vol. 7, no. 1. American Physiological Society, Jan. 01, 2019. doi: 10.14814/phy2.13860.

[18] K. R. Laurita and A. Singal, “Mapping action potentials and calcium transients simultaneously from the intact heart,” 2001. [Online]. Available: http://www.ajpheart.org

[19] W. J. Polacheck and C. S. Chen, “Measuring cell-generated forces: A guide to the available tools,” Nat Methods, vol. 13, no. 5, pp. 415–423, 2016, doi: 10.1038/nmeth.3834.

[20] C. M. Kraning-rush, J. P. Califano, and C. A. Reinhart-king, “Cellular Traction Stresses Increase with Increasing Metastatic Potential,” PLoS One, vol. 7, no. 2, 2012, doi: 10.1371/journal.pone.0032572.

[21] S. Munevar, Y. Wang, and M. Dembo, “Traction Force Microscopy of Migrating Normal and H-ras Transformed 3T3 Fibroblasts,” Biophys J, vol. 80, no. April, pp. 1744–1757, 2001.

[22] I. M. Tolić-Nørrelykke and N. Wang, “Traction in smooth muscle cells varies with cell spreading,” J Biomech, 2005.

[23] H. Colin-York et al., “Super-Resolved Traction Force Microscopy (STFM),” Nano Lett, vol. 16, no. 4, pp. 2633–2638, Apr. 2016, doi: 10.1021/acs.nanolett.6b00273.

[24] S. Makarchuk, N. Beyer, C. Gaiddon, W. Grange, and P. Hébraud, “Holographic Traction Force Microscopy,” Sci Rep, vol. 8, no. 1, Dec. 2018, doi: 10.1038/s41598-018-21206-2.

[25] M. Bergert et al., “Confocal reference free traction force microscopy,” Nat Commun, vol. 7, Sep. 2016, doi: 10.1038/ncomms12814.

[26] S. Sridharan Weaver et al., “Simultaneous cell traction and growth measurements using light,” J Biophotonics, vol. 12, no. 3, Mar. 2019, doi: 10.1002/jbio.201800182.

[27] W. R. Legant, J. S. Miller, B. L. Blakely, D. M. Cohen, G. M. Genin, and C. S. Chen, “Measurement of mechanical tractions exerted by cells in three-dimensional matrices,” Nat Methods, vol. 7, no. 12, 2010, doi: 10.1038/NMETH.1531.

[28] I. Pushkarsky et al., “Elastomeric sensor surfaces for high-Throughput single-cell force cytometry,” Nat Biomed Eng, vol. 2, no. 2, pp. 124–137, Feb. 2018, doi: 10.1038/s41551-018-0193-2.

[29] J. Fu et al., “Mechanical regulation of cell function with geometrically modulated elastomeric substrates,” Nat Methods, vol. 7, no. 9, pp. 733–736, Sep. 2010, doi: 10.1038/nmeth.1487.

[30] S. Ghassemi, G. Meacci, S. Liu, A. A. Gondarenko, and A. Mathur, “Cells test substrate rigidity by local contractions on submicrometer pillars,” Proc Natl Acad Sci U S A, pp. 1–6, 2012, doi: 10.1073/pnas.1119886109/-/DCSupplemental.www.pnas.org/cgi/doi/10.1073/pnas.1119886109.

[31] H. Wolfenson et al., “Tropomyosin controls sarcomere-like contractions for rigidity sensing and suppressing growth on soft matrices,” Nat Cell Biol, vol. 18, no. 1, pp. 33–42, Jan. 2016, doi: 10.1038/ncb3277.

[32] J. Hui and S. W. Pang, “Cell traction force in a confined microenvironment with double-sided micropost arrays,” RSC Adv, 2019.

[33] F. Xiao, X. Wen, X. H. M. Tan, and P. Y. Chiou, “Plasmonic micropillars for precision cell force measurement across a large field-of-view,” Appl Phys Lett, vol. 112, no. 3, Jan. 2018, doi: 10.1063/1.5005525.

[34] D. Post, B. Han, and P. G. Ifju, “Moiré Methods for Engineering and Science-Moiré Interferometry and Shadow Moiré.”

[35] X. Zheng and X. Zhang, “Optical moiŕe as a visualization tool for living vascular cell contraction force mapping,” Appl Phys Lett, vol. 93, no. 16, 2008, doi: 10.1063/1.3006430.

[36] C. Grashoff et al., “Measuring mechanical tension across vinculin reveals regulation of focal adhesion dynamics,” vol. 466, no. July, pp. 6–10, 2010, doi: 10.1038/nature09198.

[37] K. Austen et al., “Extracellular rigidity sensing by talin isoform-specific mechanical linkages,” vol. 17, no. 12, 2015, doi: 10.1038/ncb3268.

[38] D. Eder, K. Basler, and C. M. Aegerter, “Challenging FRET-based E-Cadherin force measurements in Drosophila,” no. October, pp. 1–12, 2017, doi: 10.1038/s41598-017-14136-y.

[39] I. L. Jones, P. Livi, M. K. Lewandowska, M. Fiscella, B. Roscic, and A. Hierlemann, “The potential of microelectrode arrays and microelectronics for biomedical research and diagnostics,” Analytical and Bioanalytical Chemistry, vol. 399, no. 7. pp. 2313–2329, Mar. 2011. doi: 10.1007/s00216-010-3968-1.

[40] A. Tanwar, H. A. Gandhi, D. Kushwaha, and J. Bhattacharya, “A review on microelectrode array fabrication techniques and their applications,” Mater Today Chem, 2022.

[41] B. Eversmann et al., “A 128 × 128 CMOS Biosensor Array for Extracellular Recording of Neural Activity,” in IEEE Journal of Solid-State Circuits, Dec. 2003, pp. 2306–2317. doi: 10.1109/JSSC.2003.819174.

[42] F. Heer, S. Hafizovic, W. Franks, A. Blau, C. Ziegler, and A. Hierlemann, “CMOS microelectrode array for bidirectional interaction with neuronal networks,” in IEEE Journal of Solid-State Circuits, Jul. 2006, pp. 1620–1629. doi: 10.1109/JSSC.2006.873677.

[43] C. O'Shea et al., "Cardiac optical mapping – State-of-the-art and future challenges," International Journal of Biochemistry and Cell Biology, vol. 126. Elsevier Ltd, Sep. 01, 2020. doi: 10.1016/j.biocel.2020.105804.

[44] M. Attin and W. T. Clusin, "Basic concepts of optical mapping techniques in cardiac electrophysiology," Biol Res Nurs, vol. 11, no. 2, pp. 195–207, Oct. 2009, doi: 10.1177/1099800409338516.

[45] C. N. Broyles, P. Robinson, and M. J. Daniels, "Fluorescent, bioluminescent, and optogenetic approaches to study excitable physiology in the single cardiomyocyte," Cells, vol. 7, no. 6. MDPI, Jun. 01, 2018. doi: 10.3390/cells7060051.

[46] C. Omichi et al., "Intracellular Ca dynamics in ventricular fibrillation," Am J Physiol Heart Circ Physiol, vol. 286, pp. 1836–1844, 2004, doi: 10.1152/ajpheart.00123.2003.-In.

[47] V. Kappadan et al., "High-Resolution Optical Measurement of Cardiac Restitution, Contraction, and Fibrillation Dynamics in Beating vs. Blebbistatin-Uncoupled Isolated Rabbit Hearts," Front Physiol, vol. 11, May 2020, doi: 10.3389/fphys.2020.00464.

[48] N. Shaheen et al., "Human Induced Pluripotent Stem Cell-Derived Cardiac Cell Sheets Expressing Genetically Encoded Voltage Indicator for Pharmacological and Arrhythmia Studies," Stem Cell Reports, vol. 10, no. 6, pp. 1879–1894, Jun. 2018, doi: 10.1016/j.stemcr.2018.04.006.

[49] D. Filice et al., "Optical mapping of human embryonic stem cell-derived cardiomyocyte graft electrical activity in injured hearts," Stem Cell Res Ther, vol. 11, no. 1, Sep. 2020, doi: 10.1186/s13287-020-01919-w.

[50] A. Gibbons et al., “Real-time visualization of cardiac cell beating behaviour on polymer diffraction gratings,” RSC Adv, vol. 7, no. 81, pp. 51121–51129, 2017, doi: 10.1039/c7ra06515a.

[51] X. H. M. Tan, “Cell Traction Force Measurement Platforms,” 2021.

[52] M. Rappel et al., “Microelectrode array a new tool to measure embryonic heart activity,” J Electrocardiol, vol. 37, pp. 104–109, 2004.

[53] J. I. Laughner, * Fu, S. Ng, M. S. Sulkin, R. Martin Arthur, and I. R. Efimov, “Processing and analysis of cardiac optical mapping data obtained with potentiometric dyes,” Am J Physiol Heart Circ Physiol, vol. 303, pp. 753–765, 2012, doi: 10.1152/ajpheart.00404.2012.-Optical.

[54] A. Sommerfled, Optics, volume IV of Lectures on Theoretical Physics. New York: Academic Press, Inc., 1954.

[55] L. B. Hazeltine et al., “Effects of substrate mechanics on contractility of cardiomyocytes generated from human pluripotent stem cells,” Int J Cell Biol, 2012, doi: 10.1155/2012/508294.

[56] J. G. Jacot, A. D. McCulloch, and J. H. Omens, “Substrate Stiffness Affects the Functional Maturation of Neonatal Rat Ventricular Myocytes,” Biophysical Jouranl, 2008.

[57] A. J. S. Ribeiro et al., “Contractility of Single cardiomyocytes differentiated from pluripotent stem cells depends on physiological shape and substrate stiffness,” Proc Natl Acad Sci U S A, vol. 112, no. 41, pp. 12705–12710, Oct. 2015, doi: 10.1073/pnas.1508073112.

[58] R. N. Palchesko, L. Zhang, Y. Sun, and A. W. Feinberg, “Development of Polydimethylsiloxane Substrates with Tunable Elastic Modulus to Study Cell

Mechanobiology in Muscle and Nerve," PLoS One, vol. 7, no. 12, Dec. 2012, doi: 10.1371/journal.pone.0051499.

[59] P. Roca-Cusachs, V. Conte, and X. Trepat, "Quantifying forces in cell biology," Nat Cell Biol, vol. 19, no. 7, pp. 742–751, 2017, doi: 10.1038/ncb3564.